Design and Testing of a High Accuracy Robotic Single-cell Manipulator

by

Jun Young Yoon

B.S., Mechanical Engineering, Yonsei University (2009)

Submitted to the Department of Mechanical Engineering
in partial fulfillment of the requirements for the degree of

Master of Science in Mechanical Engineering

at the

MASSACHUSETTS INSTITUTE OF TECHNOLOGY

June 2011

Author .....
Department of Mechanical Engineering
May 19, 2011

Certified by .....
David L. Trumper
Professor of Mechanical Engineering
Thesis Supervisor

Accepted by .....
David E. Hardt
Chairman, Department Committee on Graduate Students

Design and Testing of a High Accuracy Robotic Single-cell Manipulator

by

Jun Young Yoon

Submitted to the Department of Mechanical Engineering
on May 19, 2011, in partial fulfillment of the
requirements for the degree of
Master of Science in Mechanical Engineering

Abstract

We have designed, built and tested a high accuracy robotic single-cell manipulator to be able to pick individual cells from array of microwells, each 30 μm or 50 μm cubed. Design efforts have been made for higher accuracy, higher throughput, and compactness. The proposed system is designed to have a T-drive mechanism with two linear stages for XY-plane positioning to have higher stiffness and less structurally inherent error. Precision is especially required in Z-axis movement for successful cell-retrieval procedure and so a rotational mechanism with a voice coil actuator, among many options, is selected for the Z-axis motion because this results in relatively smaller reaction on the system and has advantages of direct drive. The prototype of the robotic single-cell picker integrates the Z-axis and XY stage motion, real-time microscopy imaging, and cell manipulation with a NI PXI-controller centered as a main real-time controller. This prototype is built to test performances of the proposed system in terms of single-cell retrieval and this thesis also discusses the experiments for the cell-retrieval process with microbeads of the equivalent size and the results as well.

This proposed system will be used to help select and isolate an individual hybridoma from polyclonal mixture of cells producing various types of antibodies. It is important to be able to do this cell-retrieval task since a single isolated hybridoma cell produces monoclonal antibody that only recognizes specific antigens, and this monoclonal antibody can be used to develop cures and treatments for many diseases. Our research's development of accurate and dedicated mechatronics solution will contribute to more rapid and reliable investigation of cell properties. Such analysis techniques will act as catalyst for quicker discovery of treatments and vaccines on a wide range of diseases including HIV infection, tuberculosis, hepatitis C, and malaria with potential impact on the society.

Thesis Supervisor: David L. Trumper
Title: Professor of Mechanical Engineering

Acknowledgments

I would first like to thank my advisor, Professor David Trumper for his guidance and support. Professor David Trumper has been inspirational in every aspect, especially with his knowledge in mechanical, electrical, and interdisciplinary fields and with his teaching skills. Every meeting I had with him, I learned valuable lessons on new and interesting things. Also, whenever I talked to him, he led me to set the right direction for my research as well as my courses and his encouraging comments and advice have always been a strength for me to go on. Under his supervision past two years, I have learned much more than I would otherwise expect and I am thrilled to continue my PhD journey in his guidance.

I would also like to thank my labmates for their support and kindness. Aaron Gawlik was always willing to help and answer all my questions. He helped me adjust myself in the lab when I first began my research, and I am always grateful for the support. Ian Mackenzie was also always voluntary to give me valuable advice. His vast knowledge on control was greatly beneficial to my curiosity. Talking to him was always pleasant and his kindness will never be forgotten. Darya Amin-Shahidi has also been a good friend for me and his willingness to help and support has always moved my mind. His expertise in Matlab and Simulink, especially, helped me figure out several issues on my research. From Mohammad Iman Nejad, I gained machine shop experience which helped me much to manufacture a number of parts for the research. His valuable advice based on the field experience was always inspiring and appreciated. I also give my thanks to our administrative assistant, Laura Zaganjori. She helped the lab run smoothly and her help was always timely.

My friends were also very helpful. Sangok Seok, dear friend and my Labview tutor, supported me with his great expertise in Labview. A number of troubles I had with Labview were eased by him and I greatly thank him for his assistance. Chargrak Choi has been my dearest friend ever since I arrived in the United States. He was always open to discussion and talking to him was always refreshing and eye-opening. I would also like to express my gratitude for dear friends, Kyoo-chul and Minseok

for their assistance in every aspect. I thank Lesley Yu from National Instruments for her generous donation of a real-time controller and Sepehr Kiani from Helicos for the donation of microscope stages and a syringe pump. I also thank Leslie Regan and Joan Kravit for their timely support and kindness.

Finally and gratefully, I would like to thank my wife and my little daughter with all my heart. Without my wife's support and faith, I would not be able to finish what I started. The devotion and sacrifice she made for me and the family is most appreciated with all my love. My daughter, Sarie has been a blessing and her existence itself always gives me the strength to carry on. Thank you, daughter.

Contents

1 Introduction 17

1.1 Motivation and Goal of the Research 17

1.2 Layout of the Thesis 18

2 Research Background 21

2.1 Cell-screening Process 21

2.1.1 Microengraving 22

2.2 Cell-retrieval Device 23

2.2.1 Functions of the CellCelector 23

2.2.2 Limitations 24

3 Design Concepts and Component Selection 29

3.1 Design Concepts 29

3.1.1 Design Options for the Cell Picker 30

3.1.2 Conceptual Configurations 33

3.2 Z-axis Mechanism Selection 35

3.2.1 Mechanism Options 35

3.2.2 Actuator and Sensor 42

3.3 Microscope and Microscope Stage 44

3.3.1 Desired Specifications 45

3.3.2 Inverse Microscope Design 46

4 Mechanical Design and Implementation 49

4.1 Prototype of the Single Cell Picker 49
4.2 Picking Method 51
4.2.1 Syringe Pump 51
4.2.2 Issues with Leakage 53
4.3 Z-axis Mechanism 58
4.3.1 Voice Coil Actuator 58
4.3.2 Optical Encoder 61
4.4 Self-designed Microscope 66
4.4.1 Self-designed Inverse Microscope 66
4.4.2 Microscope Stage with Piezo-actuator 69

5 System Integration and Control Design **71**
5.1 System Integration 71
5.1.1 Scheme for the Prototype 72
5.2 PID Control for the XY Stage 73
5.3 Control Loop for the Z-axis Motion 78
5.3.1 Frequency Response of the Plant 79
5.3.2 Mass Disconnection 80
5.3.3 Amplitude-dependent Frequency Response 83
5.3.4 System Modeling by Fitting 88
5.4 Loop-shaping Controller Design 89
5.4.1 Lead Compensator 90
5.4.2 Lead-Lag Compensator 91
5.4.3 Trajectory Generation 94
5.5 System Performance 97
5.5.1 Time Response Analysis 97

6 Experiments, Results, and Challenges **103**
6.1 Experiment Process 103
6.2 Results and Discussions 107
6.3 Challenges 108

6.3.1 Illumination 108
6.3.2 Encoder Alignment and Calibration 109

7 Conclusion and Future Work **117**

A Labview codes **121**

A.1 Control panels for the syringe pump, microscope stage, and vision . . 121
A.2 FPGA edge counter for the A-quad-B encoder 128
A.3 Real-time control loop 129

B Vendors **131**

C Drawing **135**

C.1 Mounting hub for the encoder gratings 135

List of Figures

2-1 Microengraving technique: schematic diagram depicting method for preparation of engraved arrays of secreted products from a mixture of cells. (1)A suspension of cells is deposited onto an array of microwells. (2)The cells are allowed to settle into the wells and then the excess medium is removed by aspiration. (3)The dewetted array is placed in contact with a pretreated solid support (glass slide), compressed lightly and incubated for 2-4h. (4)The microwells are removed from the solid support and placed in a reservoir of medium. (Illustrations and captions taken from [2].) 22

2-2 Picture of the existing system, CellCelector. 24

2-3 Mechanism for the 3-DOF positioner of the CellCelector. 25

2-4 Small error in the first link causing large error at the end-effector. . . 25

3-1 One design option considered for the robotic single-cell manipulator. . 31

3-2 Design of gantry configuration for the robotic single-cell manipulator. 32

3-3 Design of T-drive system for the robotic single-cell manipulator. . . . 33

3-4 Conceptual configurations for the robotic single-cell manipulator. . . 34

3-5 Linear mechanism options considered for the Z-axis motion. 36

3-6 Rotational mechanism options considered for the Z-axis motion. . . . 37

3-7 More options for the Z-axis motion with four-bar linkage structure. . 38

3-8 Cantilever beams under the vertical reaction force and the reaction torque. 39

3-9 Built-in voice coil actuator in a hard disk drive. 42

3-10 Arm extension design for the voice coil actuator. 43
3-11 Assembled CAD model for the Z-axis actuator with arm extension. . 44
3-12 Components for the self-designed inverse microscope. 45
3-13 Assembled CAD model for the self-designed inverse microscope. . . . 46

4-1 Physical configurations of the prototype. 50
4-2 Partial configurations of the microscope and z-axis mechanism. 50
4-3 OEM syringe pump for the process of cell-retrievals. 52
4-4 User interface control panel for the syringe pump. 52
4-5 Cellcelector with its sealing components. 53
4-6 Schematic of how fittings work to seal the pipette module. 54
4-7 Sealing test setup with two different materials of tubing. 55
4-8 Sealing test with two different materials of tubing. 56
4-9 Implementing new tubing prototypes on the CellCelector. 57
4-10 Testing cell-retrievals with a new tubing prototype. 58
4-11 Actuation part of the old hard disk drive selected in the previous chapter. 59
4-12 Rotational z-axis mechanism with VCA and extended arm. 61
4-13 Selected mechatronics system for the z-axis motion. 62
4-14 Mounting position for an optical encoder. 62
4-15 Implementing an optical encoder on the selected mounting area. . . . 63
4-16 Alignment setting for the grating and the mounting hub and a magnified view of the grating patterns. 64
4-17 CAD assembly simulation for the encoder implementation. 65
4-18 Physical system with the encoder, gratings, and head implemented. . 65
4-19 Self-constructed inverse microscope on a granite table. 67
4-20 Testing of the self-constructed microscope. 68
4-21 User interface with Labview for the microscope system. 68
4-22 Piezoceramic actuator in the microscope stage. (Figures taken from [21].) 69

5-1 System schematic for the prototype of the robotic single-cell manipulator. 72

5-2 The software package, PMAC Pro2, for the UMAC controller. 74
5-3 Step response of the stage with the auto-tuned gains. 75
5-4 Step response of the stage with the fine-tuned gains. 76
5-5 Step response of the stage with the reselected gains for faster rise time. 77
5-6 Control loop for Z-axis picking motion. 78
5-7 Setup for the frequency response measurement of the plant. 79
5-8 Measured frequency response of the plant. 80
5-9 Flexure body depicted as two masses connected with a spring and damper. 81
5-10 Simplified pole-zero maps of the collocated and non-collocated system. 82
5-11 Bode plots of two-mass model. 82
5-12 Amplitude-dependent frequency response of the arm system with bearing. Upper curve is with 1 V drive amplitude; lower curve is with 0.3 V drive amplitude. 84
5-13 Friction torque versus relative velocity for large displacement [12]. . . 85
5-14 The friction interface between two surfaces is thought of as a contact between bristles. For simplicity the bristles on the lower part are shown as being rigid. (Illustration and captions taken from [14].) 86
5-15 Bristle friction model for microscopic presliding displacement. (Illustration taken from [14].) 87
5-16 Conceptual sketch of an amplitude-dependent frequency response. . . 87
5-17 Bode plot of the fitted model for the plant. 88
5-18 Bode plot of the experimental response and the analytical model with lead compensator at ω_c=20 Hz. 90
5-19 Effect of T_i on the lead-lag compensator. 92
5-20 Effect of T_i on the loop transfer function. 93
5-21 Frequency response of the loop transfer function with the lead-lag compensator. 94
5-22 Position, velocity, acceleration profile of the cubic polynomial. 95
5-23 Implementation of the trajectory generation on the control loop. . . . 96

5-24 Effect of T_i on the unit step response of the closed loop system. . . . 97
5-25 Error plot of step response of the closed loop system. 98
5-26 Measured time responses of the closed loop system. X axis is in clock ticks of 50 μs. 99
5-27 Magnified portion of the beginning of the step response with a delay. 100

6-1 Bubbles trapped around microwells in hydrophilic and hydrophobic states. 104
6-2 Tip of the picking module on the surface of PDMS microwells. 105
6-3 One block of PDMS microwells before and after the cell-retrieval with the prototype. 107
6-4 Suggested position to place a ring illuminator. 109
6-5 Unexpected oscillation in the closed-loop time responses. 110
6-6 The strange oscillation occurred with double (2×) decoder. 112
6-7 A-quad-B encoder output signal when the oscillation occurs. 113
6-8 No more strange oscillation after realignment and recalibration. . . . 114

A-1 Labview code for the syringe pump control panel. 122
A-2 First case structure in the syringe pump control loop. 123
A-3 Second case structure in the syringe pump control loop. 123
A-4 Detailed code for the Tecan subvi. 124
A-5 Labview code for the microscope stage control panel. 125
A-6 Case structure in the microscope stage control loop. 126
A-7 Labview code for the vision panel. 127
A-8 Labview code for the encoder edge counter in FPGA. 128
A-9 Labview code for the real-time controller. 129
A-10 Detailed code for the Cubic subvi. 130

C-1 Drawing for the mounting hub discussed in Chapter 4. 136

List of Tables

Chapter 1

Introduction

The focus of this thesis is to design and test a high accuracy robotic single-cell manipulator for cell-retrieving processes. We have designed and built a prototype single-cell picker which uses a rotary servomechanism together with a syringe and pipette to pick individual cells from mirowells. Our design has several advantages over an existing system, CellCelector detailed in Chapter2. First, the proposed system uses more compact and simpler design and is structurally less prone to error. Second, the Z-axis, which is the most important part for accurate cell picks, is direct drive so that mechanical errors such as backlash as well as the overall positioning noise can be removed, resulting better precision. This research has been conducted over the last one and a half years in Precision Motion Control (PMC) Laboratory at the Massachusetts Institute of Technology (MIT) under the supervision of Professor David Trumper. In this chapter, we discuss the motivations for the research together with the goal of the project. We also provide the layout of the thesis in this chapter.

1.1 Motivation and Goal of the Research

As multidisciplinary research at the intersection of biology, chemistry, and engineering is growing, the need of engineering insights to the design of instrumentation and processes is also rapidly increasing. The cell-retrieving process is one of those exemplary situations where engineering insights, especially machine design and precision

control, can make a significant difference.

The cell-retrieving/isolation process is very important in biochemistry, biomedical research, and medicine because certain single cells producing monoclonal antibodies can be utilized to find cures and treatments for many diseases. Usually this cell-isolating process comes after cell screening processes where we locate cells of interest among large group of various cells with different secretions. This cell screening process has been significantly improved by a novel technique called microengraving, which is a microwell-based soft lithography method to print and thereby assay secretions of individual cells in large numbers [2].

While the microengraving screening process has high throughput due to the novel technique, the cell-retrieval procedure is limited by the capabilities of a commercially available instrument. The commercial robotic manipulator called CellCelector is essentially less accurate with limited throughput due to the design and mechanism that limit the precision. These issues are detailed in Chapter 2. Accordingly, the main focus of our research is on developing a more reliable and more accurate system with simple and robust design so that the overall throughput for the process can be improved. The primary goal, therefore, is to design and construct a prototype for the proposed system and test it to see if individual cell can be successfully retrieved and if it is possible to eventually automate the critical steps to have higher throughput.

This research's development of precise and dedicated mechatronics solution is believed to contribute to more rapid and reliable investigation of cell properties. Such analysis techniques will act as catalyst for quicker discovery of treatments and vaccines on a wide range of diseases including HIV infection, tuberculosis, hepatitis C, and malaria with potential impact on the society.

1.2 Layout of the Thesis

We have introduced our research by explaining its motivation and goal in this chapter. The rest of the thesis is composed of six other chapters. Chapter 2 provides a brief background for the research by detailing the cell-screening process and the existing

device with its functions and limitations. Chapter 3 then details the design concepts and configurations for our proposed system, robotic single-cell manipulator, and describes component selections. Chapter 4 shows the physical prototype system and details how each part is implemented. In Chapter 5, we explain how we integrate the overall system and how we design our controller to make the prototype ready for test. We then detail the experiments we conducted to test the system and also provide the results in Chapter 6. Finally, we finish the thesis by providing the conclusion and suggestions for the future work. In addition, associated Labview codes and component details together with other relevant information are provided in Appendices A, B, and C.

Chapter 2

Research Background

In this chapter, we discuss the background of our research and provide a context of why this research is of importance. First we detail the technique called *microengraving*, a novel method of cell-screening developed by the Love Lab in the Chemical Engineering Department in MIT, whom we are jointly working with. We then discuss the commercial system for cell retrieval that the Love Lab is currently using; specifications of this system are presented with its limitations.

2.1 Cell-screening Process

In order to understand the context of this research, we need to be familiar with a few biological concepts. A monoclonal antibody is an antibody produced by a single clone of hybridoma cells and only recognizes specific corresponding antigens. This is an important substance in biochemistry, biomedical research, and medicine because this antibody can be used to develop cures and treatments for many diseases. In order to extract a single monoclonal antibody, an individual hybridoma has to be selected from polyclonal mixture of cells producing various types of antibodies. The selection of a hybridoma requires two main tasks: screening of antibodies produced by large group of cells and retrieval of the specific cells with target antibodies [2].

For the screening process, a novel microwell-based technique, called *microengraving* has been recently developed and the basic concept of this method is discussed in

the following section.

2.1.1 Microengraving

Microengraving, is a soft lithography method to print secretions of individual cells using a dense array of microwells (0.1 to 1 nL each) containing single cells. In our current work, the wells are 50 μm cubed. The steps of this technique are illustrated in Figure 2-1 below.

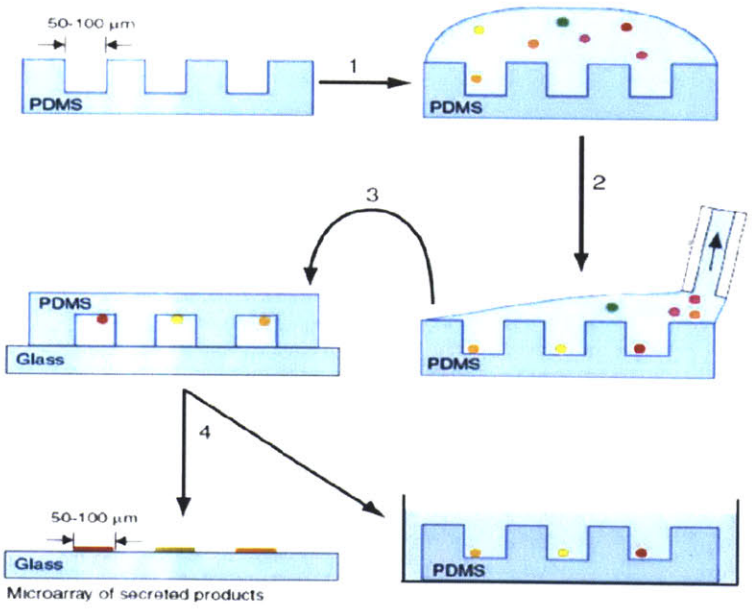

Figure 2-1: Microengraving technique: schematic diagram depicting method for preparation of engraved arrays of secreted products from a mixture of cells. (1)A suspension of cells is deposited onto an array of microwells. (2)The cells are allowed to settle into the wells and then the excess medium is removed by aspiration. (3)The dewetted array is placed in contact with a pretreated solid support (glass slide), compressed lightly and incubated for 2-4h. (4)The microwells are removed from the solid support and placed in a reservoir of medium. (Illustrations and captions taken from [2].)

A polydimethylsiloxane (PDMS) stamp shown in the figure has arrays of microwell blocks and one block is composed of 7×7 50 μm microwells or 12×12 30 μm microwells, allowing one PDMS stamp to contain 84,000 to 248,000 microwells. Unlike the existing serial-dilution process where dilution has to be repeated until monoclonality is acquired, this method allows assays of large number of living cells in parallel and so yields much higher unit assay screening throughput of more than 100,000 individual cells [2]. After the step 4 in the figure, the microarray of secreted products is printed on the glass slide corresponding to the locations of cells in the PDMS microwells, and this is why this technique is considered as a soft lithography. Since we can locate cells of interest in the PDMS stamp by comparing positions with the microarray on the slide, it is now important to be able to retrieve those cells individually.

2.2 Cell-retrieval Device

In the previous section, we learn that the microengraving technique enables high screening throughtput. However, in order to isolate a single cell for the further research, it is critical to have an accurate and high-throughput process of cell-retrieval. In this section, we introduce a commercial system that is currently used in the Love Lab for the cell picking. We then point out limitations of the system.

2.2.1 Functions of the CellCelector

Figure 2-2 shows the picture of the commercial system, CellCelector by Aviso. This system mainly consists of three parts: a robotic arm with a picking tool, an inverted microscope with a XY motorized stage, and destination plates. Based on the location information obtained from the screening process, the robotic arm moves to position the tip of the picking tool to a target well in a PDMS stamp. The main part of the picking tool is a glass micropipette whose end is pulled to have the diameter of 30 μm or 50 μm depending upon the target well dimensions. The target cells are retrieved by mechanical suction provided by a syringe system and moved to one of the multi-well plates in the destination area. The cell-retrieval process can be visualized through

Figure 2-2: Picture of the existing system, CellCelector.

the inverted microscope.

This existing device has its advantages in that it directly isolates individual cells without any pre-treatment of cells and it provides relatively more gentle harvesting than manual picks, thereby increasing cell viability. As for the accuracy, however, this system is structurally limited and this can have a negative effect on the automation of the process. The limitation of the system is discussed in the following section.

2.2.2 Limitations

Despite many advantages, the commercial system is severely challenged in terms of precision by its mechanism and structure. Figure 2-3 illustrates the mechanism of the robotic arm indicated in the green box in Figure 2-2. As shown in the figure, the structure of the system can be simplified as three links connected in a serial manner. While the first and second links as well as the second and third ones are fixed in position, it is notable that only the first link is actuated in all three degrees of freedom: up and down, left to right, and rotation. Since all motions are concentrated solely on the first link, it is more prone to error than having independent and uncoupled motions.

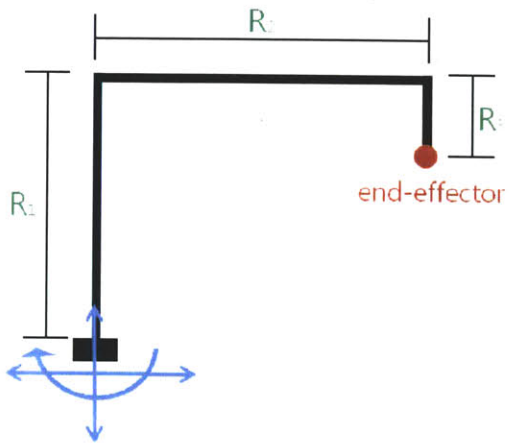

Figure 2-3: Mechanism for the 3-DOF positioner of the CellCelector.

Especially, the bearing implemented for the rotary motion has to carry the whole weight of the positioner, thereby making the system more vulnerable to position error. Now let us consider the case where the first link is tilted by a small angle, θ. Figure 2-4 depicts this situation.

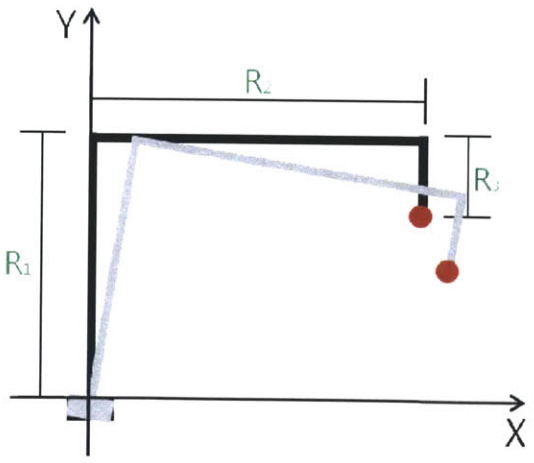

Figure 2-4: Small error in the first link causing large error at the end-effector.

As shown in the figure, when there is no error, the position of the end-effector indicated by the red dot is located at

$$\Big(R_2,\ R_1 - R_3\Big) \tag{2.1}$$

in the X-Y plane. However, with the small error, θ, the new location of the end-effector becomes

$$\Big(R_1 \sin\theta + R_2 \cos\theta - R_3 \sin\theta,\ R_1 \cos\theta - R_2 \sin\theta - R_3 \cos\theta\Big). \tag{2.2}$$

For small angle, Equation 3.7 can be linearized as

$$\Big(R_2 + (R_1 - R_3)\theta,\ R_1 - R_3 - R_2\theta\Big), \tag{2.3}$$

thereby making the position error as

$$e = \Big((R_1 - R_3)\theta,\ -R_2\theta\Big). \tag{2.4}$$

For the real system, the lengths of the first, second and third links are 15 cm, 20 cm, and 5 cm respectively, and let us assume we have the error of 1°. That is

$$\begin{cases} R_1 = 0.15 \text{ m} \\ R_2 = 0.20 \text{ m} \\ R_3 = 0.05 \text{ m} \\ \theta = 1^\circ. \end{cases}$$

Then we have the position error of

$$
\begin{aligned}
e &= \left((0.15-0.05)\frac{1\times\pi}{180},\ -0.2\frac{1\times\pi}{180}\right) \\
&= \left(1.75\text{ mm},\ -3.5\text{ mm}\right)
\end{aligned}
\tag{2.5}
$$

at the end-effector. Even if we have smaller error at the first link, for example, of $0.01°$, the final error at the end-effector would be still 17.5 μm for the vertical position and -35 μm for the horizontal position. These error values are not negligible the precision motion where submicron resolution is required. This structurally inherent error can be significantly reduced by making a small change on the structure design and we discuss this topic in more detail in the following chapter.

Chapter 3

Design Concepts and Component Selection

In this chapter, we discuss overall design concepts for the proposed system, robotic single-cell manipulator, and explain how we choose necessary components. The system requirements and required specifications of each component are also discussed in this chapter. We then detail how these components are implemented and integrated for the physical system in the following chapter.

3.1 Design Concepts

The robotic single-cell manipulator is a mechatronic system designed to provide high accuracy manipulation on microscopic objects such as cells and microbeads. For this purpose, a number of requirements of necessary components are considered with the fundamental design objectives of compactness, high accuracy, and high throughput.

Most importantly, we need a retrieval mechanism to pick up individual cells from PMDS microwells. Considering that a microwell has the depth of 30 μm or 50 μm and a mammalian cell is, in general, the size of 10 μm, the retrieval mechanism is required to have submicron resolution along the Z-axis motion. Also, this Z-axis actuator should have the travel length of at least 10 to 20 mm, since containers that hold PDMS stamps have wall height of about 10 mm. This retrieval mechanism has

to be mounted on a certain kind of plane motion stage in order for the end-effector to freely reach any microwells of interest to pick. Accordingly, this plane motion stage should have enough travel range to cover both the PDMS stamp and the 96 well plate, approximately 200 to 300 mm each axis. Resolution of this part does not have to be tight since a XY microscope stage will do the job of moving a PDMS stamp and locating the microwell of interest. One microwell has edges of 30 μm or 50 μm and one PDMS stamp containing hundred thousands of microwells has the size of 75 mm by 25 mm; therefore, the XY microscope stage should have enough travel range to cover at least one PDMS stamp, and the resolution of this motion is preferable to be on the order of 1 μm.

In order to show users the cell-retrieval process in real-time, a vision system such as a camera or a microscope is necessary. A camera alone or together with a zoom imaging lens is required to have submicron pixel size. The sensing area should be large enough to cover at least one block of microwells, which is 650 μm by 650 μm for 50 μm microwells or 690 μm by 690 μm for 30 μm microwells. An illuminator is also necessary to provide better contrast and clear images. In addition, we need a syringe system for the cell-retrieval task. Since the optimized amount of aspiration for cell-retrievals is 1 μL to 2 μL, the syringe system should have submicroliter volume resolution with a minimum flow rate of 0.2 μL/s because we do not want to spend too much time for one pick. The flow rate is preferable to be user-controllable.

All these necessary components need to be integrated with a central controller for user-friendly manipulations of the system. The hardware should have processors with large enough capability for control and vision, and the software should allow users to be able to integrate all the components with necessary controls and vision processing.

3.1.1 Design Options for the Cell Picker

A number of design options are considered to meet the design concepts and requirements of the robotic single-cell manipulator. The first design option, among many, considered for the system is illustrated in Figure 3-1. In this design, the inverse microscope and the structure carrying the Z-axis mechanism are fixed in position, and

all containers (PDMS microwells, 96 well-plates, and small containers for rinsing and sterilizing) are located in an XY positioning stage. After the microscope stage moves to locate a target microwell or 96 well-plate, the pipette module comes down and picks/places the target cell. While this design has the advantage of no movement overlaps along any axes, it also has a critical downside that the positioning stage has to become bigger and bigger for more PDMS stamps or 96 well-plates.

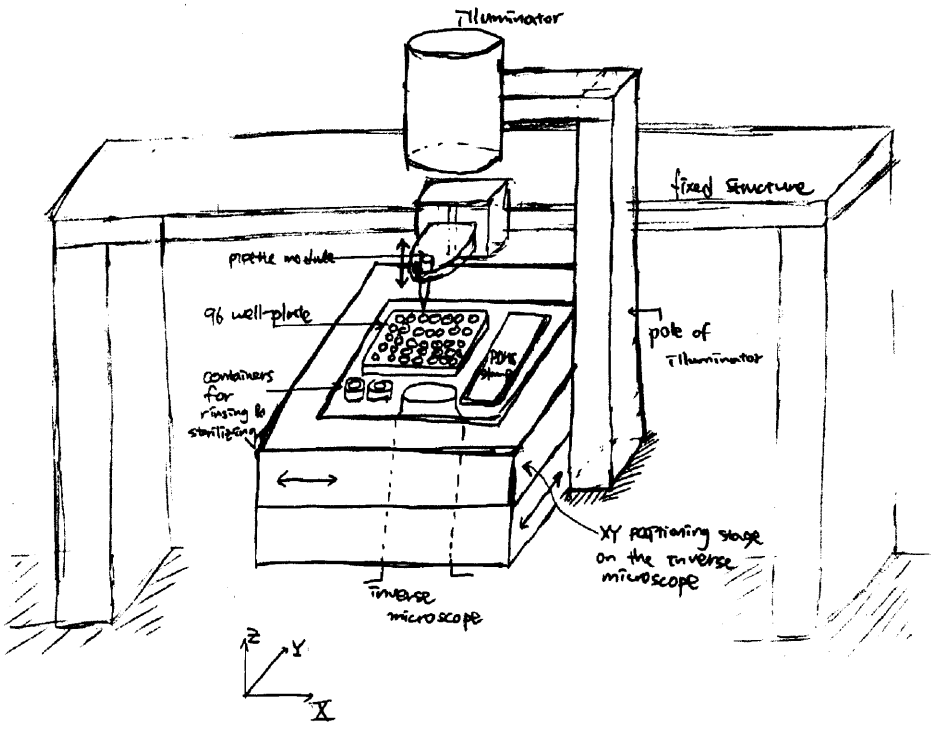

Figure 3-1: One design option considered for the robotic single-cell manipulator.

In order to overcome this drawback, we need to place 96 well-plates and small containers in another location, and this requires our system to have additional motion degree of freedom (DOF) since any retrieved cells from PDMS microwells have to be deposited in one of the 96 well-plates. This leads us to consider a gantry system as the next possible design, whose hand-sketch design is illustrated in Figure 3-2.

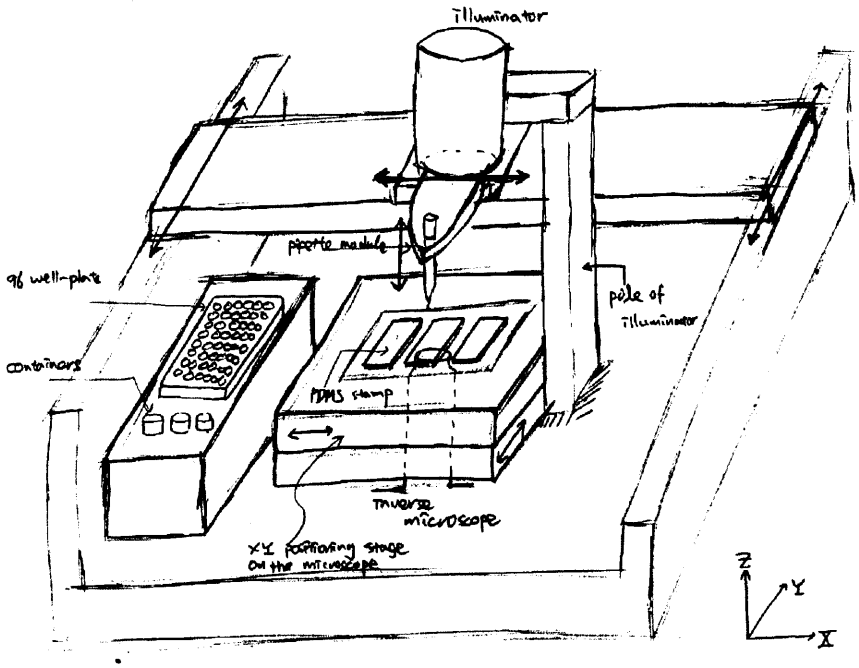

Figure 3-2: Design of gantry configuration for the robotic single-cell manipulator.

This design allows the pipette module to have all 3 DOF along X, Y, Z axes, and so there are movement overlaps between the gantry and the positioning stage along the X and Y axis. This downside is, however, inevitable when we have PDMS stamps and 96 well-plates located in different places. Advantages of this design lie in the fact that gantry systems are commercially available and can easily have the submicron resolution which is more than enough for our application. However, it is notable that the upper stage of the gantry system can have a physical collision with the illuminator. When the pipette module needs to move along the Y-axis, the whole upper stage has to slide and the range of this motion is greatly limited by the illuminator's structural support pole shown in Figure 3-2.

Another design of a T-drive system, illustrated in Figure 3-3, can remove this collision issue and provide freer movement along the Y-axis. This T-drive system is basically a combination of two linear stages with the upper one inverted so as

to reach into the inverse microscope and the 96 well-plates. This design can be a good choice for our system because many commercial linear stages are available at reasonable prices and the configuration is easy to build. Also, we can make a compact and accurate system out of this design with the right choice on linear stages, which is discussed in the following section.

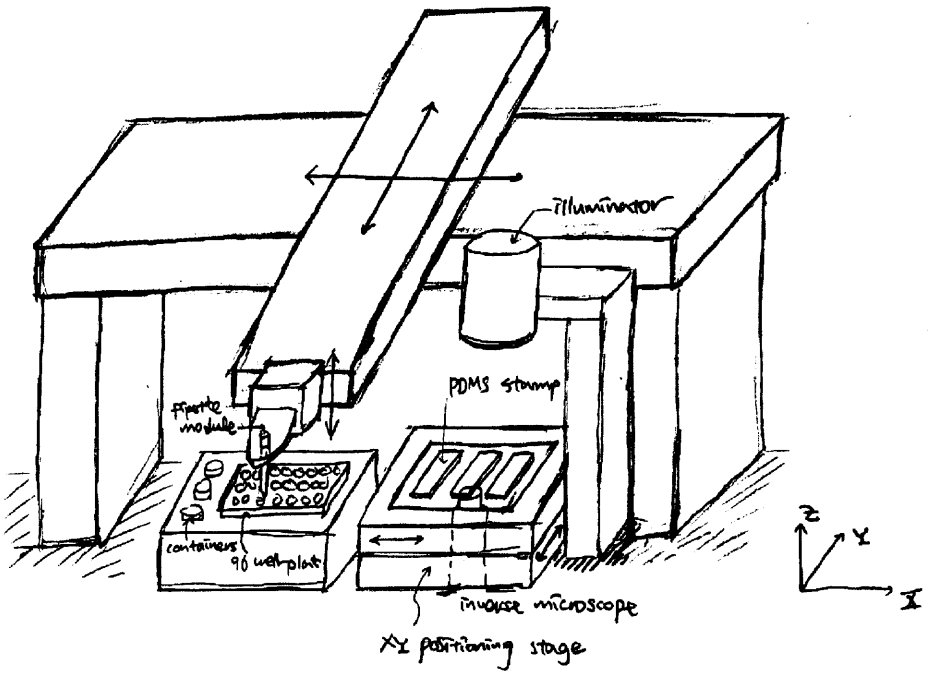

Figure 3-3: Design of T-drive system for the robotic single-cell manipulator.

Among many options, we here choose the T-drive mechanism for our system design and we show the CAD model for this design in the next section with explanation on selected components.

3.1.2 Conceptual Configurations

Among several options for the proposed system, robotic single-cell manipulator, the T-drive mechanism is selected because it is easy to build with commercially available

linear stages and also can be integrated within a compact footprint. It also gives opening in the front area for users to work freely on the 96 well-plates and the PDMS microwells. The conceptual CAD design is shown in Figure 3-4 below. The footprint of this system is 670 mm $\times$ 800 mm.

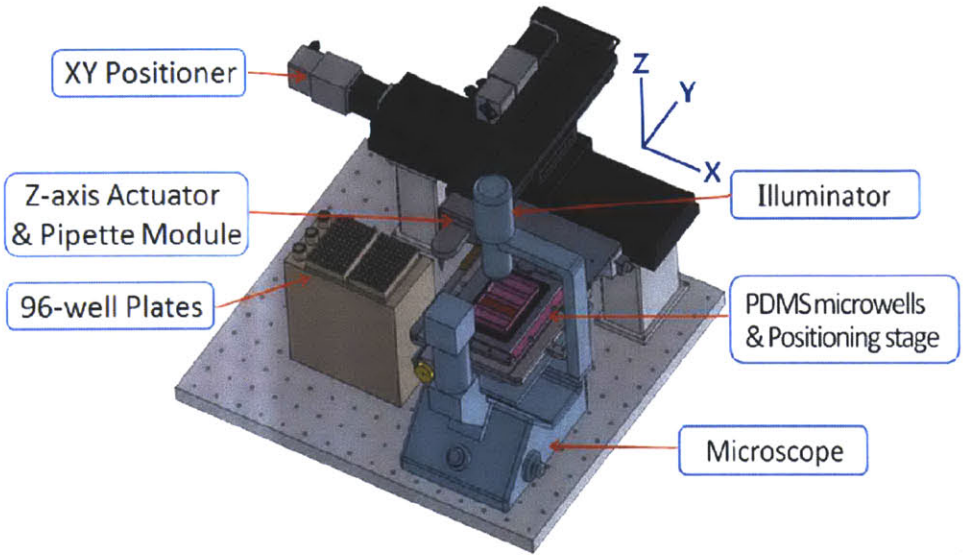

Figure 3-4: Conceptual configurations for the robotic single-cell manipulator.

In this concept, which has not been constructed, the XY positioner of Figure 3-4 is composed of two linear stages from Aerotech: PRO 165-400 for X-axis motion and PRO 115-200 for Y-axis motion. The Y-axis stage has a foldback which uses a timing belt to connect the parallel shafts of the ballscrew and motor so that we can save unnecessary space in the back. However, if the compactness is not a critical factor in design, it is more suggested not to use the foldback since it causes additional flexibility in the drivetrain which can degrade performance. Another noticeable design point is that a bigger stage, PRO 165-400, is selected for the X-axis motion. This is partially because we need longer travel length along the X-axis line, but more importantly, this bigger stage augments the roll stiffness which is significantly necessary in this configuration. As explained earlier, the resolution of the XY positioner does not have

to be tight for the cell-retrieval process; however, for future purposes such as the deterministic cell-depositing task, it is preferable to have submicron resolution. This is why the PRO series from Aerotech are selected for the system. Both PRO series have the resolution and accuracy of 0.5 μm and ± 8 μm respectively and the maximum speed of 300 mm/s. Detailed specifications for these stages are provided in Appendix B.

The pipette module and the Z-axis mechanism are simplified in the figure and this part is detailed in the following section and Chapter 4. The inverse microscope in the figure is also a simplified version of an Olympus CKX 41 which has a positioning stage on it. The XY microscope positioning stage in this concept is a SCAN IM from a German company Marzhauser which has the resolution and acceleration of 50 nm and $1 m/s^2$, respectively. The information on detailed specifications of both products is provided in Appendix B. Instead of using this commercial inverse microscope, however, we plan to design and construct our own microscope, for the prototype, with a camera, a zoom imaging lens, and a microscope stage. We discuss this self-designed microscope in detail in the following section and Chapter 4.

3.2 Z-axis Mechanism Selection

We use a syringe system for the pick-and-place tasks and the end-effector which is the tip of a glass micropipette should be able to approach a microwell of interest to pick a target cell. It therefore requires Z-axis motion as well as XY plane motion. Many design options are considered for the Z-axis mechanism to provide the tip accurate access to the Z-axis motion. In this section, we discuss these options and how we select one among them.

3.2.1 Mechanism Options

There are a number of mechanisms that can be used for the Z-axis motion. Without pondering too much on advantages and disadvantages, any possible approaches are first considered from a regular direct current (DC) motor to a linear pneumatic

actuator. These options are then categorized to two groups. Figure 3-5 shows the linear mechanism category for the Z-axis movement. The figures show the end of the Y-axis stage with a linear voice coil mechanism, lead-screw system, and a pneumatic actuator implemented respectively.

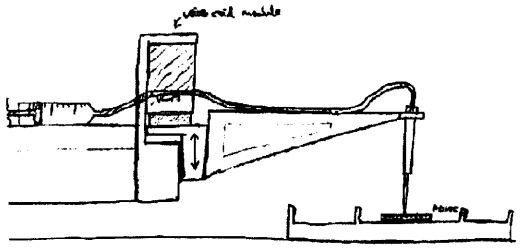

(a) Linear voice coil motor

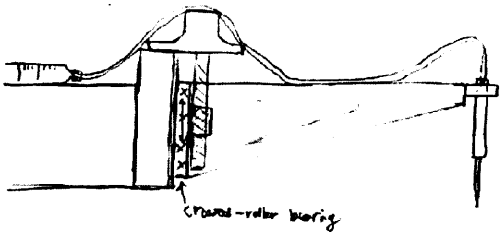

(b) Lead screw mechanism

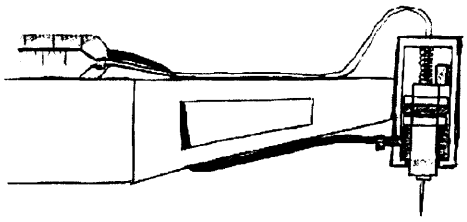

(c) Pneumatic actuator

Figure 3-5: Linear mechanism options considered for the Z-axis motion.

These options are very practical in that they directly provide vertical motion and have inherently perpendicular instantaneous velocity of the tip when touching the surface of PDMS stamps. The other category is for the rotational mechanisms,

shown in Figure 3-6, containing a regular DC motor system, a DC motor with a four-bar linkage, and a voice coil actuator mechanism.

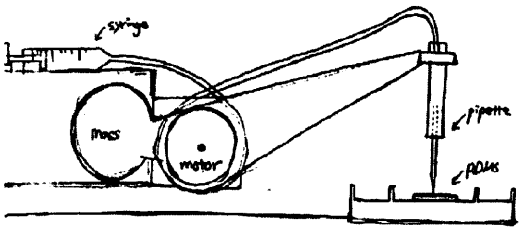

(a) Regular DC motor

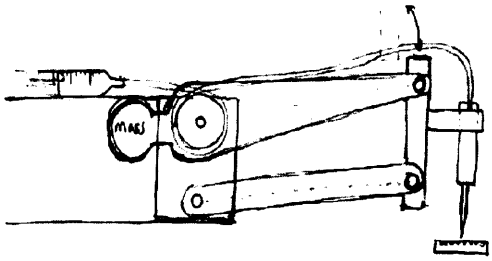

(b) Four-bar linkage

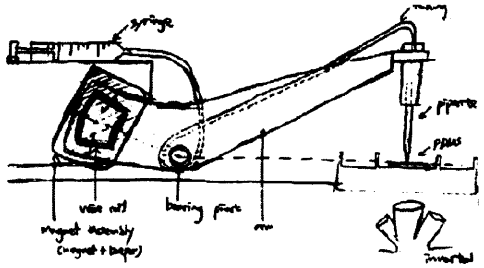

(c) Voice coil motor

Figure 3-6: Rotational mechanism options considered for the Z-axis motion.

These rotational mechanisms, except for some four-bar linkage systems, cannot provide linear motion; however, given that we only need a travel length of 10 to 20 mm, which is much smaller than the arm length (150 to 200 mm), the motion can be

close to straight line.

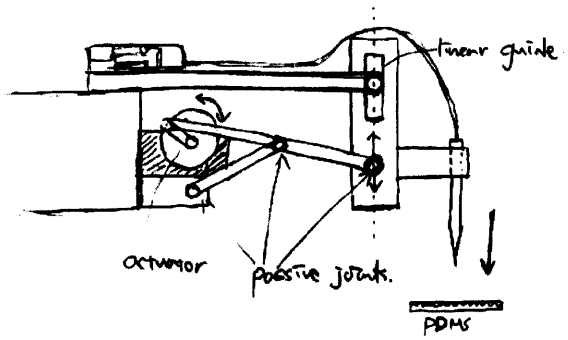

(a) Hoekens linkage

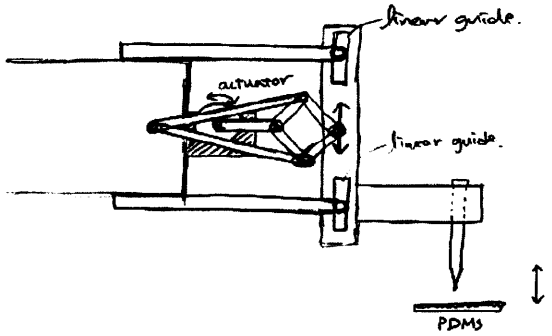

(b) Peaucellier-Lipkin linkage

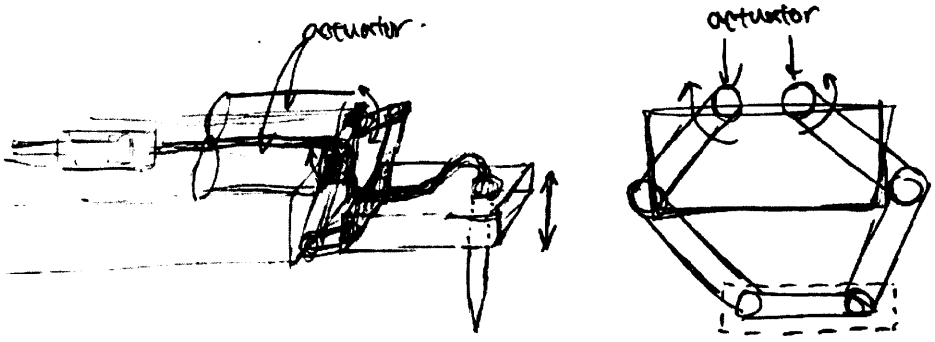

(c) Sarrus linkage or double SCARA

Figure 3-7: More options for the Z-axis motion with four-bar linkage structure.

In the brainstorming process, we also considered four-bar linkage systems giving very linear motion in more detail, shown in Figure 3-7. For example, the Sarrus

linkage and Peaucellier-Lipkin linkage create linear motion while the Hoekens linkage provides nearly straight line motion. However, for such a short range of 10 to 20 mm, using and implementing a four-bar linkage structure on the end of the Y-axis stage seem too complicated and not practical. Also, the linear guide will be hard to build with sufficient accuracy.

Before comparing pros and cons of each one of the options, we need to decide which group, either linear mechanism or rotational mechanism, can be a better choice in terms of reaction to the system and concern of error. For this purpose, let us consider the Y-axis stage on which the Z-axis mechanism is mounted as a cantilever beam with one end fixed. This cantilever beam would experience vertical reaction force when a linear mechanism actuates the end-effector up and down while it would be exposed to reaction torque or moment when a rotational mechanism actuates the tip. These are illustrated in Figure 3-8 along with the maximum amount of deflection in each case.

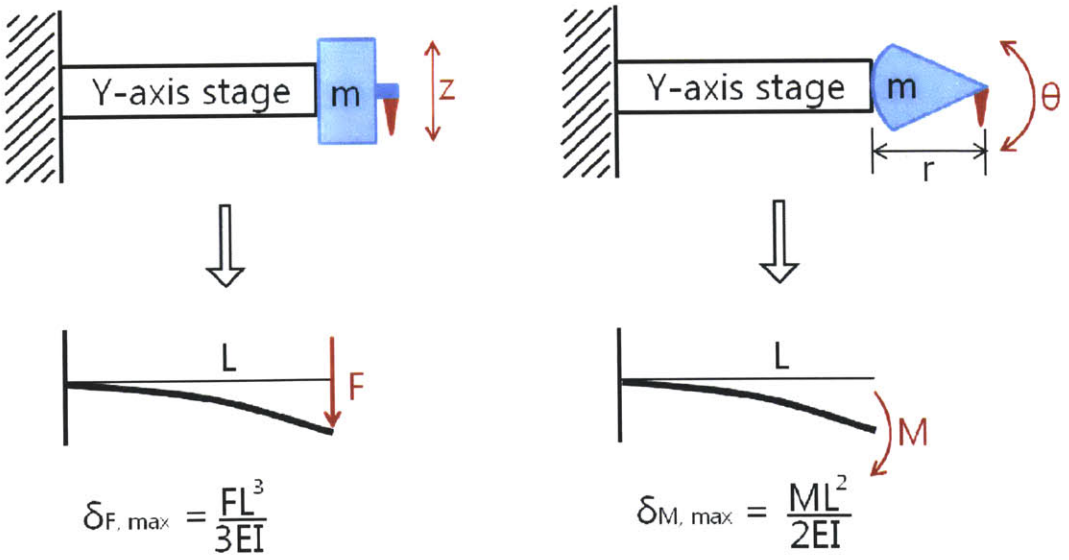

(a) Reaction force

(b) Reaction torque

Figure 3-8: Cantilever beams under the vertical reaction force and the reaction torque.

In both figures above, the cantilever beam has a length L, Young's modulus E,

and area moment of inertia I. The additional structures for the linear or rotational motion are assumed to have the same mass m, and the reaction force and moment are assumed to be exerted on the end of the cantilever, which models the Y-axis stage. In the figures, the maximum deflections under the reactions are expressed in terms of the parameters [8]. In order to compare the deflection level, we need to find a link to connect the force, F to the moment, M. This link can be found by considering the fundamental condition for the Z-axis movement. The basic requirement for the end-effector is to move a certain distance within a certain amount of time. That is, if we want to locate the tip at the distance of d in the required time of t under the assumptions of initial rest and the constant acceleration of a, the distance and the acceleration are expressed as

$$d = \frac{1}{4}at^2 \quad , \quad a = \frac{4d}{t^2}. \tag{3.1}$$

The force required is therefore

$$F = ma = m\frac{4d}{t^2}. \tag{3.2}$$

As for the reaction torque, the angular acceleration, α is, in the same manner, expressed as

$$\alpha = \frac{4d}{rt^2} \tag{3.3}$$

where r is the rotation system tip to center distance.

With the worst case scenario for the rotational mechanism, the total mass of the extra structure m is considered to be concentrated at the end as a point mass. Thus the mass moment of inertia, J is equal to mr^2. The torque needed to move the tip to the distance d is therefore

$$M = J\alpha = mr^2\frac{4d}{rt^2} = mr\frac{4d}{t^2}. \tag{3.4}$$

Accordingly, the relation between the force and torque is simply

$$M = rF. \tag{3.5}$$

With this relation, we can decide which case has the larger deflection by looking at the difference between $\delta_{F,max}$ and $\delta_{M,max}$. If this difference is positive, the linear mechanism causes worse reaction to the system with larger deflection, thereby making the rotational mechanism a better choice. Otherwise, the opposite conclusion can be made. The difference is

$$\delta_{F,max} - \delta_{M,max} = \frac{FL^3}{3EI} - \frac{ML^2}{2EI}. \tag{3.6}$$

After substituting M with Equation 3.5, canceling out terms and reorganizing, the difference becomes

$$\frac{2L}{3} - r > 0. \tag{3.7}$$

Since the arm (length of r) of the rotational mechanism is much shorter than the length (L) of the Y-axis stage, it can be said that the inequality of Equation 3.7, in general, is true and the rotational mechanism exposes less reaction and less deflection to the system. This is especially true when we can always reduce the length r by implementing a counter-balance mass because the value r is just the distance between the rotation axis to the center of mass. As a result, we can now choose the rotational mechanism group over the linear one.

Now, we need to choose one mechanism within the group shown in Figure 3-6. First, even though the four-bar linkage structure can provide relatively more straight motion to the tip, it is not very efficient to build this complicated structure for such a short travel length of 10 to 20 mm. As for the general DC motor case, it does have the advantage of easy installation; however, it is not a direct drive and so can have a backlash problem which can cause large enough error to the end-effector's motion. With other options ruled out, the voice coil actuator with the advantages

of both straightforward installation and direct derive is then selected as our Z-axis mechanism to give the accurate tip movement.

3.2.2 Actuator and Sensor

Now that we chose the Z-axis mechanism, we need to either build a voice coil actuator or find a commercially available one. Luckily we found an old hard disk drive manufactured by IBM, shown in Figure 3-9, which has a well-constructed electromagnetic motor with a well-built-in bearing.

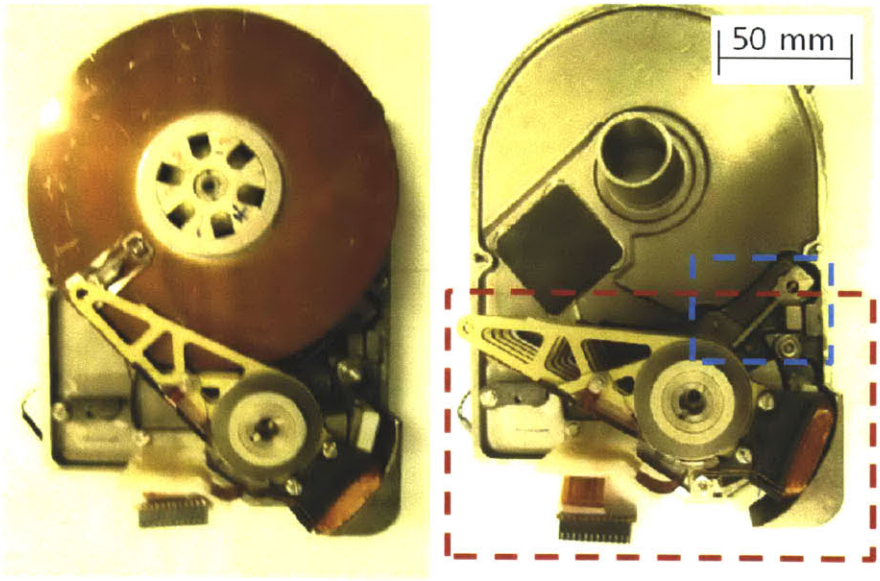

(a) with disks (b) disks disassembled

Figure 3-9: Built-in voice coil actuator in a hard disk drive.

The built-in voice coil actuator that we plan to use is indicated inside of the red box in Figure 3-9(b). It is notable that this device has the mechanical stop system indicated inside of the blue box. This stop system is there to prevent the coils from coming out of the magnet part. We do not mind to have this extra structure since we need only 10 to 20 mm travel length along the Z-axis line which corresponds to less than 20° given our designed arm length. In fact, we later use this hard stop as a

reference point of the Z-axis motion and this is detailed in Chapter 4.

While a current hard disk drive generally has the same kind of actuator with the arm of about 35 mm, this old hard disk drive has fairly big one with the 85mm-long arm and it actually makes this old device a better choice for our Z-axis actuator because it can be directly used with simple arm extensions. Figure 3-10 shows the CAD model of the actuator and several components for the extension we designed for this mechanism.

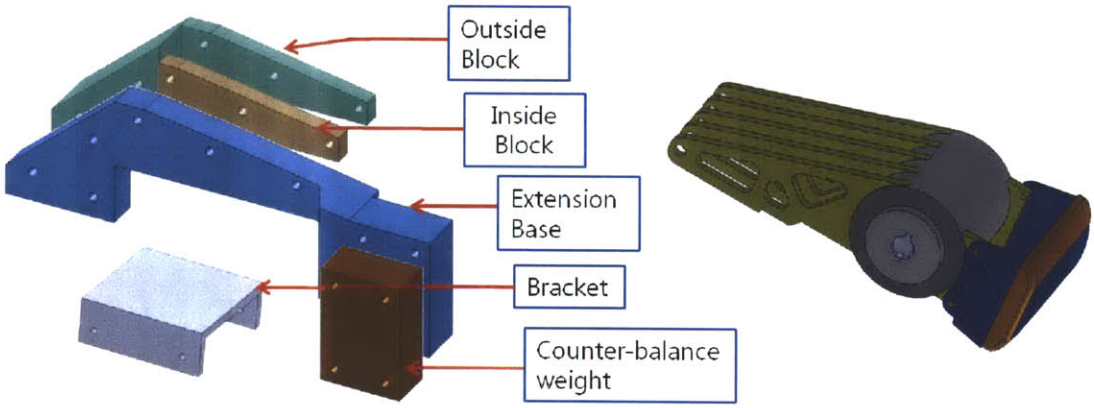

Figure 3-10: Arm extension design for the voice coil actuator.

The arm extension is designed to have several separate components rather than a single body for manufacturing purposes. By separating parts, it becomes easier to manufacture; the extension base can be first cut with a water-jet and then milled to have different height and necessary holes in required positions. The inside and outside blocks can be also manufactured in the same way. As for the bracket, a thin aluminum plate is first milled and then bent to have 90° angles. Every parts except for the counter-balance block are designed to be manufactured with aluminum alloy 6061 for its light-weight (density of 0.0027 g/mm^3) and good machinability. On the other hand, the counter-balance block is designed to be manufactured with brass alloy 360 for its higher density (density of 0.0085 g/mm^3) and good machinability. The extension parts together with the bracket play a role to provide stiffness in all

possible directions and the counter-balance block is there to simply balance the arm. The importance of counter-balance is detailed in Chapter 4.

The assembled CAD model for the arm is shown in Figure 3-11 below. This figure also shows the pipette module mounted on the extension. The pipette module and its sealing components are discussed in Chapter 4 in detail. The total arm length from the shaft to the tip is 140 mm. We show the manufactured and assembled physical system in Chapter 4.

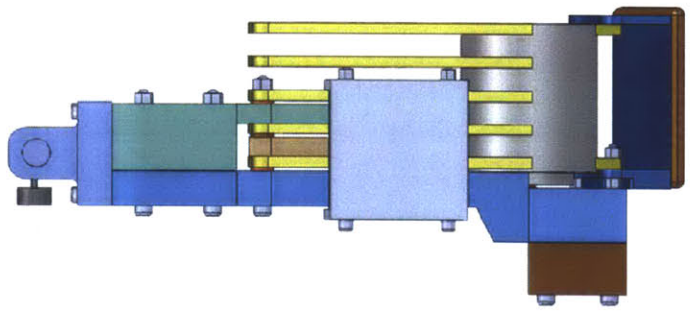

(a) Top view

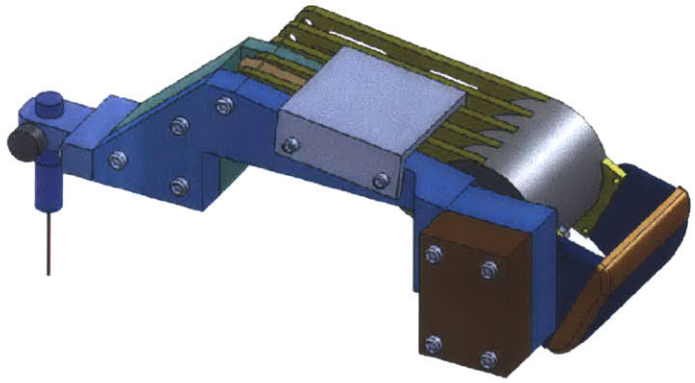

(b) Isometric view

Figure 3-11: Assembled CAD model for the Z-axis actuator with arm extension.

3.3 Microscope and Microscope Stage

As explained before, we decide to design and construct our own microscope for the prototype instead of using a commercial one such as Olympus CKX 41 used in our

conceptual design in Figure 3-4. In this section, we discuss necessary components for an inverse microscope and their requirements. We also present the conceptual design in this section and the actual microscope system constructed is detailed in the following chapter.

3.3.1 Desired Specifications

The basic purpose of an inverse microscope is simply to provide users access to images of specimens, which are, in our case, cells in PDMS microwells with the size on the order of 10 μm. Accordingly, in order to design our own microscope, the most fundamental components we need are a camera and a zoom imaging lens which have enough specifications to capture images of microscopic objects. The selected components including a camera, a lens, and other necessities are shown in Figure 3-12 below.

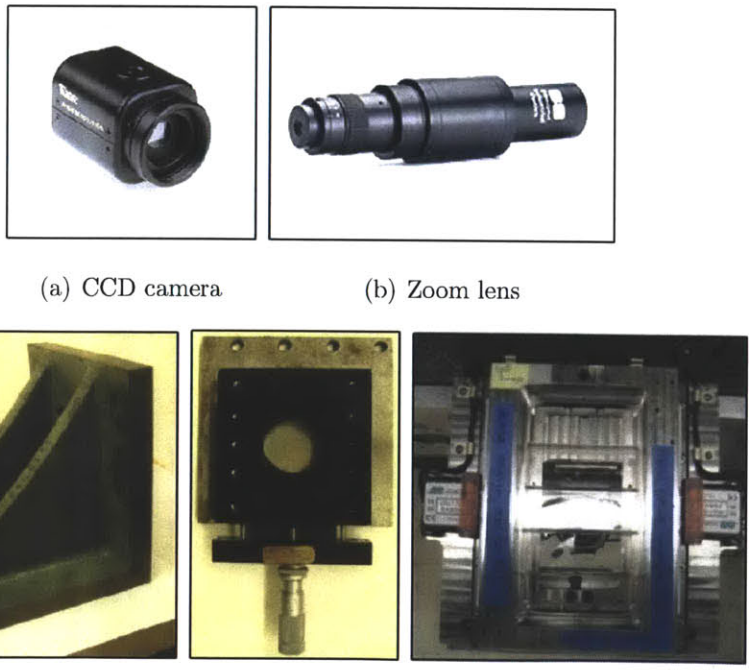

(a) CCD camera (b) Zoom lens

(c) L-shape bracket (d) Focus stage (e) XY stage

Figure 3-12: Components for the self-designed inverse microscope.

The camera shown in Figure 3-12(a) is a charge-coupled device (CCD) monochrome

camera, Watec 902C. It has 768 × 494 pixels with the size of 8.4 × 9.8 μm each. Accordingly, only with this camera, it would be hard to capture clear images of 10 μm cells. This is why we need a zoom imaging lens, shown in Figure 3-12(b), which has a magnification level of 2.5× up to 10×. This lens is VZM 1000 model from Edmund Optics and the detailed specifications of the camera and lens are provided in Appendix B. Together with this lens, the camera can achieve a sensing area of 0.64 × 0.48 mm with the smallest pixel of 0.84 × 0.98 μm, which is enough to observe micrometer-sized objects. Since the zoom imaging lens has a specific working distance of 35 mm with the tolerance of ±1 mm, it would be of great help to have a command of adjusting this distance. The focus stage, shown in Figure 3-12(d), is used for this purpose. The L-shape bracket with opening in Figure 3-12(c) is the body of the self-designed microscope and provides a structural base for the microscope positioning stage, shown in Figure 3-12(e). This positioning XY stage has several piezoelectric motors in it and this is detailed in Chapter 4.

3.3.2 Inverse Microscope Design

We conceptually assemble those components explained in the previous section with a CAD tool and Figure 3-13 below illustrates the assembled model for our self-designed inverse microscope.

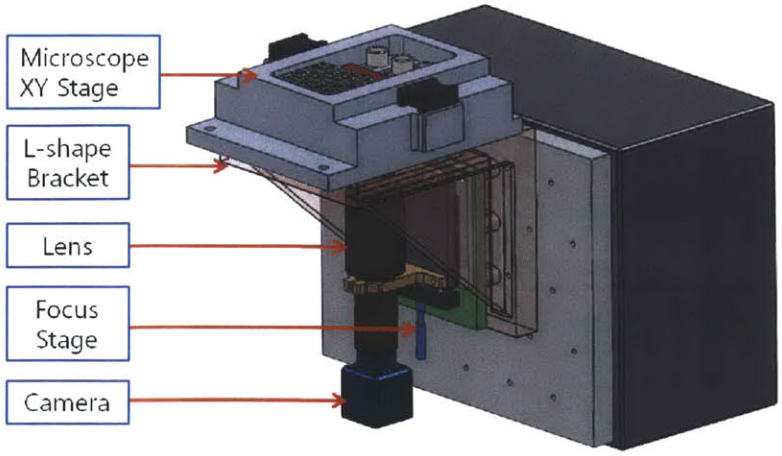

Figure 3-13: Assembled CAD model for the self-designed inverse microscope.

First, the L-shape bracket is mounted on the side of a granite table with the opening area facing upward. The focus stage with the camera and lens mounted is then assembled so that the lens is located in the middle of the bracket's opening. Lastly, the microscope positioning stage is mounted on the bracket. In the figure, a 96 well-plate, a PDMS stamp, and several small containers are located in the stage. We also plan to add an illuminator to this system. In Chapter 6, we discuss the illumination in more detail. The physical system for this inverse microscope has been built and we discuss it more in the following chapter.

Chapter 4

Mechanical Design and Implementation

In this chapter, we discuss how the conceptual design of the proposed system and selected components detailed in the previous chapter are used to construct the prototype of the system. We then explain several important parts of the prototype in more detail and talk about how they are implemented. A critical issue of the existing commercial system is also addressed in this chapter with suggested solutions and supporting experiments.

4.1 Prototype of the Single Cell Picker

Conceptual configurations for the proposed system, robotic single-cell manipulator, are designed and discussed in Chapter 3, and here we present the prototype for the system. This prototype has been constructed mainly to see the feasibility and performance of the proposed system and it focuses largely on the accuracy of the Z-axis movement. For the prototype, the XY positioner in Figure 3-4 from Chapter 3 is replaced with mechanical XY stages and the inverse microscope has been self-designed and constructed with a simple monochrome camera, a zoom lens, and a XY microscope stage. More importantly, the Z-axis mechanism part together with the pipette module has been built and mounted on the XY mechanical stages. This

part mainly consists of the voice coil actuator from an old hard disk drive selected in the previous chapter, an arm extension, and an optical encoder. We discuss each component and their implementations in detail in the following sections. Figure 4-1 below shows the prototype of the robotic single-cell manipulator.

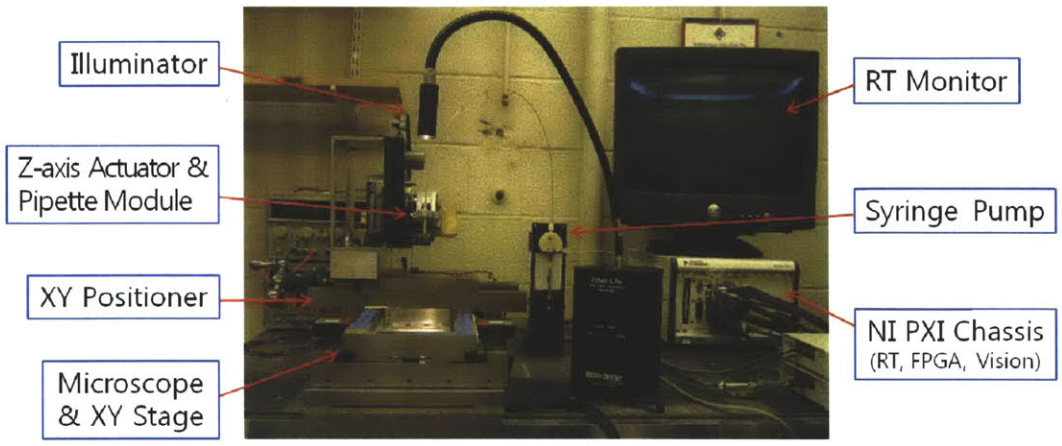

Figure 4-1: Physical configurations of the prototype.

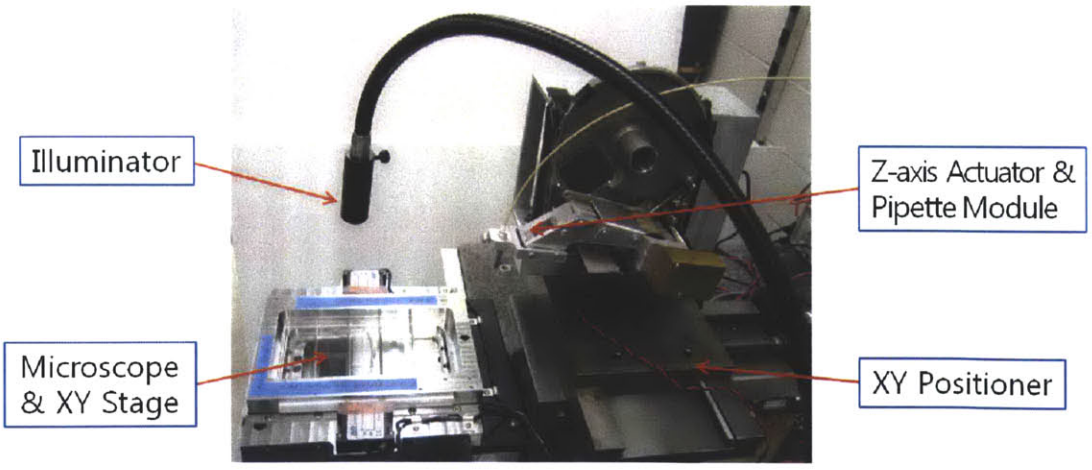

Figure 4-2: Partial configurations of the microscope and z-axis mechanism.

The main controller for this prototype, shown in Figure 4-1, is a National Instruments (NI) PXI controller containing a real-time processer, a field-programmable gate

array (FPGA) card, and an analog vision card. Labview is used as a programming tool for this controller and we discuss how the entire prototype is integrated with this PXI controller in the following chapter. A syringe pump is used with polyether ether ketone (PEEK) tubing in order to be able to aspirate and dispense individual cells or microbeads from the PDMS microwells to the 96 well-plates. An illuminator is also included to provide better contrast for the microwells' images captured from the inverse microscope. Detailed information on these parts is provided in the following sections. Figure 4-2 shows the Z-axis mechanism and the pipette module part in more detail.

4.2 Picking Method

4.2.1 Syringe Pump

An original equipment manufacturing (OEM) syringe pump with 60 mm stroke is used in the prototype for the process of cell-retrievals. This syringe pump, Cavro XLP 6000, driven by a stepper motor with a Teflon coated leadscrew controls the volume of growth medium aspirated with a cell and the flow rate as well. Together with a 50 μL syringe, this device has the approximate resolution of 1 nL and the average speed range of 5.2 nL/sec to 42 μL in the 48000 microstepping mode. All these settings can be controlled with a simple serial communication using RS-232 at a baud rate of 96000. Figure 4-3 below shows a picture of the syringe pump. As shown in the figure, this device includes a multi-channel valve system so that the growth medium can be automatically refilled; one valve is connected to a medium reservoir and another to the pipette module through PEEK tubing. As explained, all the commands can be sent to the syringe pump through a RS-232 serial communication and we built an user interface (UI), shown in Figure 4-4, with Labview to command this device. The detailed Labview coding is provided in Appendix A.

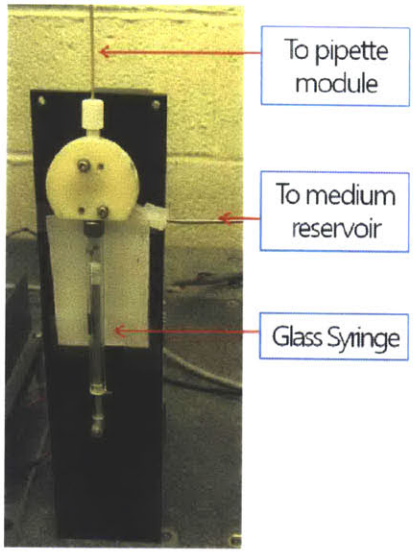

Figure 4-3: OEM syringe pump for the process of cell-retrievals.

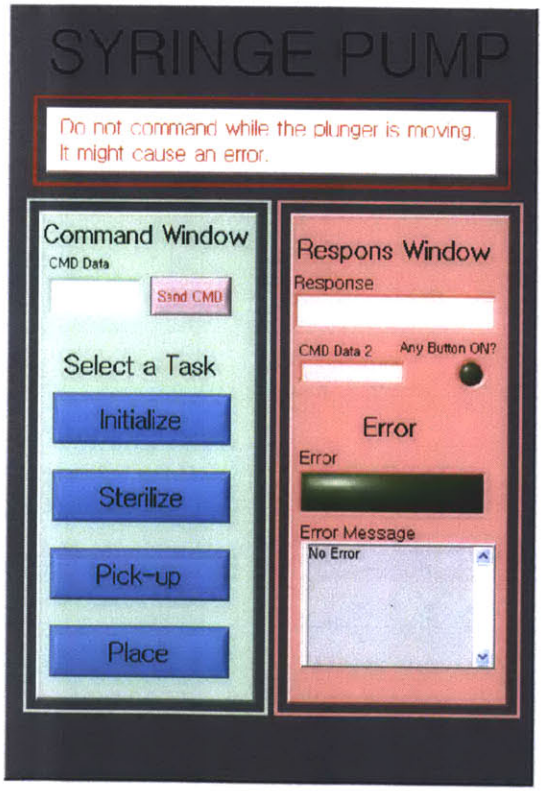

Figure 4-4: User interface control panel for the syringe pump.

4.2.2 Issues with Leakage

In using a syringe pump and running a liquid to pick and place a cell or microbead, it is important to make sure that all components are appropriately connected and sealed. This is especially true when the device runs under high pressure conditions. Since micropipettes used for cell-retrieval process have a very small tip opening of 30 μm or 50 μm, the pipette module is inevitably exposed to relatively high pressure during the process of cell-retrieving and disposing. Any failure on sealing, therefore, can cause serious leakage problem, thereby bringing about poor cell-retrieval performance. Figure 4-5 shows a picture of the commercial system with the types of the fittings used in it.

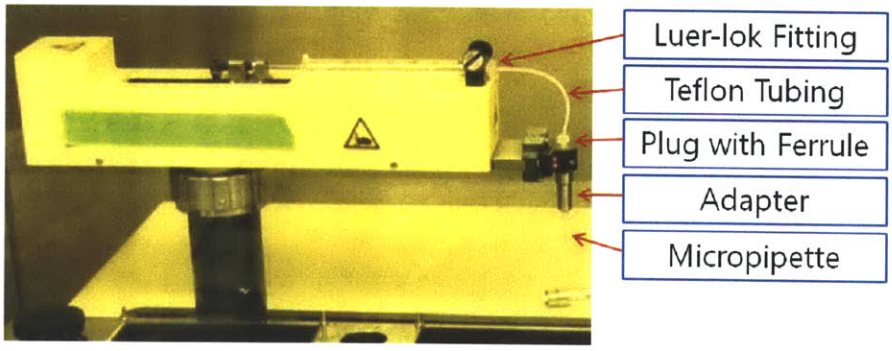

Figure 4-5: Cellcelector with its sealing components.

As indicated in the figure, in the CellCelector, a glass syringe is mounted on a syringe pump and connected to a micropipette through several fittings. Teflon tubing with a Luer-lok fitting connects the glass syringe to an adapter. The Luer-lok is a standard fitting which provides the connection between the syringe and the tubing, and the other end of the tubing is connected to the adapter with a plug and an inside ferrule. A micropipette is also attached to the other end of the adapter with a plug and a ferrule to make sure that the liquid from the glass syringe only runs to the tip of the pipette. However, leakage has been detected in the existing system while running from the point where the Teflon tubing is connected to the adapter. This leak point

is illustrated in more detail in Figure 4-6. This leakage issue has been observed with both 30 μm and 50 μm-OD micropipettes, but more seriously with the 30 μm one.

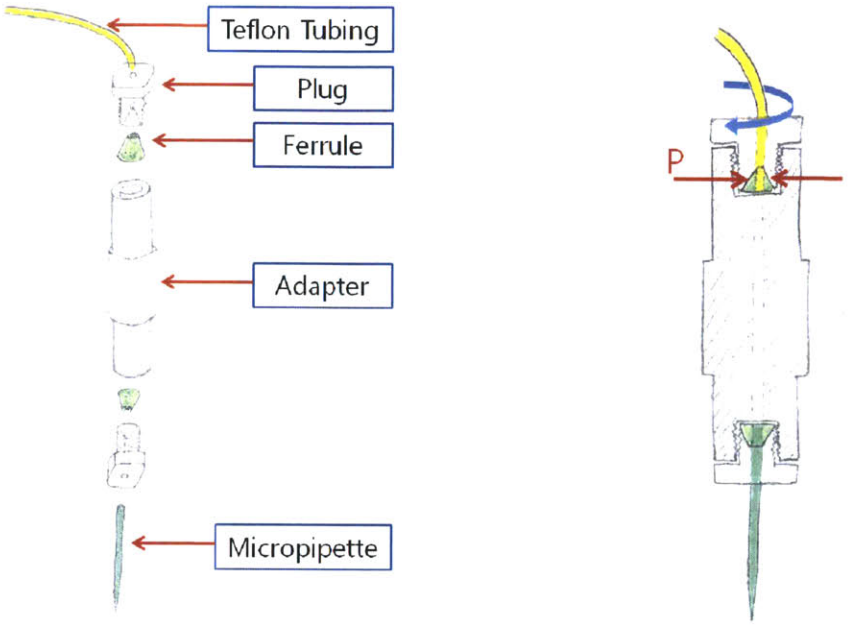

(a) Unassembled (b) Assembled

Figure 4-6: Schematic of how fittings work to seal the pipette module.

Figure 4-6(a) shows the positions of the fittings just before assembly and Figure 4-6(b) indicates the cross-section of the assembled pipette module. As shown in the figure, the inside ferrule is the main component for sealing between the tubing and the adapter. When the plug is fastened, it presses the ferrule so that the ferrule can seal the tubing by squeezing it. This squeezing effect is indicated as horizontal pressures with red arrows in Figure 4-6(b). Even though the pipette is connected to the adapter in the same way the tubing is, the leakage mostly occurs at the point where the tubing meets the adapter. This makes the material of tubing, which is Teflon, a likely cause of failure. Teflon is actually the brand name of the DuPont Company, for polytetrafluoroethylene (PTFE), and this material is commonly used in chemistry and biology due to its good chemical resistance. However, when it comes to mechanical properties, Teflon has a relatively small yield strength compared to other polymers such as PEEK. The compressive yield strength of Teflon is 10

to 15 MPa while PEEK has the compressive yield strength of 118 MPa [9][18][19]. That is, when the ferrule squeezes the Teflon tubing as shown in Figure 4-6(b), the pressure exceeds Teflon's yield strength at some point and the tubing deforms instead of holding the pressure and being sealed. This is why the leakage occurs at the point where the tubing and the adapter meet. Also, more serious leakage is detected with smaller (30 μm-OD) micropipettes since the smaller the opening is, the higher the liquid pressure is on the Teflon tubing.

In order to confirm this cause and suggest possible solutions, we conduct simple experiments. Figure 4-7 illustrates the experimental settings: Figure 4-7(a) with Teflon tubing and Figure 4-7(b) with stainless steel tubing. The stainless steel tubing is used as a possible solution for the replacement of Teflon tubing since stainless steel has much higher yield strength than Teflon: 240 MPa for commonly used 304 stainless steel [20].

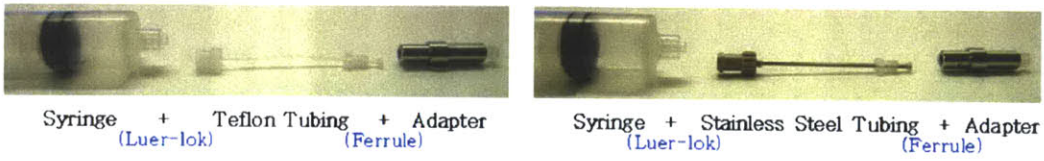

(a) Teflon tubing (b) Stainless steel tubing

Figure 4-7: Sealing test setup with two different materials of tubing.

As shown in Figure 4-7(b), the stainless steel tubing has the same outer diameter as the Teflon tubing, 1/16 inch, and a Luer-lok adapter is utilized to provide the same condition of the sealing as the existing one. The contact information of the vendor for this microfluidic component is provided in Appendix B. The lengths of both tubings are also set to be the same and the other end of the adapter is blocked, in both cases, with a plug so that the sealing parts experience high pressure.

With this setting, a sealing test is conducted in the way illustrated in Figure 4-8. To do the test under the same conditions, we tried to fasten all fittings with the same torque and to apply the same amount of pressure to both syringes.

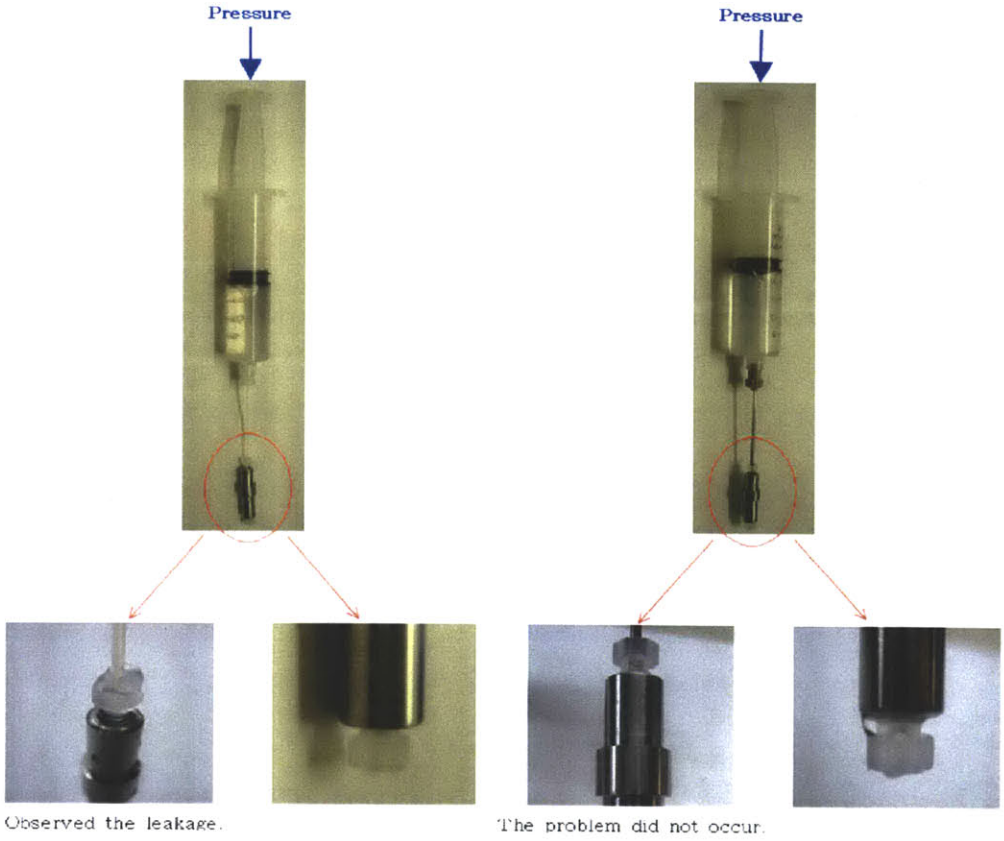

(a) With a teflon tubing (b) With a stainless steel tubing

Figure 4-8: Sealing test with two different materials of tubing.

As shown in Figure 4-8(a), the Teflon tubing brings about the leakage problem as expected; however, the test with the stainless steel tubing does not show any leakage at the point where the tubing is connected to the adapter. Rather, when we pressed the syringe with much higher pressure, the blocked end had a little bit of leakage. We also tried with a PEEK tubing of the same diameter in the same settings and did not observe any leakage either. As a result, we come to the conclusion that the leakage problem in the existing system, CellCelector, is caused by the relatively small yield strength of the tubing material, Teflon, and this issue can be resolved by changing the material to PEEK or stainless steel. The information about vendors for PEEK and stainless steel tubing is provided in Appendix B.

After confirming that the leakage issue is from the tubing material, we built a

tubing prototype with commercially available stainless steel tubing and tested it with CellCelector to see if stainless steel tubings can also do the task without any unexpected problems. Figure 4-9 shows two different shapes of the tubing prototype implemented on the current system.

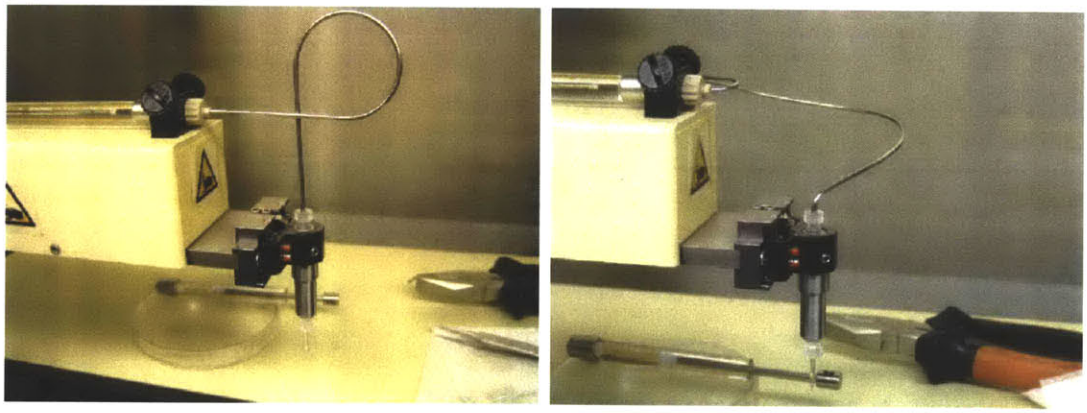

(a) Prototype#1 (b) Prototype#2

Figure 4-9: Implementing new tubing prototypes on the CellCelector.

Figure 4-9(a) shows the first trial of the prototype. The loop shape is made to reduce the tension. Although this prototype is constructed with a hardened stainless steel tubing, we suggest to use annealed tubing since it would be much easier to handle and bend into a desired path. The first trial did not cause any leakage problem. However, it had an issue for the actual cell-retrieval process. Since the existing system has small clearance between the illuminator and the microscope stage, the first trial of the prototype had a collision with the illuminator while running for the cell-retrievals. Accordingly, the second prototype is designed to avoid this collision and tested for the cell-picking process. Figure 4-10 below shows the experimental result with this new stainless steel tubing prototype.

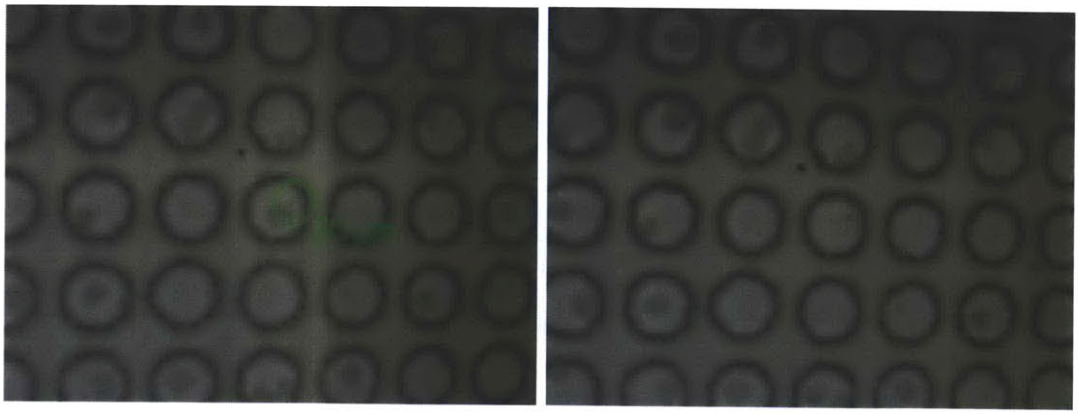

(a) Before retrieving (b) After retrieving

Figure 4-10: Testing cell-retrievals with a new tubing prototype.

As indicated in Figure 4-10(a), a 30 μm-OD micropipette is used for this experiment and the green circle illustrates the position of the pipette tip. As shown in Figure 4-10(b), the cell placed in the well near the green circle is removed, suggesting a successful pick. The same process was conducted five times in a row and all trials were successful with no leakage issue occurred during the process. In addition, the same experiment was performed with a PEEK tubing and the result was also positive. This change of tubing should be included as the standard connection in the CellCelector.

4.3 Z-axis Mechanism

In this section, we discuss in detail the main components of the Z-axis mechanism: the actuator and the sensor, and also explain how we implement them.

4.3.1 Voice Coil Actuator

As discussed in Chapter 3, we chose to utilize the voice coil actuator of an old hard disk drive for our Z-axis movement. Now we need to understand the capability of this actuator by obtaining its torque constant, K_T.

With several algebraic steps, we can obtain the torque constant. First, let us look

at the actuator, illustrated in Figure 4-11, more closely and then define necessary parameters for the calculations.

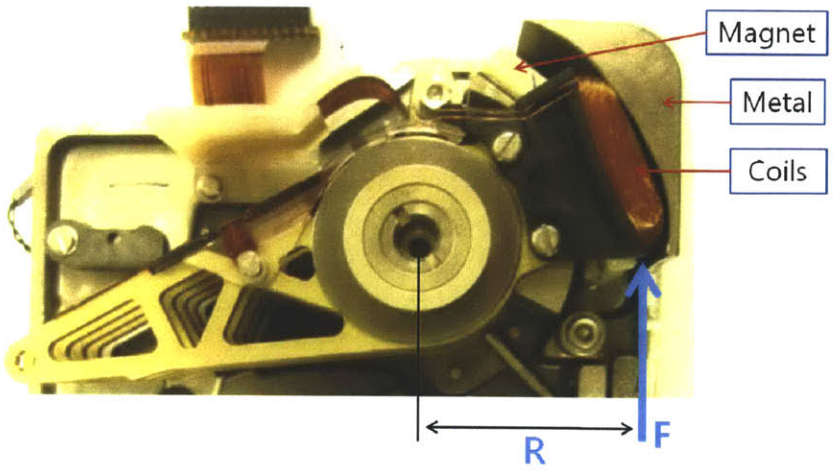

Figure 4-11: Actuation part of the old hard disk drive selected in the previous chapter.

As shown in the figure, coils are wound around a plastic adapter connected to the actuator arm and are located between a metal plate and magnet. Depending on the direction of the current through the coil, the arm experiences a Lorentz force that makes the actuator rotate either clockwise or counter-clockwise. The Lorentz force is expressed, by definition, as

$$F = 2Nl\vec{I} \times \vec{B} \tag{4.1}$$

where,

$$\begin{cases} \text{N=216} & : \text{Number of turns of coil} \\ \text{l=0.035} & : \text{Length of the coil (m)} \\ \text{I} & : \text{Current through the coil (Ampere)} \\ \text{B=0.65} & : \text{Estimated magnetic flux density (Tesla).} \end{cases}$$

The 2N term in Equation 4.1 comes from the fact that each coil turn passes through the air gap twice. The parameter l indicates the length of the coils in the magnetic field, and the outer product becomes a simple multiplication since the direction of the current is perpendicular to that of the magnetic field. As for the magnetic flux density, we assume that the magnet is a neodymium magnet which is commonly used in hard disk drives and the air gap is as wide as the magnet. Since a neodymium magnet has the remanence of about 1.3 tesla, the magnetic flux density is assumed to be about 0.65 tesla. When we measured the flux density with a gaussmeter, we obtained about 0.4 tesla which is in agreement with our estimated value.

Considering the relationship between torque and current together with Equation 4.1, we have

$$\tau = K_T I = FR = 2NlIBR \tag{4.2}$$

where R=0.04 m.

Therefore, the torque constant is derived as

$$K_T = \frac{FR}{I} = 2NlBR \simeq 0.4 \text{ Nm/A}. \tag{4.3}$$

As shown above, we know this actuator has a relatively small torque constant, and we also measure the internal resistance of the coils to be about 10 ohms. Accordingly, when considering overheating of the coils, the actual torque we can have with this actuator is thermally limited to less than about 1 Nm. As a result, it is very important to counter-balance the actuator arm in order to be able to easily manipulate it with small torques. This is why we design, in Chapter 3, the counter-balance mass with a brass block whose density (0.0085 g/mm^3) is higher than aluminum (0.0027 g/mm^3) with which the arm extension is designed to be built. Figure 4-12 below shows the CAD model and actual physical configuration of the Z-axis mechanism.

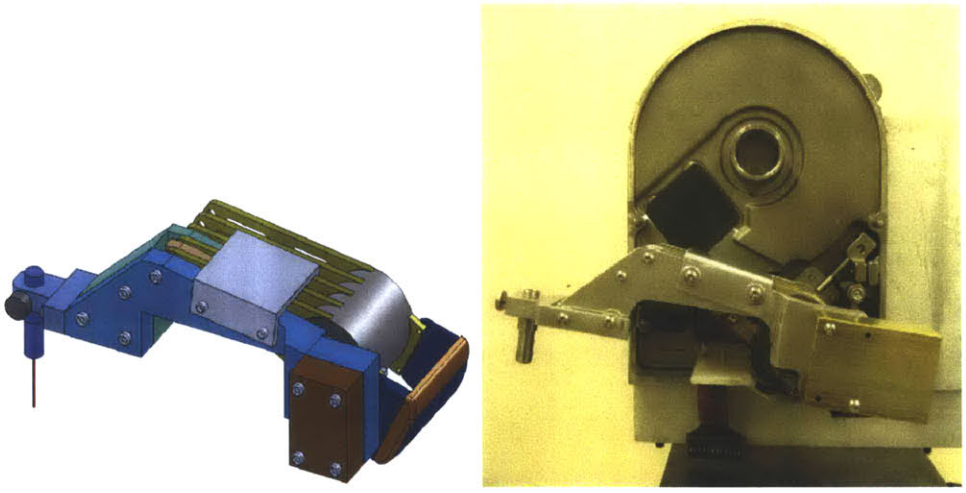

(a) CAD model (b) Physical system

Figure 4-12: Rotational z-axis mechanism with VCA and extended arm.

As shown in Figure 4-12(b), the brass counter-balance mass, a brown block in both figures, makes the whole arm balance at some middle point between two hard stops.

4.3.2 Optical Encoder

As discussed in Chapter 3, we need a sensor for the position control of the Z-axis movement. Given that the PDMS microwells and cells are on the order of 10 μm, it is required for the Z-axis motion to have the resolution of 1 micron or better. This, together with the arm length of 0.2 m, requires the rotational resolution of 5.0 μrad on the actuator shaft. To meet this condition, a MicroE optical encoder, Mercury 3500, is selected. This model guarantees the interpolated resolution of 3.0 μrad per count with the interpolation level of 256. The output of this encoder is a typical A-quad-B type with a maximum rate of 28.8 million quadrature states per second.

After finding a proper encoder system, it is critical to figure out how to implement it on the actuator since improper implementation of a sensor may cause serious error and poor measurement. For the first step, it is important to find the appropriate mounting area for a sensor, and Figure 4-13 shows our chosen location for the optical

encoder.

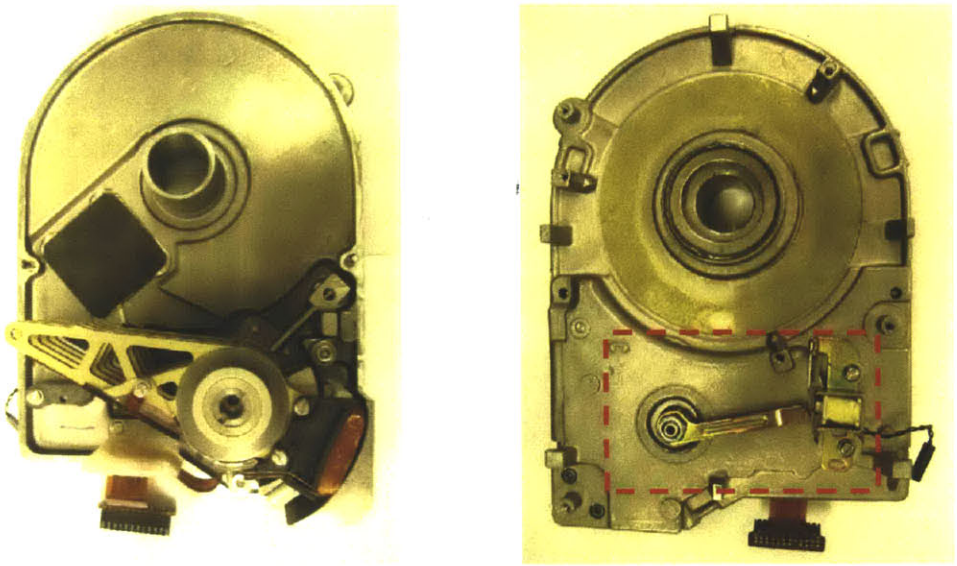

(a) Front view (b) Rear view

Figure 4-13: Selected mechatronics system for the z-axis motion.

Fortunately, as shown in the figure, the shaft of the actuator has a protruding part with the thread of M6×1.0. This part is indicated with a red dashed-line circle in Figure 4-14 for closer look. We decided to use this threaded part of the shaft as a mounting point for our encoder.

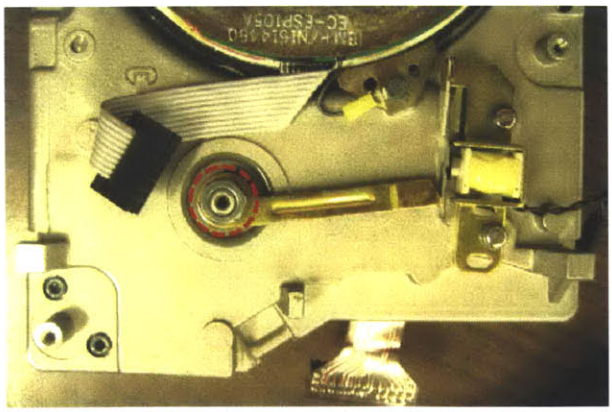

Figure 4-14: Mounting position for an optical encoder.

One more good thing is that MicroE offers standard hubs for each of the corresponding glass grating disks and they send the grating mounted on the standard hub on customers' demand. Accordingly, what we need to do is to design an additional mounting hub to connect the grating to the threaded shaft part of our system. Figure 4-15 shows these parts aligned for assembly. In the figure, the transparent disk is the glass grating with grating patterns indicated as a black line around the disk. The grating is mounted on the green hub which is the standard hub which MicroE offers. The pink structure is our designed mounting hub with three M3×1.0 threaded holes and one M6×1.0 threaded hole at the center. The complete drawing is provided in Appendix C.

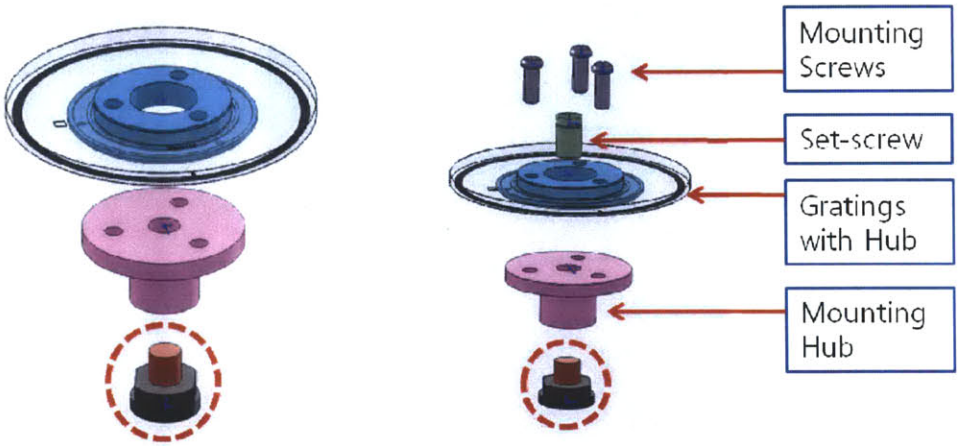

(a) Alignment (b) Assembly

Figure 4-15: Implementing an optical encoder on the selected mounting area.

As shown in Figure 4-15(b), the grating with the standard hub is to be mounted on the mounting hub with three mounting screws, and then the whole assembled part is mounted on the threaded part of the shaft indicated inside of the red dashed-line circle in the figure. Then a set-screw is threaded into the M6 thread of the mounting hub until it bears on the M6 screw of the rotary axis.

For the first step of the assembly, it is very important to correctly align the grating and the mounting hub. Poor alignment would result in large error and unreliable

measurements, making the whole closed-loop system less accurate. In order to optimize the alignment, we use an optical method which utilizes a camera or microscope to directly see the grating patterns and adjust the position of the grating. Figure 4-16 illustrates our settings for the alignment.

(a) Alignment setting (b) Magnified view

Figure 4-16: Alignment setting for the grating and the mounting hub and a magnified view of the grating patterns.

In this alignment setting, we mount the assembled part on a flat and transparent acrylic plate and this plate is placed on our self-designed inverse microscope discussed in Chapter 3. In this method, we just used a M6 screw to provide the rotary motion since we will only use less than 20° of the gratings; however, we suggest using a rotary bearing for more accurate alignment in case of using more range. The microscope then provides the real-time images of the grating patterns as shown in Figure 4-16(b). The straight red line indicates the outer edge of the grating patterns and is the reference position to which we calibrate the position of the grating. While rotating the glass grating, we observe the magnified view of the patterns and give little taps to the grating making sure that the outer edge of the patterns always stays along the red line during the whole 360° revolution. Once confirming that there is no shift on the patterns, the alignment is finished with fastening the three mounting screws. After this alignment, the grating is ready to be mounted on the shaft, and Figure 4-17

shows the CAD simulations for the encoder mounting.

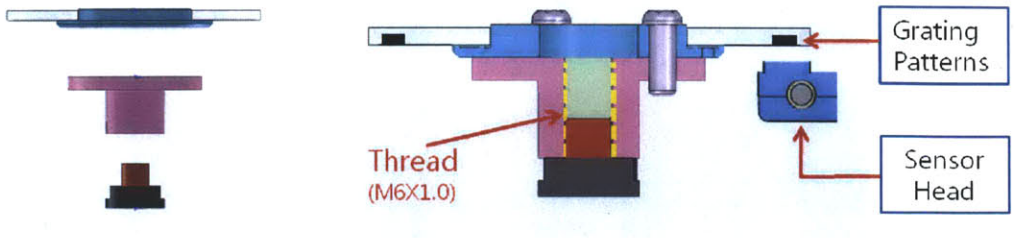

(a) Before assembly (b) After assembly

Figure 4-17: CAD assembly simulation for the encoder implementation.

Once the grating is ready for mounting, it is now time for the sensor head to be correctly implemented. As shown in Figure 4-17(b), the encoder head should be located below the grating patterns with a certain standoff distance. The standoff clearance for the MicroE encoder is 2.4 mm with a standoff tolerance of ± 0.15 mm. With this standoff clearance requirement, it is also important that the head is not tilted about any of the three axes in the three dimensional space. The information on the specific values for these alignment tolerances is provided in Appendix B. With all these requirements considered, the encoder head is mounted on a mounting plate and this plate is attached with epoxy onto the mounting area, which is the rear side of the hard disk drive. It is notable that shims are very useful to meet such a small standoff clearance.

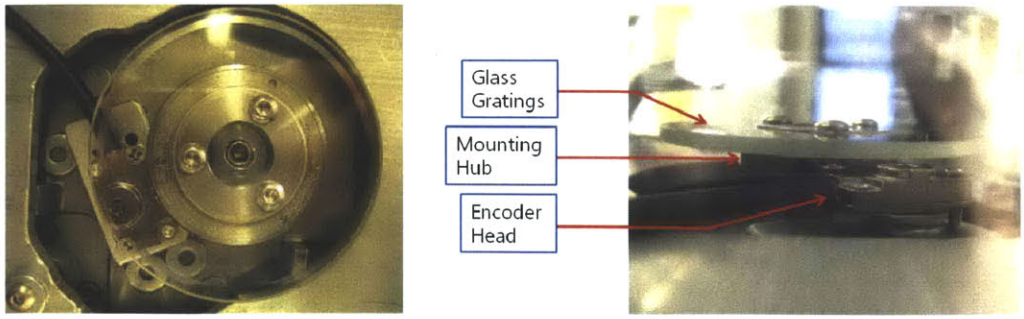

(a) Top veiw (b) Side view

Figure 4-18: Physical system with the encoder, gratings, and head implemented.

The LED indicators on the interpolator show the strength of the signal with red, yellow, and green colors, and these indicators are also useful to diagnose the alignment during the mounting process. Figure 4-18 shows the pictures of the implemented encoder system. After finishing the encoder implementation, we set up a dust cover around the area so as to avoid any interference of dusts with measurements. After the whole process of alignment and implementation, we could obtain the A-quad-B output well, but there was a problem with the index pulse. The LED indicators on the interpolator also have a dedicated LED for the index mark so that it blinks when the index passes over the encoder head, and we could see this LED blinking when we rotate the gratings to have the index mark pass the head. It is strange, however, we were not able to see the actual index pulse at the output channel. We suspect that this issue comes from the output calibration procedure. In the MicroE installation manual, it says that we need to be able to move the scale past the sensor in both direction so that the index mark passes under the sensor, and the index mark should be 7mm away from the sensor each direction. However, since our Z-axis actuator has the hard stops, we might not rotate the gratings enough to make sure that the index mark is well away from the sensor, and we assume this might cause the issue with the index pulse.

4.4 Self-designed Microscope

4.4.1 Self-designed Inverse Microscope

In Chapter 3, we discuss the design of the inverse microscope with necessary components such as a charge-coupled device (CCD) camera, a zoom lens, and a XY microscope stage. In this section, we explain how we construct the self-designed microscope and show the physical configurations of it.

The compact and cost-efficient inverse microscope is built on the side of a granite table. On this platform, a L-shaped bracket is used as the frame of the microscope. Since this bracket has an opening, a camera and zoom lens can capture images through

this opening. The camera has an analog output which is connected to the NI vision card in the NI PXI controller. This real-time controller receives data from the camera and shows the monochrome images to users. The quality of images can be improved by adding proper filters in the controller. A manual focus stage is also added in order for users to adjust the working distance for clear images. Finally, an XY microscope stage is implemented on the L-bracket such that the bracket opening is aligned with the location where PDMS microwells are placed. Figure 4-19 shows the physical configurations of the self-built microscope with a XY stage on it.

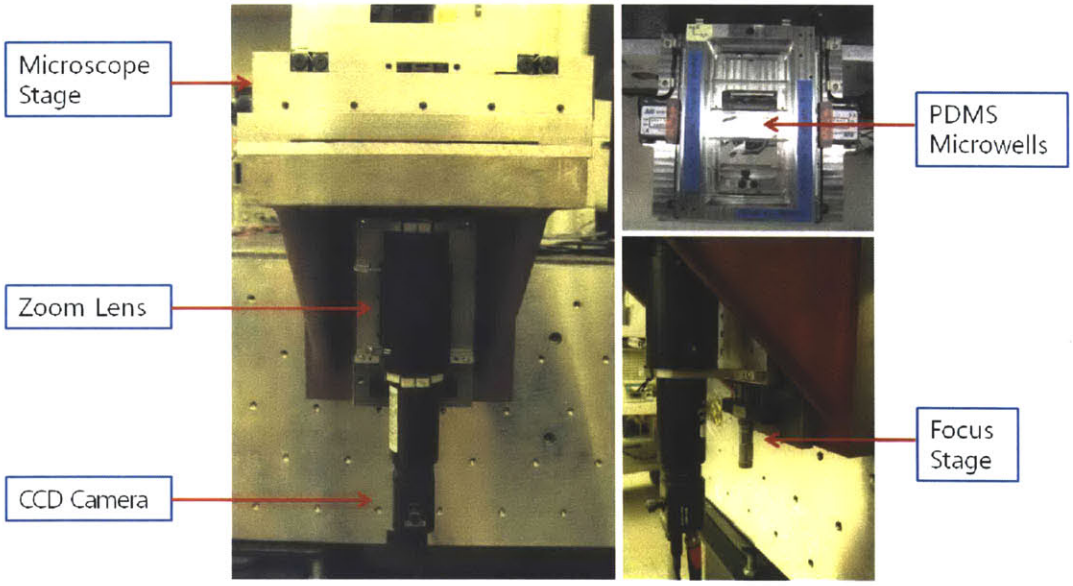

Figure 4-19: Self-constructed inverse microscope on a granite table.

As shown in the figure, this microscope is built as designed in Figure 3-13. We obtain an image of PDMS microwells with this inverse microscope as illustrated in Figure 4-20.

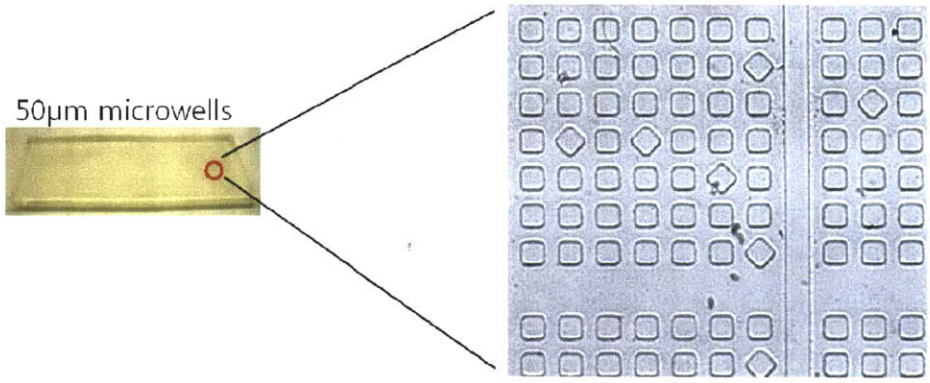

Figure 4-20: Testing of the self-constructed microscope.

The image shows many microwells and each microwell has 50 μm edges and depth of the same size. The magnification level can be changed by users up to ten times, and the image shown is obtained with the threefold setting.

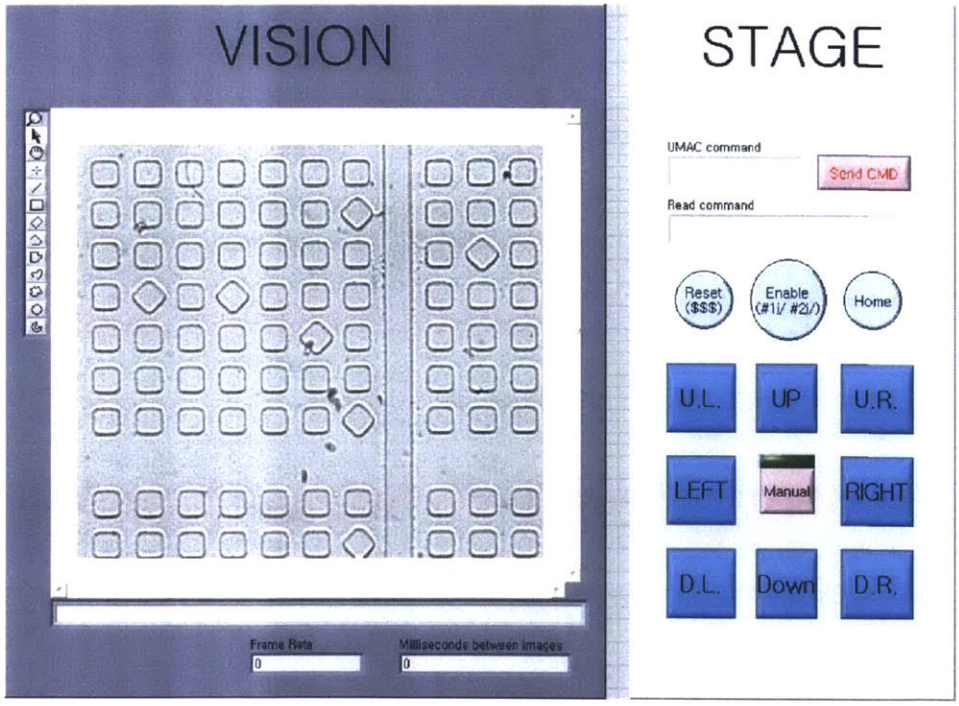

Figure 4-21: User interface with Labview for the microscope system.

A user interface (UI), shown in Figure 4-21, is also created for easier and more

intuitive interaction between users and devices. The stage control panel controls the stage movements and the vision panel shows the real-time images of microwells as the stage moves around. The detailed Labview coding is provided in Appendix A together with the syringe control panel code discussed in the previous section.

4.4.2 Microscope Stage with Piezo-actuator

The microscope stage used in our microscope system is equipped with piezoelectric motors from Nanomotion. The mechanism of these motors are interesting in that it creates actuation by piezoceramics' walking-like motion. When a piezocermic material is electrically excited, it converts the electrical power to mechanical strain. Under special electrical field, both the longitudinal extension mode and the transverse bending mode are excited simultaneously, creating an elliptical trajectory of the piezoceramic material. With the proper placement of a ceramic plate against the edge of the piezoceramics, the trajectory motion of the material can provide thrust to the plate, thereby moving the ceramic plate [21]. This trajectory motion looks just as it walks on the plate. The two steps of this mechanism are illustrated in Figure 4-22 below.

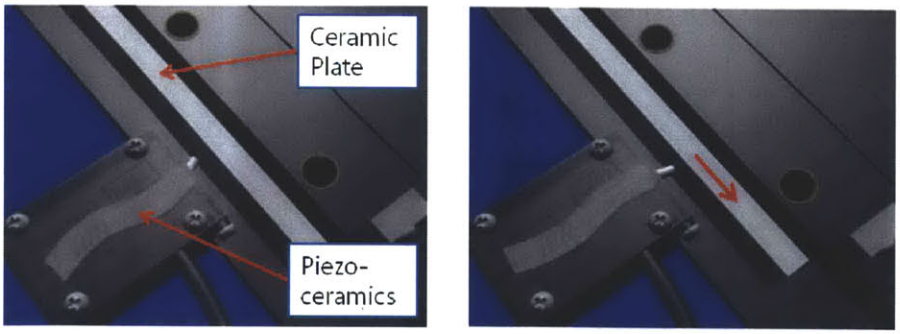

(a) Walking motion #1 (b) Walking motion #2

Figure 4-22: Piezoceramic actuator in the microscope stage. (Figures taken from [21].)

The microscope stage we use for our prototype has two stacked axes to provide

the XY plane motion. The top axis has two of these piezo-actuators to drive the Y-axis motion and the bottom axis has one piezo-actuator driving the X-axis motion. This microscope stage were donated to us by Helicos Company, so we cannot tell what the original reason for the different number of actuators. However, the fact that the top axis has less mass than the bottom axis together with top one uses two actuators, we assume that the top axis was designed to be the fast axis by more force and more acceleration with two actuators. In addition, both axes have linear encoders implemented to provide the position feedback to the controller called Universal Motion and Automation Controller (UMAC) which we explore in Chapter 5 together with the control algorithm for this stage.

Chapter 5

System Integration and Control Design

This chapter discusses how the system is integrated with the components detailed in the previous chapters, and also describes how the control architecture is implemented for the system to achieve the desired tasks. The controller design for the picking mechanism, which is one of the most critical parts of the prototyped system, is discussed in detail. In the process of designing the controller, interesting phenomena associated with the system are also discussed.

5.1 System Integration

The main task for the prototype of the robotic single-cell manipulator is to pick up a single cell or a microbead of equivalent size, generally 10μm diameter, from each individual microwell. For this purpose, components detailed in the previous chapters are integrated: a voice coil actuator, optical encoder, CCD camera, zoom lens, real-time controller, and vision interface. All the parts are composed such that the integrated system has National Instruments (NI) real-time PXI chassis as a main controller. The overall scheme for the total system is shown in Figure 5-1 below.

5.1.1 Scheme for the Prototype

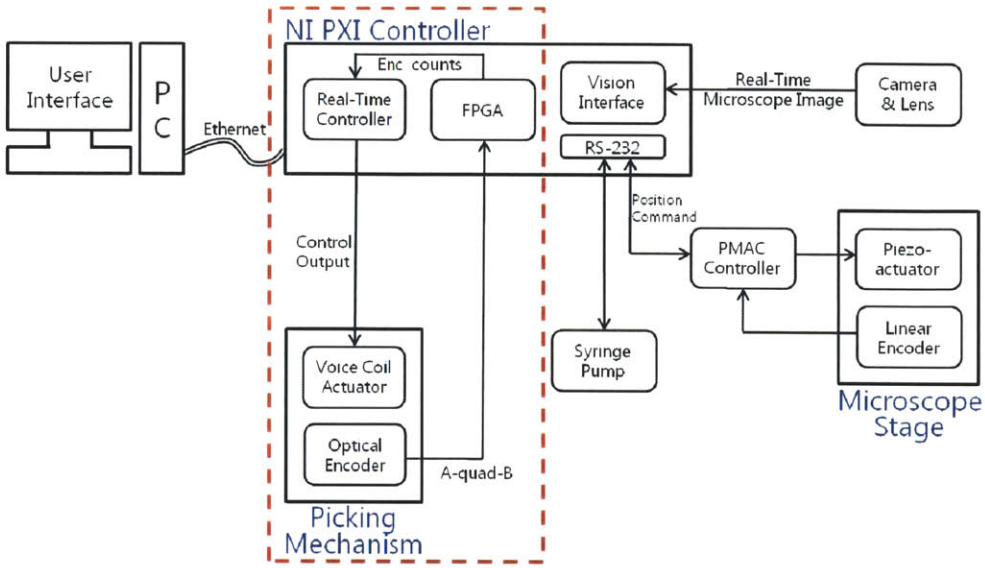

Figure 5-1: System schematic for the prototype of the robotic single-cell manipulator.

Tasks performed by each component are discussed in detail in the following sections; however, here is a brief description of how it works. Firstly, real-time microscope images of the PDMS microwells are transferred though the vision interface installed in the NI PXI Chassis, and those images are used to locate an individual cell or target of interest among a myriad number of microwells. For the prototype system, the XY microscope stage is used to move the PDMS microwells so as to align the well of interest with the expected location of the end-effector. This effector is a glass micropipette driven fluidically by a syringe pump. Commands for the microscope stage to move are given from the main controller to the Universal Motion and Automation Controller (UMAC) through a serial communication. This UMAC controller, contains a Programmable Multi Axis Controller (PMAC) CPU for stand-alone operation, takes the encoder position data and provides control output to the XY stage piezo-actuators discussed in the previous section. The controller design for the UMAC can be performed with a dedicated software package called PMAC Executive Pro2 Suite, and we

explore this topic in the following section. After locating the target, the glass pipette mounted at the end of z-axis actuator arm is lowered so that the tip touches the rim of the target well. To precisely control the tip position, an optical encoder is used as the actuator arm position sensor. A Field Programmable Gate Array (FPGA) is programmed to count the edges of the encoder A-quad-B output. Controlled by the main controller through serial communication, the proper amount of liquid is then aspirated by the syringe pump in order to pick the target cell or microbead out of the microwell. All of this process is shown through the user interface window for operators to observe. Figure 4-1 from the chapter 4 shows the corresponding physical configurations of the prototype.

5.2 PID Control for the XY Stage

In this section, we briefly discuss how we control the microscope XY stage with the UMAC controller. In following section, we explore the main control issue with the Z-axis arm system. As discussed in the previous section, the microscope XY stage is controlled by the UMAC and we can design a control scheme and change control parameters by using the software package PMAC Executive Pro2 Suite. The linear encoder, MS 30 Series by RSF Elektronik, implemented on the XY stage provides a resolution of 0.16 μm together with an interpolator ($\times$4096) included in the UMAC controller. The PMAC CPU in the UMAC controller can be connected to a user PC through a serial port, ethernet, or USB. This connection allows a user to design a controller and change control parameters with the software tool shown in Figure 5-2. As shown in Figure 5-2(a), the software provides a convenient auto-tuning tool with which we can set some desired specifications such as a damping ratio and choice of integral action and automatically obtain calculated control parameters. For our application, we decide to use a simple PID controller together with a low pass filter, and the transfer function for this controller is

$$C(s) = K_P + \frac{K_I}{s} + K_D s + \text{Low Pass} = \frac{K_D s^2 + K_P s + K_I}{s(\tau s + 1)}. \qquad (5.1)$$

The low pass filter is used to give additional pole and prevent the high frequency roll-up. After the auto-tuning process, we can implement the tuned gains on the system to check time responses such as step response, ramp response, or a user-defined trajectory following with the interactive tuning tool shown in Figure 5-2(b).

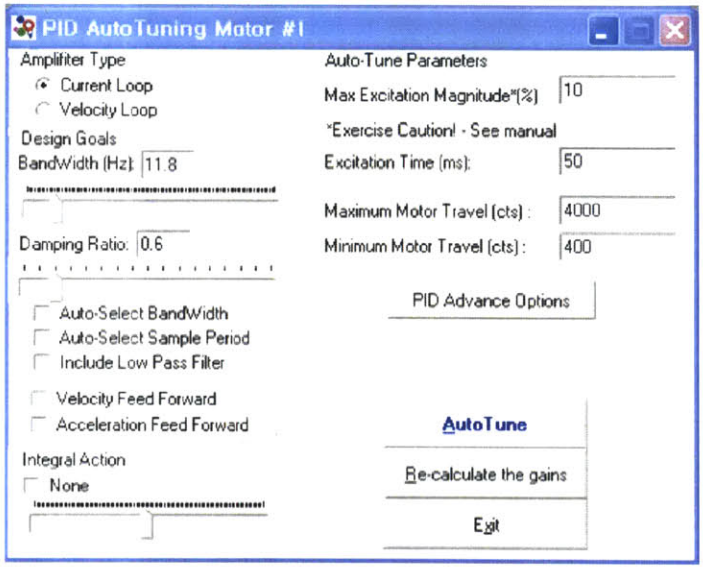

(a) Auto-tuning tool

(b) Interactive tuning tool

Figure 5-2: The software package, PMAC Pro2, for the UMAC controller.

For a start, we select the damping ratio of 1 to avoid the overshoot and choose to include the integral action to eliminate the steady-state position error. After implementing the auto-calculated gains (K_P=20673, K_I=62239, K_D=5154), we obtain a step response to 1000 counts (160 μm) input with the interactive tool as illustrated in Figure 5-3.

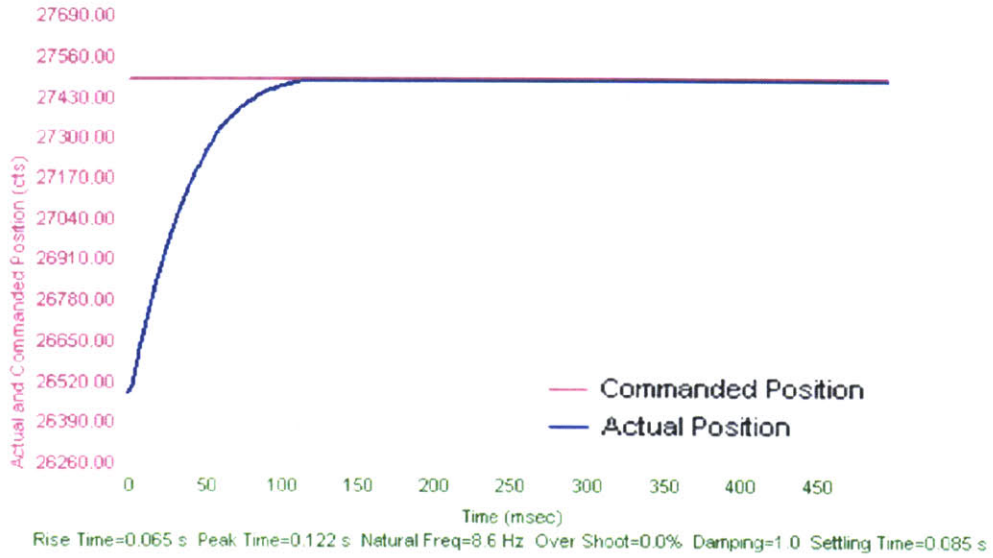

Figure 5-3: Step response of the stage with the auto-tuned gains.

As shown in the figure, the response yields no overshoot, as expected, and has a rise time of 0.062 s, and a settling time of 0.085 s. This could be an acceptable response; however, we can fine-tune the gains for better response. Without going through the auto-tuning again, we directly use the interactive tool to change the gains and check the corresponding responses. In order to decrease the rise time for faster initial response, we increase the proportional gain and the integral gain and reselect the derivative gain accordingly for faster settling time. On the basis of this empirical tuning, we choose such gains as

$$\begin{cases} K_P &= 30000 \\ K_I &= 80000 \\ K_D &= 3000. \end{cases}$$

Figure 5-4 below now shows the step response of the stage to 1000 counts input with the fine-tuned gains.

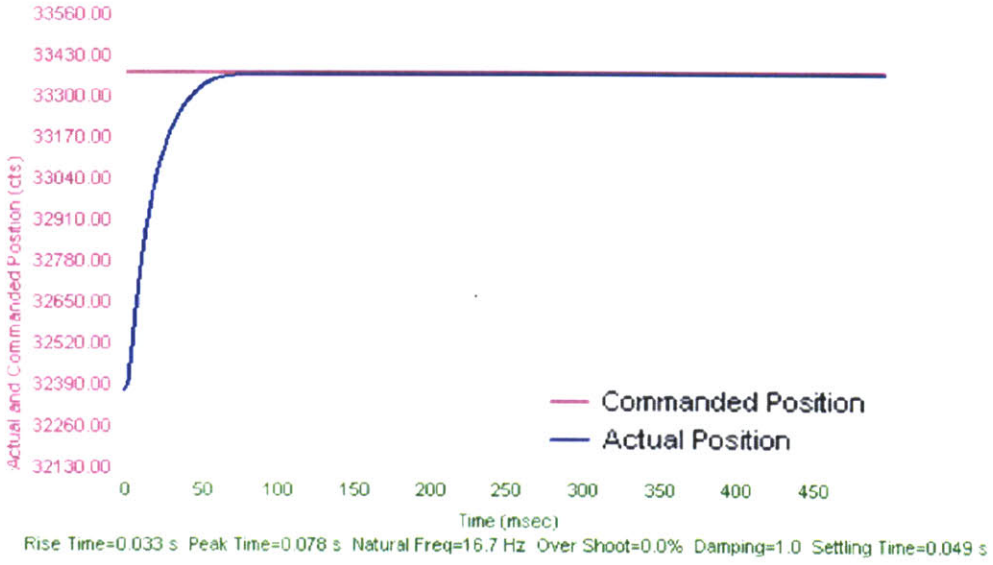

Figure 5-4: Step response of the stage with the fine-tuned gains.

From the figure, we see that the rise time decreased to 0.033 s and the settling time to 0.049 s, making the system almost twice faster than before. It is also possible to even lower the rise time for applications with faster initial response required. In fact, we can achieve such a result by significantly increasing the proportional and integral gains. Yet, such a fast rise time can easily yield large overshoot and slow settling, so we need to choose the proper derivative gain accordingly. These effects of the gains are true in general; however, it is always necessary to fine-tune the gains after setting up the starting point. Taking the same process we took above with the

software tools, we chose the control parameters for the faster initial response with smaller rise time as

$$\begin{cases} K_P &= 95000 \\ K_I &= 190000 \\ K_D &= 800. \end{cases}$$

Now as expected we can see the step response with faster rise time in Figure 5-5 below.

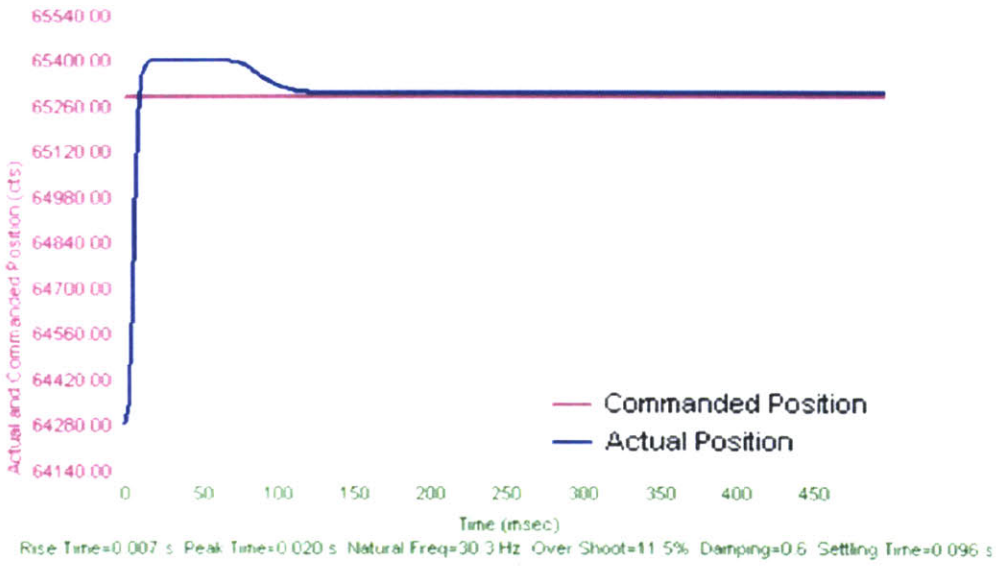

Figure 5-5: Step response of the stage with the reselected gains for faster rise time.

The figure shows that the rise time decreased to 0.007 s. However, the system now has the overshoot of 11.5 % due to the large proportional gain. Also, even though we tried to lower the settling time at the same time by decreasing the derivative gain, the settling time could not be lower more with other characteristics intact because of the large integral gain. Accordingly, these control parameters are effective with applications where faster initial response is relatively more needed than the settling

time and a little bit of overshoot is allowed. However, for our application where a faster settling time is more necessary and a smooth motion is preferred, we choose the parameters implemented on Figure 5-4, i.e., K_P=30000, K_I=80000, and K_D=3000.

5.3 Control Loop for the Z-axis Motion

The main control target of the prototype system is the z-axis position. The voice coil actuator discussed in the previous chapter is used for the z-axis motion, and the optical encoder is used as a sensor to provide the position feedback. This control loop is indicated inside of the red dashed-line box in Figure 5-1 above, and it is again illustrated in a bit more detail in Figure 5-6.

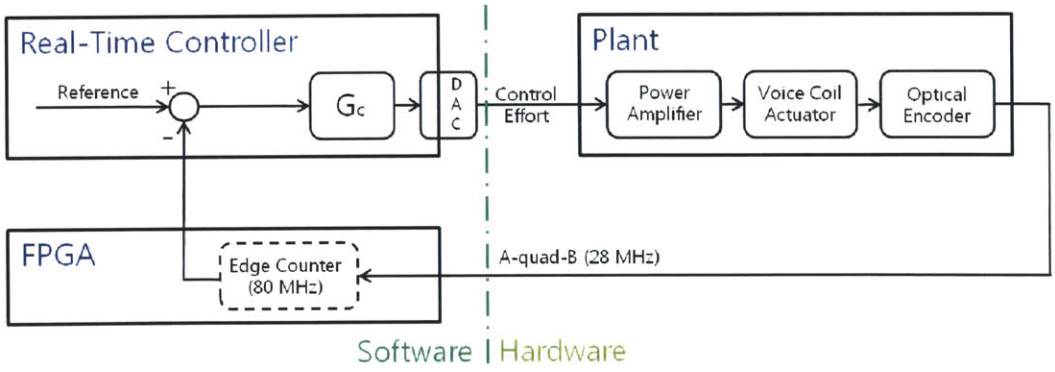

Figure 5-6: Control loop for Z-axis picking motion.

As shown in the figure, the edge counter in the FPGA uses a 80 MHz clock, which is well beyond the maximum speed of the encoder output, 28 MHz, to make sure not to loose any edges of the encoder output signal. The power amplifier, with a gain of 4, is built with an APEX PA04 used in voltage-control mode. Specifications of this amplifier are provided in Appendix B in more detail.

5.3.1 Frequency Response of the Plant

In order to decide a control approach, we need to first understand the plant which, for this system, includes a power amplifier, a voice coil motor, and an encoder. This can be done by mathematically modeling each component and superposing them. However, for some cases where it is hard to measure necessary parameters such as mass, stiffness, and damping, it is easier to measure a frequency response of the plant as a whole. Under the assumption the plant is linear time-invariant, any periodic input with a certain frequency ω going through the plant results in a periodic output with the same frequency, but different amplitude and phase. Plotting the ratio of amplitudes and the phase difference between the input and output gives the frequency response or Bode plot, and this is what a digital signal analyzer (DSA) does. Figure 5-7 below illustrates the setup of the Z-axis mechanism part for frequency response measurement.

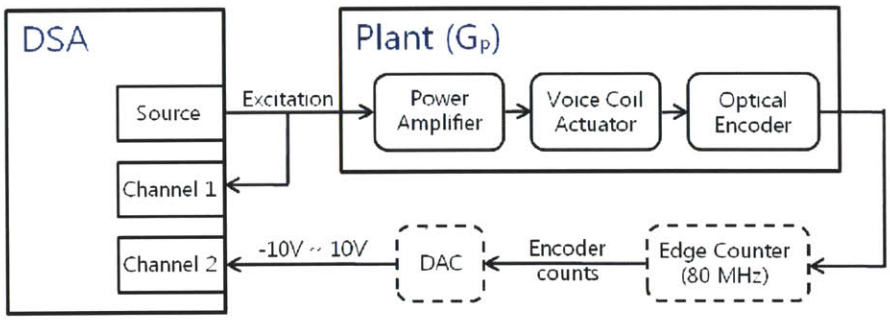

Figure 5-7: Setup for the frequency response measurement of the plant.

A DSA device in sinusoidal mode utilizes a sine wave as a periodic input in order to excite the plant, and then the output, also as the same frequency sine wave with different amplitude and phase, goes back into the DSA device. The equation for this is

$$A \sin \omega t \quad \rightarrow \quad A\,|G_p(j\omega)| \sin(\omega t + \angle G_p(j\omega)). \tag{5.2}$$

The frequency response of the plant is then given as plots of the magnitude,

$|G_p(j\omega)|$, and the phase, $\angle G_p(j\omega)$, in terms of ω, as indicated in Figure 5-8 below. From the figure, we can tell that this plant is a second order system having its break frequency at around 1 Hz. Also, we can see two interesting phenomena from the frequency response; one is the low-frequency plateau in the magnitude plot and the other is the resonance behavior at around 200 Hz. These phenomena are discussed in detail in the following sections. We also obtain a mathematical model of the plant from the frequency response by fitting later in the following section.

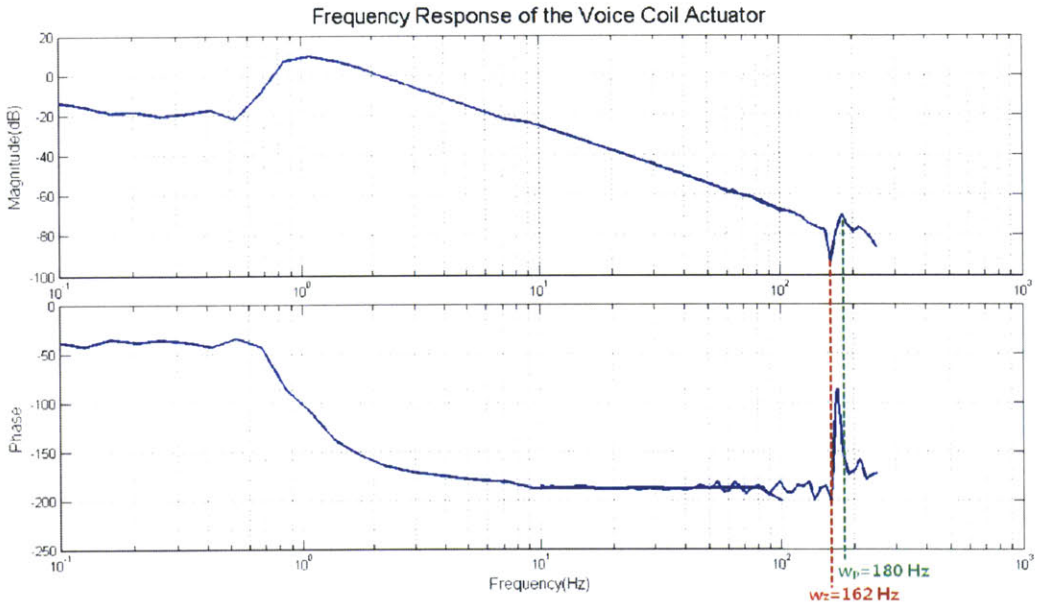

Figure 5-8: Measured frequency response of the plant.

5.3.2 Mass Disconnection

The phenomenon observed at around 200 Hz in Figure 5-8 is often seen when a system has flexure bodies or flexible connections. For such a system, it can be simply considered as two masses connected with a spring and dashpot.

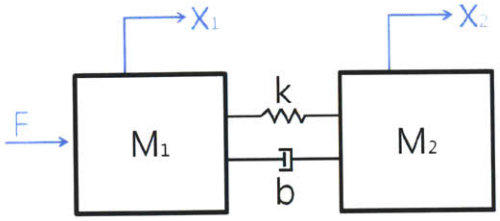

Figure 5-9: Flexure body depicted as two masses connected with a spring and damper.

From the Figure 5-9, we see that the first mass is collocated since the force is directly applied to it while the second mass is not. This two-mass model has the equations of motion of

$$M_1\ddot{X}_1 = b(\dot{X}_2 - \dot{X}_1) + k(X_2 - X_1) + F \tag{5.3}$$

$$M_2\ddot{X}_2 = b(\dot{X}_1 - \dot{X}_2) + k(X_1 - X_2). \tag{5.4}$$

These equations have the state variable form of

$$\begin{bmatrix} \dot{X}_1 \\ \ddot{X}_1 \\ \dot{X}_2 \\ \ddot{X}_2 \end{bmatrix} = \begin{bmatrix} 0 & 1 & 0 & 0 \\ -\frac{k}{M_1} & -\frac{b}{M_1} & \frac{k}{M_1} & \frac{b}{M_1} \\ 0 & 0 & 0 & 1 \\ \frac{k}{M_2} & \frac{b}{M_2} & -\frac{k}{M_2} & -\frac{b}{M_2} \end{bmatrix} \begin{bmatrix} X_1 \\ \dot{X}_1 \\ X_2 \\ \dot{X}_2 \end{bmatrix} + \begin{bmatrix} 0 \\ \frac{1}{M_1} \\ 0 \\ 0 \end{bmatrix} F \tag{5.5}$$

$$\vec{y} = \begin{bmatrix} 1 & 0 & 0 & 0 \\ 0 & 0 & 1 & 0 \end{bmatrix} \begin{bmatrix} X_1 \\ \dot{X}_1 \\ X_2 \\ \dot{X}_2 \end{bmatrix}.$$

The pole-zero maps of both transfer functions for the mass 1 and mass 2 appear as in Figure 5-10. In addition, For the specific values of $M_1 = 9$ kg, $M_2 = 1$ kg, $k = 10^7$ N/m, $b = 30$ Nsec/m, Bode diagrams for each transfer function, $\frac{X_1}{F}$ and $\frac{X_2}{F}$, are plotted in Figure 5-11.

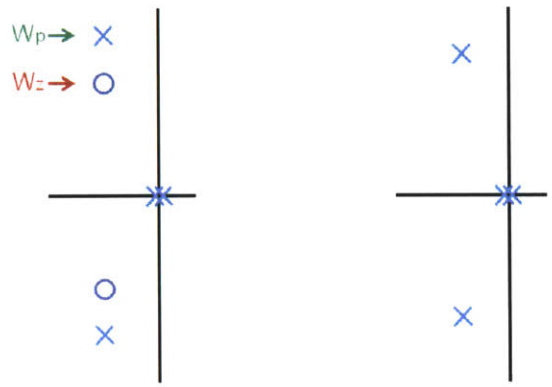

(a) X_1/F (b) X_2/F

Figure 5-10: Simplified pole-zero maps of the collocated and non-collocated system.

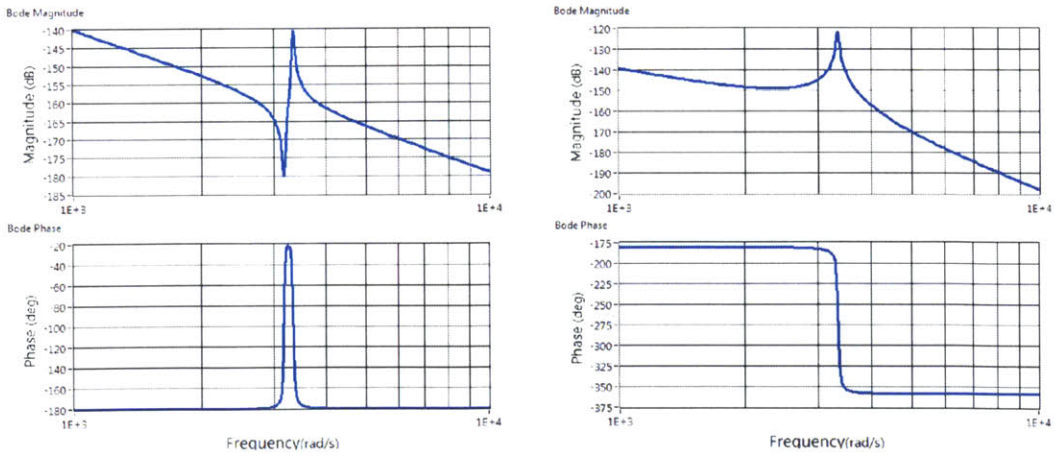

(a) X_1/F (b) X_2/F

Figure 5-11: Bode plots of two-mass model.

Considering this model, we can associate the mode at about 180 Hz in Figure 5-8

with the collocated case. In this case, ω_z=162 Hz and ω_p=180 Hz as indicated in the Figure 5-8. When this plant is driven at frequencies higher than ω_p, it behaves as if the mass has been reduced from M_1+M_2 to M_1 and this effect is the same as disconnecting the second mass. This is why this phenomenon is called *mass disconnection*. In general, these ω_z and ω_p are expressed in terms of the masses and the stiffness.

$$\omega_z = \sqrt{\frac{k}{M_2}}, \qquad \omega_p = \sqrt{\frac{k}{M_{eq}}} \ (\text{where}, M_{eq} = \frac{M_1 M_2}{M_1 + M_2}). \tag{5.6}$$

The collocated mass is the actuator arm, connected encoder, and its extension base. We need a bit more understanding in order to find the non-collocated mass of the plant. Using the phenomenon called *mass tuned damper* is of great help. Mass tuned damper is very interesting phenomenon because when driven at the natural frequency of the zero, the collocated mass does not move at all even with the direct excitation and only the non-collocated mass moves even without any direct force on it. This occurs when a flexure system is excited by the frequency of ω_z. When the plant was excited by a periodic input of ω_z=162 Hz, the arm and extension base was stationary and some buzzes were observed from the pipette holder. Accordingly, we can tell that the pipette holder is the non-collocated mass of the plant with respect to measurements taken at the encoder. Conversely, with respect to the pipette position, this mode is collocated.

5.3.3 Amplitude-dependent Frequency Response

Another interesting phenomenon that deserves a closer look in Figure 5-8 is the low-frequency plateau. Unlike a general second order system response where the magnitude plot begins with a DC gain and stays flat until it meets a break frequency, the measured frequency response has a strange bump at around the break frequency. It becomes more interesting when observing similar, but different behavior with another measurement, and it is illustrated in Figure 5-12. The blue line is the measured response with a sinusoidal input of relatively small amplitude, 0.3 V, and the red dashed line is when the amplitude is larger, 1 V or higher.

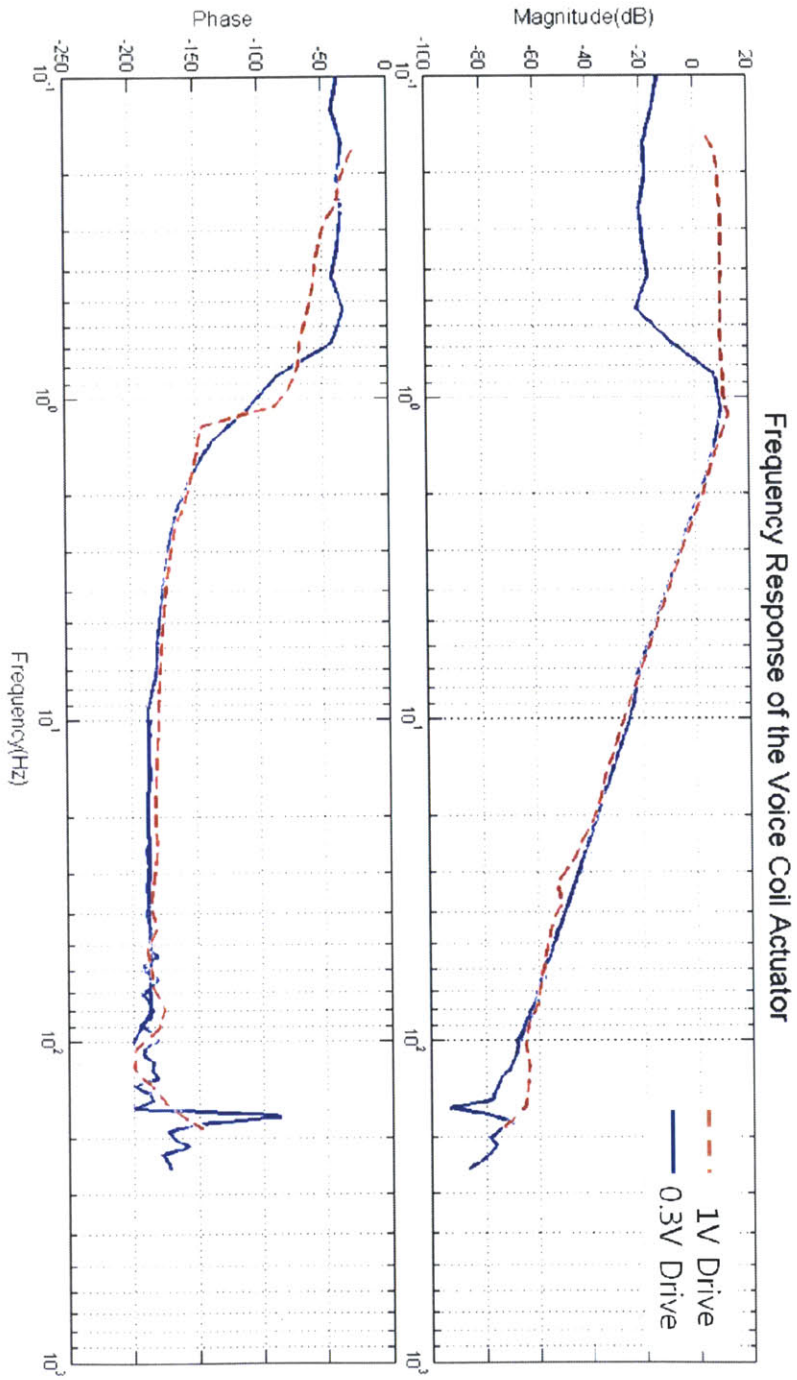

Figure 5-12: Amplitude-dependent frequency response of the arm system with bearing. Upper curve is with 1 V drive amplitude; lower curve is with 0.3 V drive amplitude.

As shown, with the input of a small amplitude, the frequency response of the plant has a strange bump and it also has a lower DC gain. When everything is perfectly linear, the frequency response has to be independent of the input amplitude. Thus, we know that this low-frequency behavior stems from some form of non-linearity. The most likely mechanism which can explain this is bearing friction.

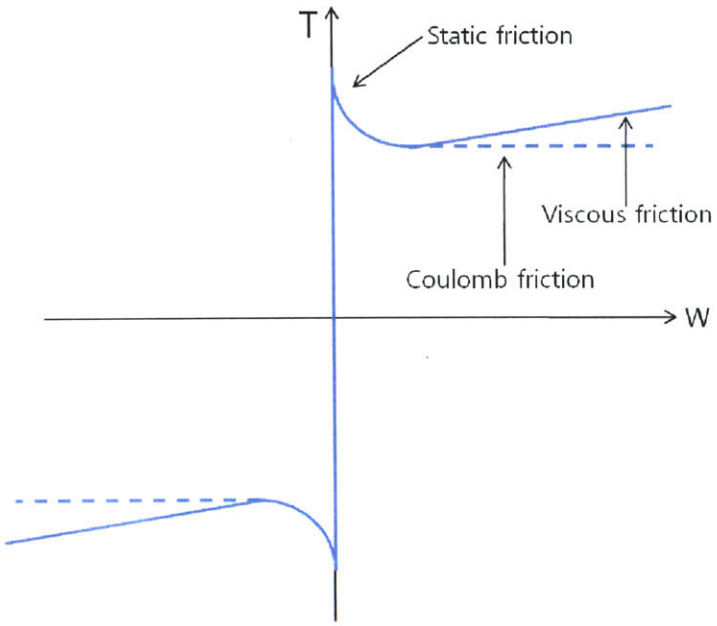

Figure 5-13: Friction torque versus relative velocity for large displacement [12].

When the input amplitude is higher than a certain threshold value, the angular displacement of the voice coil motor is relatively large and the bearing friction is then basically related to the angular velocity based on the Coulomb friction model, which is shown in Figure 5-13 with other general types of friction [10][12].

However, this model does not perfectly hold for the case when the displacement is microscopic, which is when the input amplitude is small. In that case, the bristle model [15] can be applied. Based on this friction model, asperities can be considered as flexible bristles and every contact point of two surfaces are viewed as a bond between these bristles. This concept is illustrated in Figure 5-14. As one surface moves relative

to the other, the bristles behave as springs, as shown in Figure 5-15 [13][17].

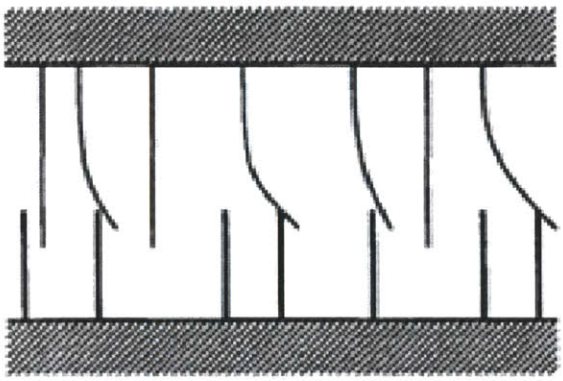

Figure 5-14: The friction interface between two surfaces is thought of as a contact between bristles. For simplicity the bristles on the lower part are shown as being rigid. (Illustration and captions taken from [14].)

As shown in Figure 5-15 and explained in [15], friction behaves likes a spring when the applied force is smaller than the break-away force and the stiffness of the spring is related to the amount of the displacement. From the figure, we know that the smaller the applied force and the presliding displacement are, the stiffer the spring behavior of the friction becomes. As a result, when we measure frequency responses of a system containing components like a bearing which can bring about this friction effect, we obtain different responses with different excitation amplitude. The basic concept of this phenomenon is illustrated in Figure 5-16 and this is consistent with what our measurement showed in Figure 5-12. Since this phenomenon comes from micro-level friction of two contacting surfaces, any systems with contacting parts such as bearings are expected to have this sort of phenomenon.

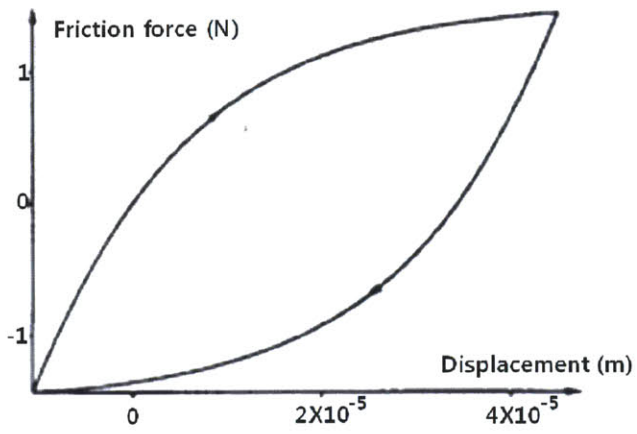

Figure 5-15: Bristle friction model for microscopic presliding displacement. (Illustration taken from [14].)

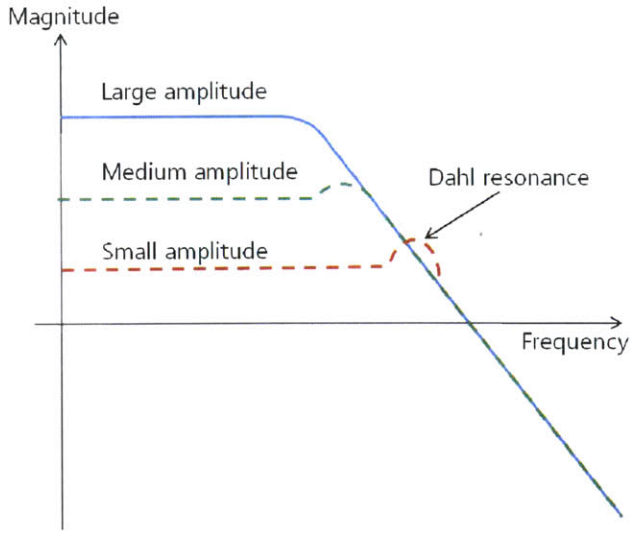

Figure 5-16: Conceptual sketch of an amplitude-dependent frequency response.

As shown in Figure 5-16, the frequency response with relatively small amplitudes shows an interesting phenomenon, called *Dahl resonance* after Philip R, Dahl who wrote an early report on this subject [10][11]. This phenomenon most likely comes from the spring-like behavior of presliding friction caused by contacting surfaces, and

the frequency is likely the resonant frequency of the presliding elastic behavior [16]. From our arm system illustrated in Figure 5-12, we can see that there is a significant resonance spike of about 25 dB and the break frequency of about 1 Hz is likely the resonant frequency of the spring-like behavior of the presliding friction caused by the bearing we have in our arm system.

5.3.4 System Modeling by Fitting

We have discussed two phenomena of the mass disconnection and amplitude-dependent frequency response in the previous sections. With large enough excitation, the bearing effect can be ignored and the DSA can obtain a frequency response of the plant as a standard second order system. Also, if we decide to work in lower frequency region than any resonance frequency areas, we can build a mathematical model for the plant by fitting the measured Bode plot of the plant, which is illustrated in Figure 5-17 below. In addition, if crossover is well above the Dahl resonance, closed loop stability is not affected by the Dahl resonance.

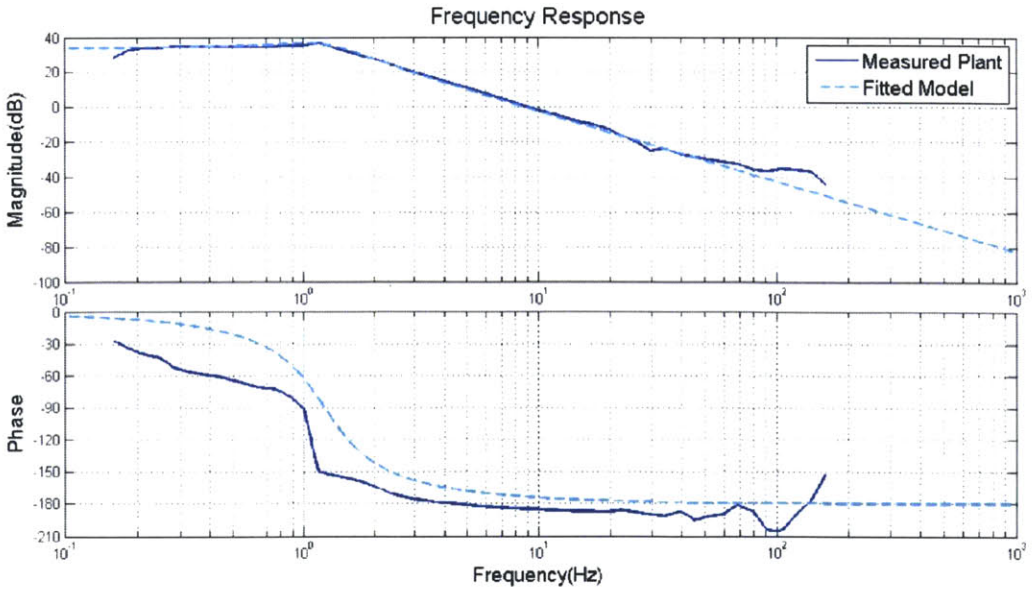

Figure 5-17: Bode plot of the fitted model for the plant.

The dashed blue line indicates the fitted mathematical model and its expression is

$$G_p(s) = \frac{K_m {\omega_n}^2}{s^2 + 2\zeta\omega_n s + {\omega_n}^2} = \frac{3002}{s^2 + 6.16s + 59.29}. \tag{5.7}$$

$$(\text{where } K_m = 50.64, \quad \omega_n = 7.7 \text{ rad/s}, \quad \zeta = 0.4)$$

The mathematically model fits reasonably well with the measured response up until 100 Hz. Since we omitted the high-frequency resonances for the model, it is very reasonable to see some discrepancy in higher frequencies. The measured Bode plot of the plant in Figure 5-17 does not contain the resonance behavior at high frequency because the range of measurement was limited by the slow loop time, 2 ms, and therefore much phase delay. At the time of measurement, we used Labview to measure the frequency response and the loop time was limited by the default real-time clock of 1 KHz. However, we later found out that a faster real-time clock of 1 MHz was available with a CPU better than Pentium 3 and used this faster clock to measure the frequency response again. Based on the later measurement, we knew that there is the resonance around 200 Hz just as shown in Figure 5-8.

5.4 Loop-shaping Controller Design

From the blue line which indicates the measured Bode plot of the plant in Figure 5-17, we know that this system would be not very stable when closing the loop with unity feedback and unity proportional gain since the return ratio has gain and phase margins close to zero. Accordingly, we need a controller to appropriately control the system and make it stable with large enough bandwidth, gain and phase margins for the application of interest. It can be surely done only mathematically to design a PID controller using the mathematical model we have derived in the previous section; however, it would be easier and more intuitive to use the loop-shaping method since we already have the frequency response of the loop transfer function of the system.

5.4.1 Lead Compensator

As explained above, the loop transfer function of the system needs additional phase at the crossover frequency to have enough damping, and higher loop gain to have larger bandwidth and therefore better stiffness. A lead compensator, indicated below, can be used for this purpose.

$$\begin{aligned} Lead(s) &= K\frac{\alpha\tau s+1}{\tau s+1} \qquad (where\ \alpha > 1) \\ &= \frac{0.03988s+1.585}{0.002516s+1} \end{aligned} \tag{5.8}$$

We here choose $\alpha = 10$ to add additional 55°, $\tau = 2.516 \times 10^{-3}$ sec and $K = 1.585$ to have the crossover frequency at ω_c=20 Hz. The crossover frequency can be increased by implementing larger gain K; however, it is here selected as 20 Hz to test if the mathematical control model fits well with the experimental plot. Figure 5-18 shows the experimentally measured frequency response of the loop transfer function overlayed with the Bode plot of the analytical model.

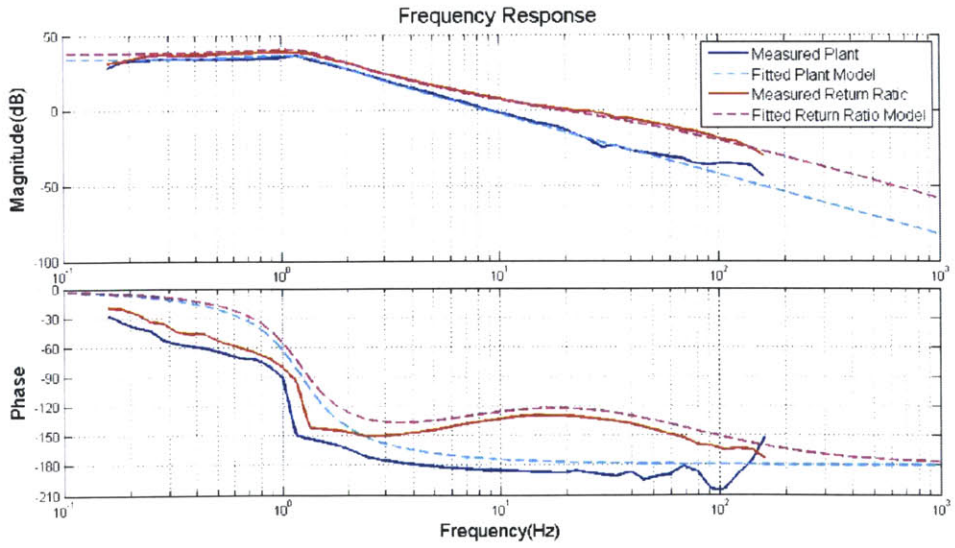

Figure 5-18: Bode plot of the experimental response and the analytical model with lead compensator at ω_c=20 Hz.

As shown in the figure, we can see that the mathematical model for the plant is very reliable in designing a controller. The magnitude plot fits well before the resonance region and the phase plot also fits reasonably well between 30 Hz and 100 Hz which is the area of primary interest.

This lead compensator is very similar to a PD controller in that they practically do the same job on a plant. One thing different between a lead compensator and a regular PD controller is that the former has an additional pole further left of the zero to avoid the infinite roll-up the latter has. In practice, this infinite roll-up amplifies high-frequency noise so that an additional pole is generally added, thereby making a lead and modified PD controller practically same. It can be also mathematically understood via:

$$\begin{aligned} \text{Lead}(s) &= K\frac{\alpha\tau s+1}{\tau s+1} \\ &= K(\frac{\tau s+1}{\tau s+1}+\frac{\alpha\tau s-\tau s}{\tau s+1}) \\ &= K(1+\frac{\tau(\alpha-1)s}{\tau s+1}) \\ &= K_P+K_D\frac{s}{\tau s+1} \end{aligned} \tag{5.9}$$

$$\text{where}\quad K_P=K,\quad K_D=K\tau(\alpha-1),\quad \alpha>1.$$

5.4.2 Lead-Lag Compensator

In the previous section, we see that a lead compensator can provide desired phase margin at desired crossover frequency which is directly related to the bandwidth of the system. However, the closed loop system with only a lead compensator cannot guarantee zero steady-state error to a step input. Accordingly, we now design a lead-lag compensator, which can be also viewed as a PID controller, to add the advantage of zero steady-state error. Equation 5.10 below indicates the expression of the lead-lag

controller we use.

$$\text{LeadLag}(s) = K(\frac{\alpha\tau s + 1}{\tau s + 1})(\frac{T_i s + 1}{T_i s}) \qquad (\text{where } \alpha > 1) \tag{5.10}$$

As discussed in the previous section, α decides how much additional phase to add at the desired crossover frequency and the control gain, K, and time constant τ determine the location of the crossover frequency and system stiffness. We choose to add 55° at the crossover frequency of 55 Hz this time. The location of the desired crossover frequency is decided such that it stays far enough from the resonance region so as not to excite any natural modes the plant has. As a result, $\alpha = 10$, $\tau = 9.15 \times 10^{-4}$ sec, and $K = 12.57$ are selected. In order to find an appropriate value of T_i, let us examine the effect of T_i on the controller by looking at Figure 5-19.

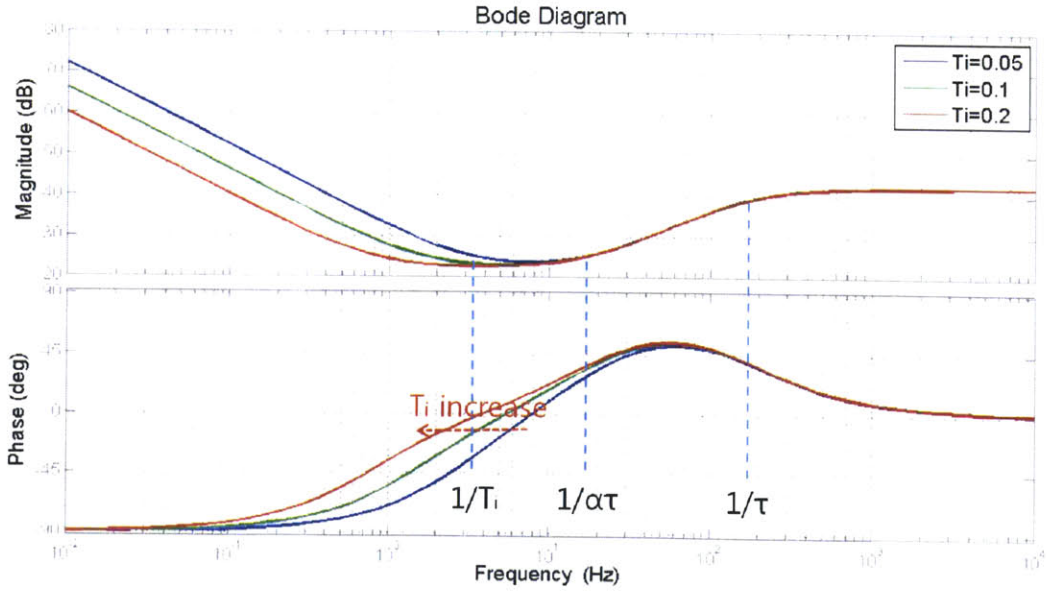

Figure 5-19: Effect of T_i on the lead-lag compensator.

Figure 5-19 illustrates how the frequency response of the lead-lag controller itself changes according to the value of T_i, as well as the location of break frequencies

defined in terms of the parameters. From the figure, we see that as T_i increases, the location of the first singularity, a zero, moves to the left and this can affect the phase-subtracting location of the loop transfer function. This is graphically shown in Figure 5-20.

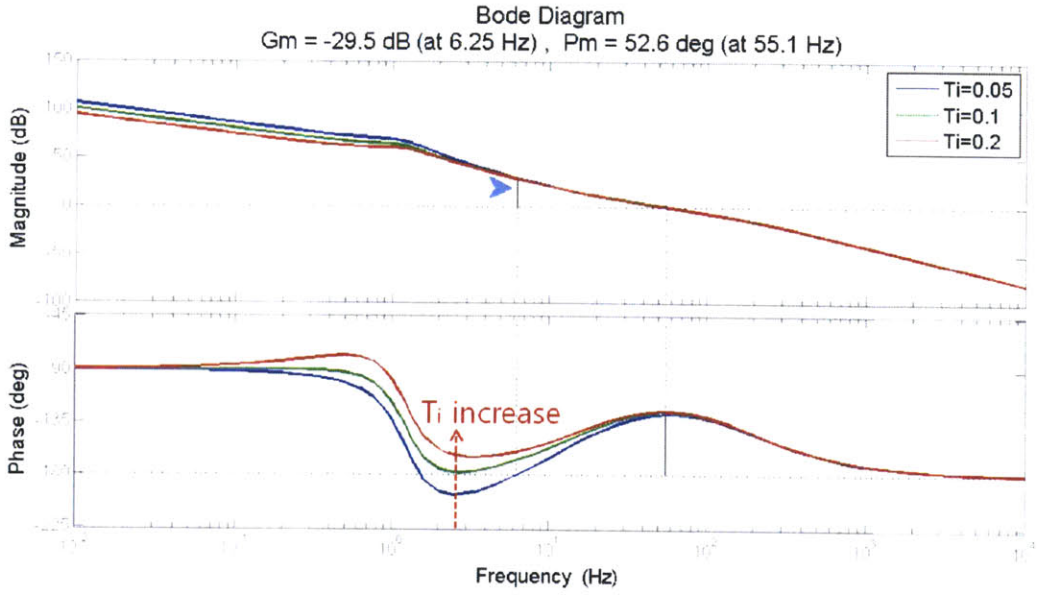

Figure 5-20: Effect of T_i on the loop transfer function.

As shown in the figure above, a small value of T_i can make the phase plot of the loop transfer function cross the $-180°$ line twice. This does not make the system unstable, however, it does make the system have a finite gain margin, which is indicated with a blue arrow in Figure 5-20. Accordingly, here we choose $T_i = 0.2$ and thus the lead-lag controller we implement is following.

$$G_c(s) = \text{LeadLag}(s) = \left(\frac{0.115s + 12.57}{0.000915s + 1}\right)\left(\frac{0.2s + 1}{0.2s}\right) \tag{5.11}$$

Figure 5-21 below now indicates how this lead-lag compensator modifies the frequency response of the open-loop plant. As expected, the crossover frequency is placed at 55 Hz and the phase margin is approximately $55°$.

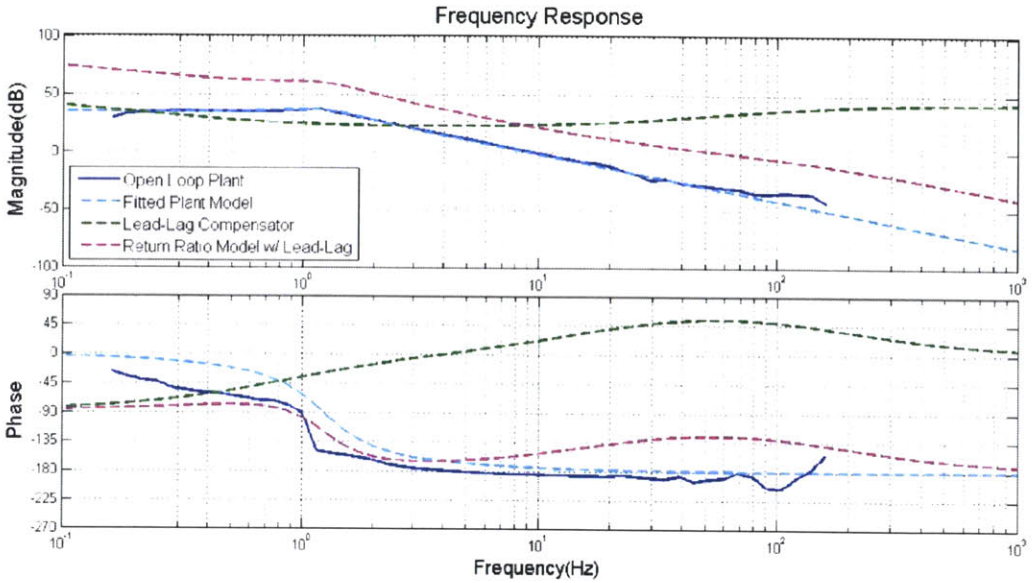

Figure 5-21: Frequency response of the loop transfer function with the lead-lag compensator.

This lead-lag compensator is implemented in discrete-time with the Labview programming tools. In Labview, the control loop is implemented inside a while loop, which has a loop time of 50 μs (sampling rate = 20 KHz). The discrete transfer functions with a sampling time of 50 μs are shown below, and the Labview coding for the controller implementation is attached in Appendix A.

$$\text{Lead}(z) = \frac{125.7z - 125}{z - 0.9468} \tag{5.12}$$

$$\text{Lag}(z) = \frac{z - 0.9998}{z - 1} \tag{5.13}$$

5.4.3 Trajectory Generation

In general, a high loop gain requires the large control output from a controller and it can often cause saturation. Although the loop gain for our system is not extremely large, it is large enough to amplify the position error to the point where the control

effort saturates and the actuator arm hits a hard stop when a somewhat large step input is given. In our system, the reference and the position output are given as encoder edge counts where 1 count is equivalent to shaft's rotational displacement of 3 μrad and the approximately linear motion of the end effector, 0.45 μm. For the picking process, the tip has to be able to move in the approximate range of 20 mm and this is almost 45000 counts, which is too large value to give as a step input to the system. This requires us to generate a trajectory command smooth enough to avoid the control output saturation and large overshoot. We here choose a cubic polynomial for our smooth trajectory which is shown below in Figure 5-22.

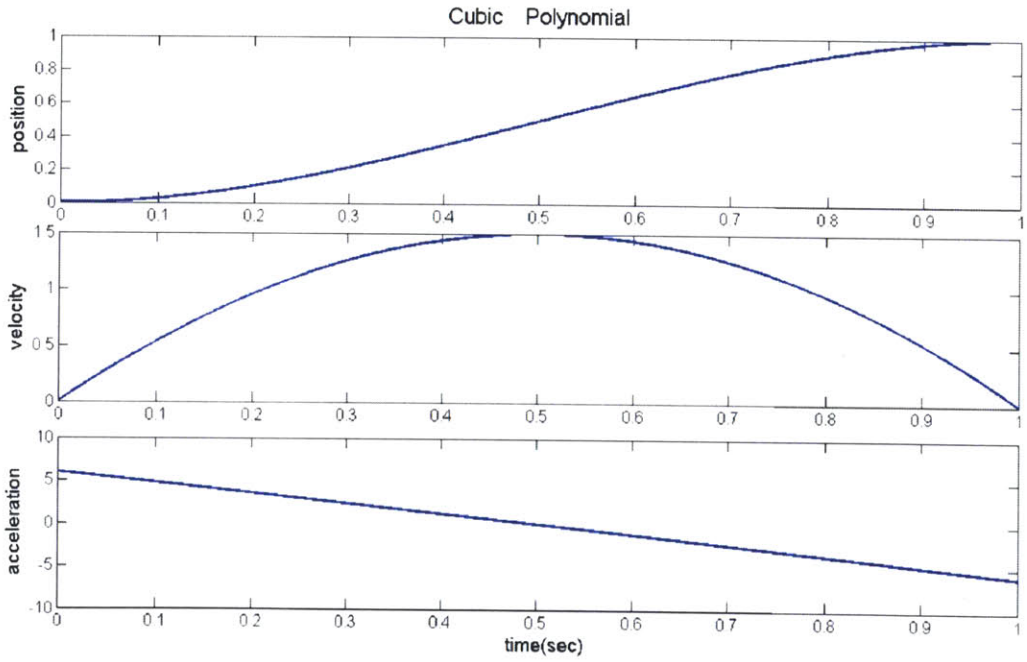

Figure 5-22: Position, velocity, acceleration profile of the cubic polynomial.

The position x can be expressed as a third order polynomial in time t of

$$x = a_0 + a_1 t + a_2 t^2 + a_3 t^3 \tag{5.14}$$

with four conditions of

$$\begin{cases} x(0) = x_c & : \text{ current position,} \\ x(t_f) = x_{ref} & : \text{ final position (reference),} \\ \dot{x}(0) = 0 & : \text{ zero initial velocity,} \\ \dot{x}(t_f) = 0 & : \text{ zero final velocity,} \end{cases}$$

where t_f is the final time in second.

The four coefficients of Equation 5.14 can be found with the four conditions given above. The final expression of the cubic polynomial is

$$x = x_c - \frac{3(x_c - x_{ref})}{{t_f}^2} t^2 + \frac{2(x_c - x_{ref})}{{t_f}^3} t^3 \ . \tag{5.15}$$

In our application, x_c is the current position that we measure with the optical encoder in real-time and x_{ref} is the reference position that we give as a command for the system to follow. Time t_f is the final time of this trajectory, so the smaller value it is, the faster the trajectory is. Figure 5-23 shows the basic concept of the implementation of the trajectory, and the detailed Labview coding for this trajectory generation is provided in Appendix A.

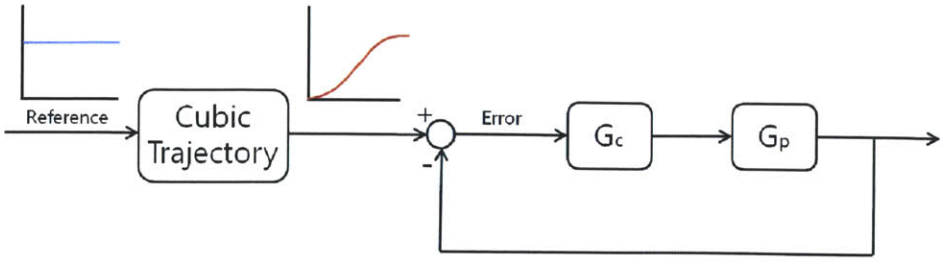

Figure 5-23: Implementation of the trajectory generation on the control loop.

5.5 System Performance

In this section, we discuss the performance of the controlled system with the lead-lag compensator we designed in the previous section by looking at its step response.

5.5.1 Time Response Analysis

Examining a step response, we understand many features of a system: rise time, settling time, overshoot, and more. Let us first look at the step response of the analytical model of the system, and compare to the experimental results.

We discussed the effect of T_i on the system's loop transfer function in the previous section, and here Figure 5-24 shows its effect on the step response of the closed loop system. As shown, T_i does not have significant effect on the step response although it somewhat decreases the overshoot and elongates the settling time as T_i increases. In the previous chapter, we chose $T_i = 0.2$ and the red line in Figure 5-24 shows the step response of the system with this value. According to this analytical response, the rise time (10% to 90%) is 3.31 ms, the settling time is 23.8 ms, and the overshoot is 22.8% at 8.86 ms.

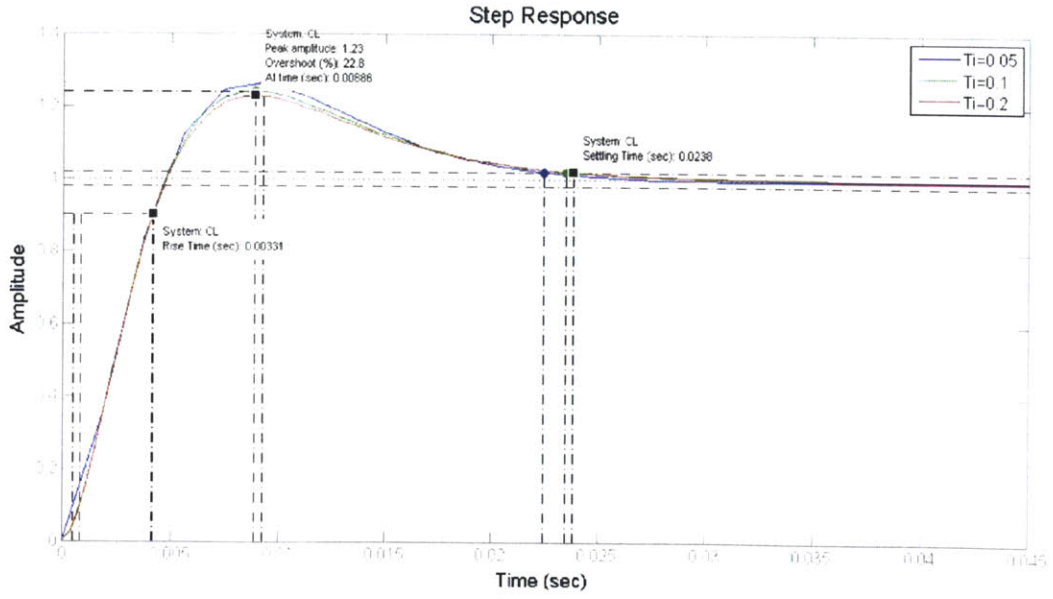

Figure 5-24: Effect of T_i on the unit step response of the closed loop system.

The error plot in Figure 5-25 helps indicate fine settling and elongated settling time as T_i increases.

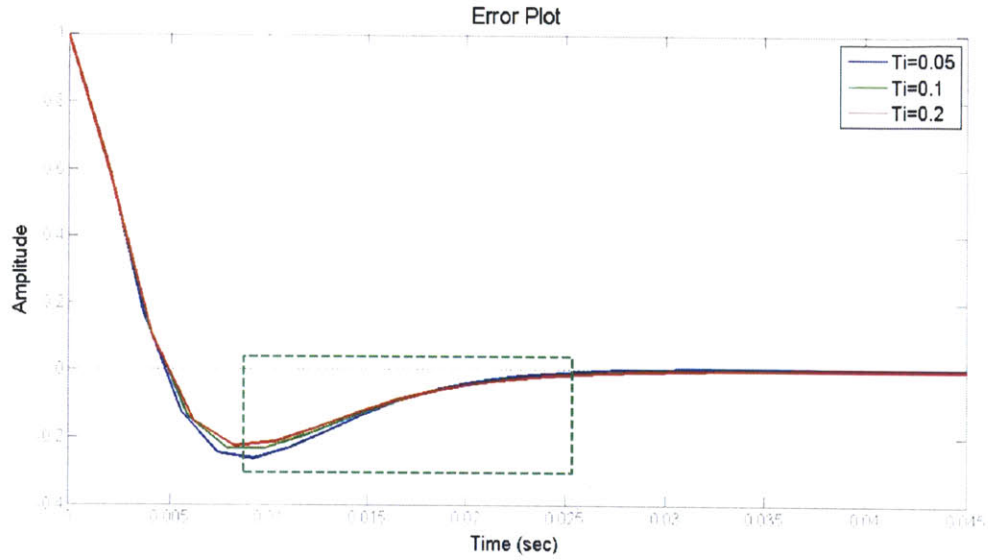

(a) Error plot

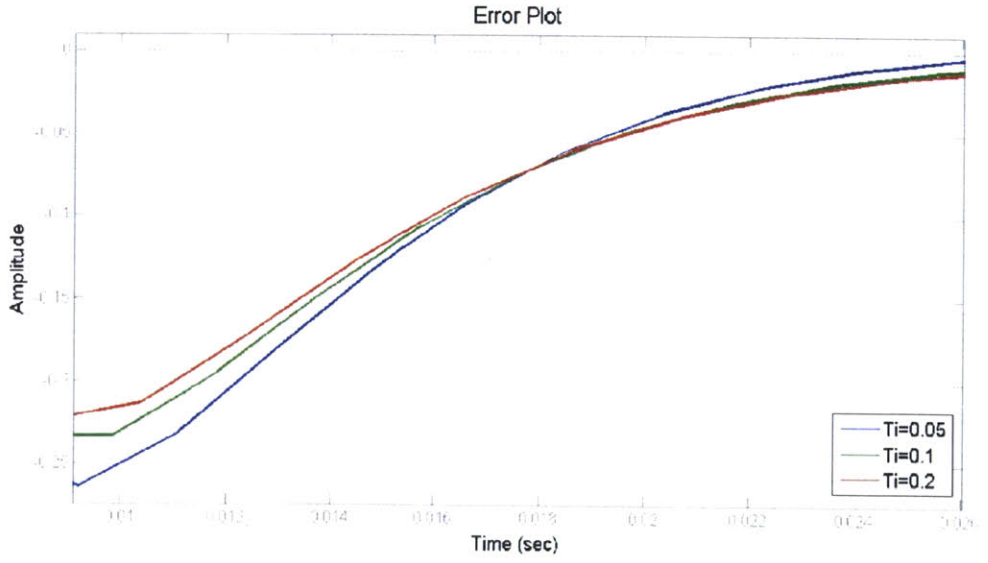

(b) Magnified part

Figure 5-25: Error plot of step response of the closed loop system.

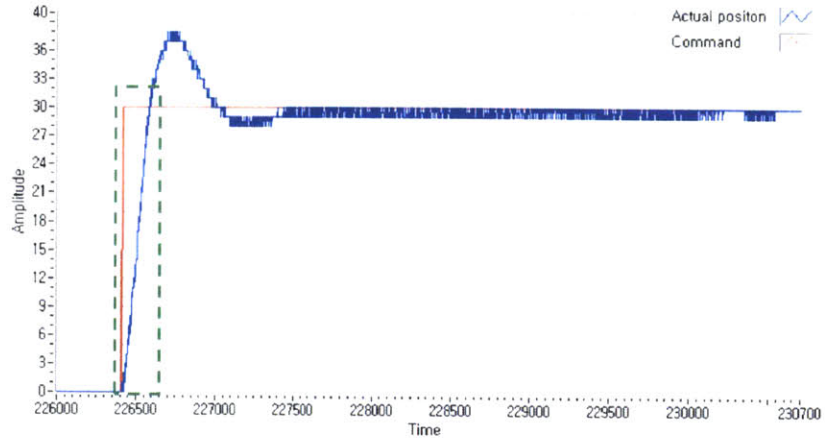

(a) Step response. Y axis is in encoder counts.

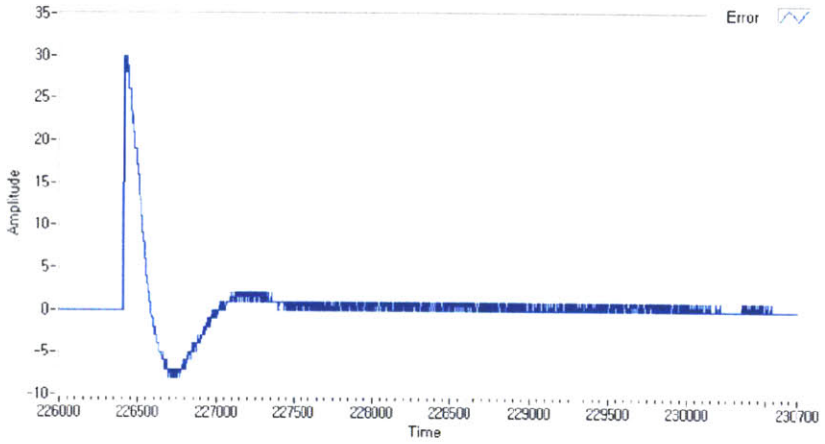

(b) Error plot. Y axis is in encoder counts.

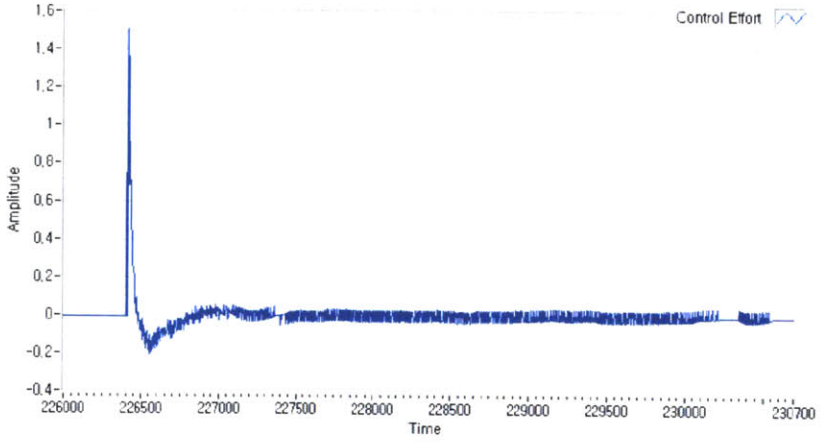

(c) Control effort. Y axis is in voltage

Figure 5-26: Measured time responses of the closed loop system. X axis is in clock ticks of 50 μs.

In order to see the true performance of the physical system, several time responses are experimentally measured and displayed in Figure 5-26. First of all, the experimental step response in Figure 5-26(a) looks very much like the analytical one from Figure 5-24. In this case, the step input is in the encoder edge counts of 30 and the X-axis indicates time such that the scale interval of 1 is equal to the loop time, 50 μs. By looking closely at this figure, we find that the rise time, $T_r \simeq 5.5$ms, and the overshoot, $\%OS \simeq 23.3\%$ at $T_p \simeq 12.5$ms. These values are somewhat different from what we have in the analytical model; however, we can say it is within reasonable agreement.

Figure 5-27 illustrates a magnified part of Figure 5-26(a), and we can observe a delay of the system.

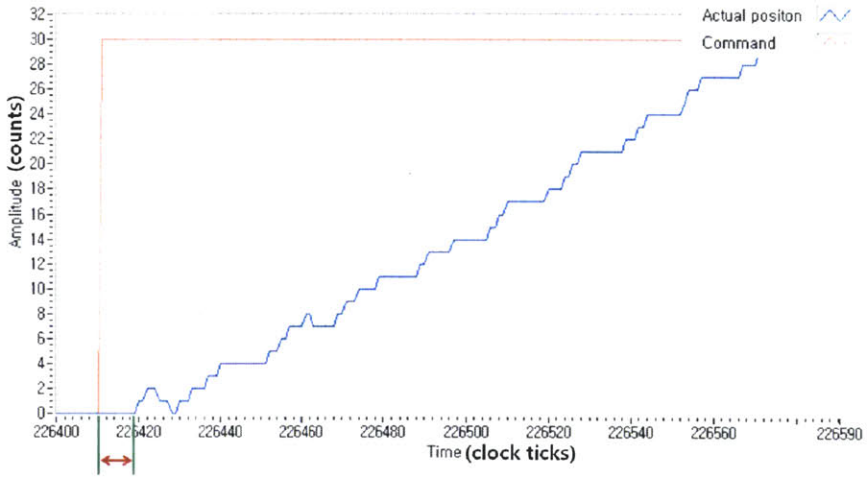

Figure 5-27: Magnified portion of the beginning of the step response with a delay.

In theory, the servo position has to follow the command immediately. However, there can be a delay of some sort in a real hardware system. As shown in the figure, the blue line which is the response begins approximately 7 clock intervals after the step input, and since one interval is equal to 50 μs, it means a delay of 0.35 ms. Looking closely at the control output plot in Figure 5-26(c), however, we find out that the control effort begins to increase only one sample after the given input, which

makes sense because the updated value of the input is applied to the next loop. This means that the delay of the servo position is caused during one of the following steps or some combination of them. First, we considered the maximum output of the DAQ device. That is, if the calculated value of the control output is sent out through the DAQ device with lower speed than the control loop time, this might be the cause of the delay. However, the maximum output speed is specified as 333 KHz which is much faster than the loop and so it is not likely that this step has a significant effect on the delay. Then the next step we considered is when the optical encoder reads the position of the actuator and sends quadrature output to the FPGA card for edge counting. These steps also do not seem to cause such a delay since the encoder output speed is 28.8 MHz and the FPGA counting clock is 80 MHz which are significantly faster than the loop frequency. The final step we are suspicious of the most is when the encoder counts are transferred back to the real-time control loop. When the real-time control loop takes the next loop, it requests the edge count value from the FPGA. If the data transfer is not complete over one loop period, the loop has to begin its work with the previous count value, causing a delay. The data transfer from the FPGA card to the real-time controller may not be the only culprit for the delay; however, it is the most likely the main source of the delay.

In Chapter 5, we have discussed how the overall system is integrated with the parts explored in Chapter 3 and 4. We have also explained the control architecture for the XY microscope stage and the Z-axis servomechanism together with the system responses in both time domain and frequency domain. With the controllers, the XY plane motion has a resolution of 0.16 μm and the Z-axis motion has a resolution of about 0.45 μm with the crossover of 55 Hz. In addition, while explaining the design process of the controller, we introduced several interesting phenomena including mass disconnection, mass tuned damper, amplitude-dependent frequency response, and the Dahl resonance. In the following chapter, we discuss how we conduct experiments with the prototype system where our controller is implemented, and the results are also explored.

Chapter 6

Experiments, Results, and Challenges

This chapter discusses why and how the experiments are conducted using the prototype of the robotic single-cell manipulator. We also discuss the experimental results and challenges encountered during implementations and experiments.

6.1 Experiment Process

The main purpose of the experiment is to see if it is possible to effectively pick a cell or a microbead out of a microwell and how reliable it is. Before the actual picking experiment, several things should be appropriately prepared. First of all, PDMS microwells should be treated to have hydrophilic behavior. This is because PDMS itself is a very hydrophobic material and this property causes a number of bubbles around the wells, thereby making the process of cell or microbead-distribution difficult and also obstructing the view of microwells' inside. Trapped bubbles are shown in Figure 6-1 below. Figure 6-1(a) and 6-1(b) show one block (7×7, 50 μm each) of microwells when the PDMS stamp is in hydrophilic state and hydrophobic state respectively.

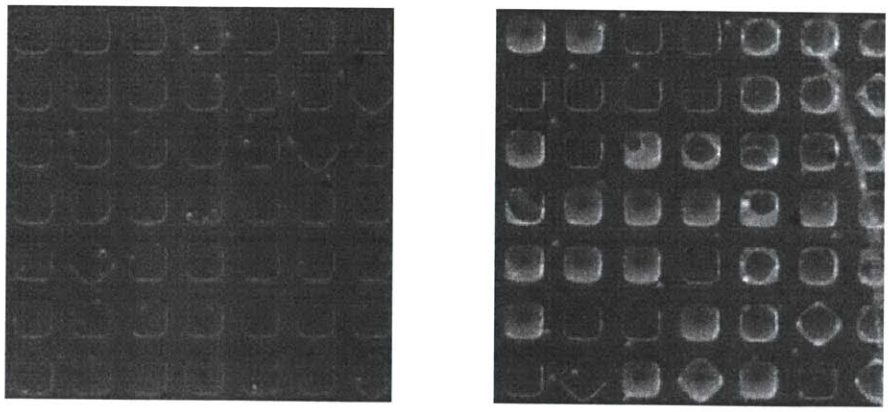

(a) Hydrophilic state (b) Hydrophobic state

Figure 6-1: Bubbles trapped around microwells in hydrophilic and hydrophobic states.

After manufacturing microwells by casting with Polydimethylsiloxane (PDMS), it has to be treated with plasma to be hydrophilic. Then, PDMS microwells are placed in a container with liquid and stay immersed to avoid any exposure to air because any contact with air turns the material back to hydrophobic state. The liquid we choose to use for this purpose is phosphate buffered saline (PBS). PBS is a water-based salt solution containing sodium chloride, sodium phosphate, potassium chloride, and potassium phosphate in it. As one of the buffer solutions, it is commonly used in biological research since it is isotonic and non-toxic to cells.

Since microwells have to stay hydrophilic to provide better environments for the experiment, this PDMS stamp should also stay immersed in PBS when placed onto the inverse microscope we designed and built in the previous chapters. Once the PDMS stamp is in position, a syringe in the syringe pump and the tubing have to be filled with PBS, the same liquid in which the PDMS stamp is immersed. For the filling process, a relatively larger syringe, volume of 1 mL, is first utilized to fill the tubing and the pipette module. When trying this, a straight streamline should be observed out of a glass pipette to make sure that the pipette is in good condition and there are no air bubbles trapped inside. Then, this large syringe is detached from the syringe pump and a glass syringe with the volume of 50 μL filled with PDB is implemented for the actual task of cell- or microbead-retrievals in order to allow fine

volume control.

After the PDMS stamp and the syringe pump become ready, microbeads are deposited onto the microwells and are settled into the wells by gravity. For the purpose of the picking experiment, microbeads of 10 μm are first used instead of actual living cells. When depositing microbeads, it is also important to decide the concentration of beads. Three different concentration rates have been tried: 0.05 %, 0.25 %, and 0.5 %, and the 0.5 % concentration is selected for the experiment because it provides the proper number of beads to work with, neither too dense nor too sparse.

Now the Z-axis picking module has to be properly calibrated and it mostly concerns two calibrations. One is for the reference to which we can define the exact distance to the surface of a PDMS stamp. Since we have an issue with the index pulse discussed in Chapter 4, we choose the upper hard stop described in Chapter 3 as the reference of the Z-axis movement. As soon as the prototype of the robotic single-cell manipulator begins to run, the Z-axis picking module goes up to a point where it touches the upper hard stop. This point is then set to be the reference and the module now goes down until it touches the surface of a PDMS stamp. From this process of calibration, we find out the exact distance between the reference, the upper hard stop, and the PDMS stamp's surface. The way to see if the tip of a glass pipette certainly touches the PDMS surface is to observe the change of brightness and distortion of wells' edges as described in Figure 6-2.

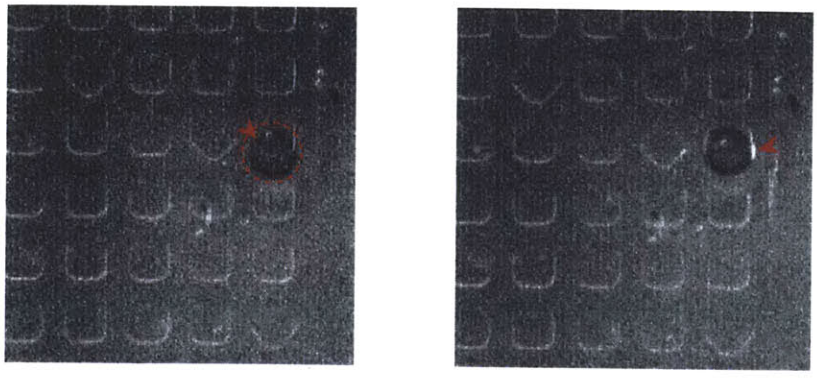

(a) above the surface (b) on the surface

Figure 6-2: Tip of the picking module on the surface of PDMS microwells.

Figure 6-2(a) shows a part of a PDMS stamp and we can find the position of the picking module tip by looking at the brightness change, the dark area. In this case, the tip is not really touching the surface, but it is only a bit above the surface. In Figure 6-2(b), however, we know the tip is now touching the surface by looking at the distorted part of a well pointed with a small red arrow. For actual picks, it is good to note that retrieval process becomes more successful when the tip not only touches the surface but also reaches a bit into a well.

The next calibration we need is to select a reference well and align it to the landing position of the tip. In this prototype, the Z-axis picking module is fixed at a certain position on the mechanical stage, and the XY microscope stage controls the position of microwells on the XY plane. Accordingly, after the first calibration of Z-axis motion, one reference well is selected and the microscope stage moves the PDMS stamp such that the selected reference well is located where the tip is expected to land. This way, we can have the reference position where a microwell of interest has to be moved in order for a target cell or microbead to be retrieved. Figure 6-2(b) also shows a good alignment with the reference well and the tip.

Once all this preparation is appropriately completed, the prototype is ready for the actual picking experiment. First, a target well is selected and is moved to the position of the reference well. The tip of the picking module is then driven down to the surface of the PDMS stamp. This process can be easily done since these have been appropriately calibrated beforehand. Once the tip touches the rim of a target well, a syringe pump aspirates approximately 1 μL to 2 μL of PBS from the microwell, which correspond to 1000 to 2000 steps in the microstep mode as described in Chapter 4. For picking experiment with microbeads, a constant aspirating speed of 900 steps per sec is used; however, this speed can be easily adjusted by users with the control panel discussed in Chapter 4 for better performance with specific applications. After this aspiration, we lift the tip from the surface and observe the target well to see if the retrieval is successful.

The picking experiment has been conducted with following the exact protocol described above and the results are discussed in the following section.

6.2 Results and Discussions

In this picking experiment, microbeads of 10 μm diameter with the concentration ratio of 10 μL of beads to 2 mL PBS is used instead of living cells. Experiments with living mammalian cells is considered to be a future work. Microwells of 50 μm cubed and a 50 μm pipette tip are also used for the experiment. Figure 6-3 below shows one block of PDMS microwells containing microbeads in some of the wells. The target bead indicated with a black arrow in Figure 6-3(a) is successfully aspirated and we can check this by looking at the same well in Figure 6-3(b).

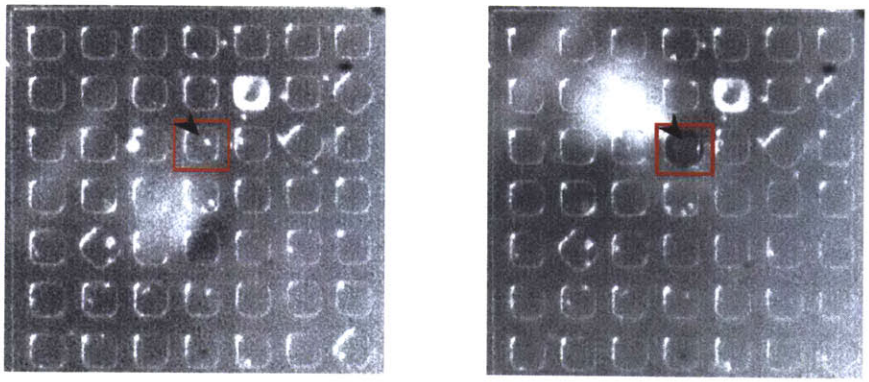

(a) Before (b) After

Figure 6-3: One block of PDMS microwells before and after the cell-retrieval with the prototype.

The volume of one well is 125 pL, so in theory, aspirating this much should be enough to pick a cell or microbead; however, it is not quite the case in practice because there is adhesion of a cell or bead to the walls of a well and liquid covering other parts of the PDMS stamp can be also aspirated together with the liquid inside of a target well. In our experiment, sometimes picking was successful with the aspiration of 0.2 μL, while 2 μL were required for some other times. This might depend on how long the beads have stayed in the wells since the longer they stay, the more they tend to adhere to the walls. Accordingly, most of experiments were conducted right after microbeads had been deposited on a PDMS stamp and the average of 1 μL to

2 μL aspiration, 1000 to 2000 steps of the syringe pump, was used to make sure of successful picks.

The retrieval process itself takes the average of 5 to 10 seconds, and the testing of the prototype results in reliable cell-retrievals with the success rate of more than 90 percent. More experiments with actual living mammalian cells should be conducted as a future work.

6.3 Challenges

In this section, we discuss some of the challenges we have encountered while designing, implementing, and testing the proposed system, robotic single-cell manipulator. We also suggest possible ways to tackle these issues and provide answers to some of challenges we were able to resolve.

6.3.1 Illumination

A fiber optic illuminator by Dolan-Jenner Industries is used, as shown in Figure 4-1, to illuminate the PDMS stamp and so provide better contrast to its images. When the illuminator is placed right above the pipette module, however, the shadow of the arm extension hinders the illumination. Placing the illuminator with a certain angle also ends up to be poor illumination due to shadows and reflection. Even though the images of microwells containing microbeads are visible as shown in Figure 6-1, 6-2, and 6-3, they could have been much better with a more proper illuminator.

We suggest that a ring illuminator should be a very suitable choice for this application. Mounting a ring illuminator between the pipette module and the microscope stage, we can avoid any unnecessary shadows and minimize the reflection. Figure 6-4 shows the suggested mounting area for a ring illuminator.

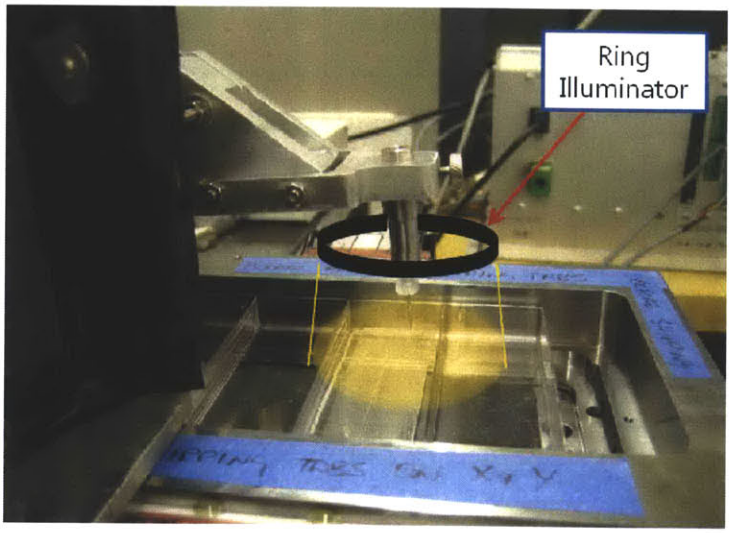

Figure 6-4: Suggested position to place a ring illuminator.

Many types of ring illuminators are now commercially available at reasonable prices, but making one with several light-emitting diodes (LEDs) placed in a ring-shape circuit board might be easier, faster, and more economical.

6.3.2 Encoder Alignment and Calibration

After implementing the actuator, encoder, trajectory generation, and the controller to get the Z-axis mechanism working, we tested its motion to see if it works the way we want. At a quick look, it seemed to follow the trajectory command well without large errors. However, sometimes the system made a buzzing sound together with an unexpected oscillation, which is illustrated in Figure 6-5. Figure 6-5(a) shows the trajectory response where the red line is trajectory command and the white line is the following response. Also, the corresponding control output is plotted in Figure 6-5(b) and an oscillation with the same frequency is also observed in this control output plots.

Before trying to find the cause of the oscillation, we need to understand the operation settings of the system:

- The encoder outputs, phase A and phase B, are connected to the FPGA card.
- The maximum encoder output is 28.8 MHz and the interpolation level is selected as $\times 256$ to increase the resolution.
- A quadruple ($4\times$) decoder implemented in FPGA counts the encoder's A-quad-B output edges.
- The FPGA card sends the counts to the real-time controller.
- In the real-time controller, a discrete lead-lag compensator is implemented to control the Z-axis motion with the encoder's position feedback data from the FPGA decoder. The control loop time is 50 μs.
- A trajectory generation is implemented in the real-time controller to provide smooth motion to the Z-axis actuator.

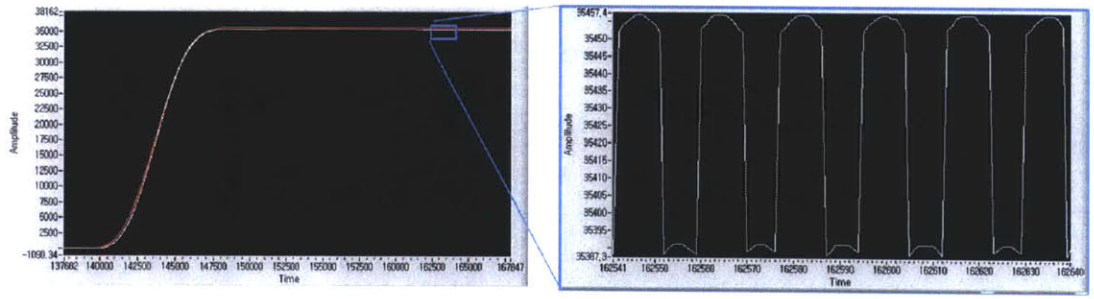

(a) Trajectory response

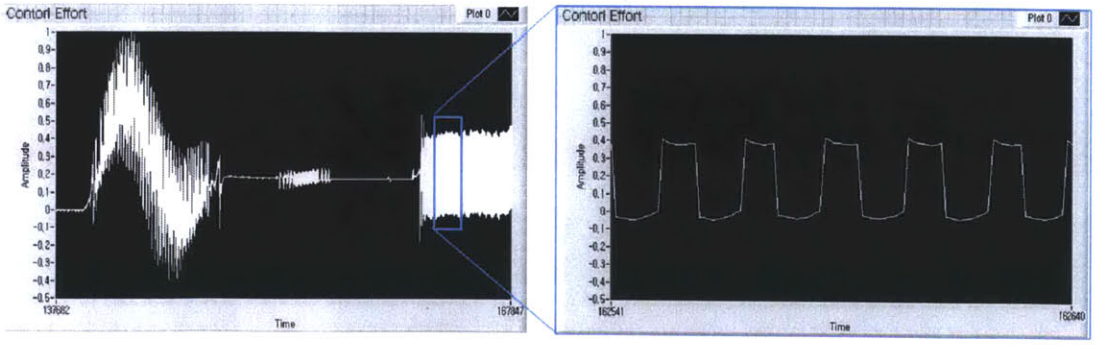

(b) Control output

Figure 6-5: Unexpected oscillation in the closed-loop time responses.

Now from observations and Figure 6-5, we find several characteristics of the oscillation:

- The unknown oscillation is not consistent. That is, it comes and goes from time to time.
- It does not depend on the position of the Z-axis actuator and seems to occur very much randomly.
- The oscillation occurs when the control loop is closed.
- When it happens, the amplitude and frequency of the oscillation are about 64 encoder counts and 1.2 KHz respectively.
- The oscillation signal looks close to a square wave rather than a sinusoidal wave.

When finding a cause of an issue, it is good to list possible causes and rule out the obvious ones first. The first one we could think of as a possible cause was the presence of loose parts. Accordingly, we checked every fastening components, such as bolts and nuts, and fastened them tightly again; however, the oscillation was still observed even after this trial. Then, we became suspicious that there might be some resonance dynamics at around 1 KHz because we only obtained the frequency response of the plant up to 200 Hz or so. We tried decreasing the Z controller loop gain low enough to avoid any resonance, if there is, at around 1 KHz, but this could not make the buzzing sound go away either. Together with this trial, the fact that the oscillation comes and goes inconsistently also guided us that it is not likely from a resonance dynamics at high frequency.

While trying to find the cause, more interesting behavior was observed. We wanted to try to remove the unwanted oscillation by using a low pass filter, and so we implemented a discrete low pass filter with the cutoff frequency of 100 Hz. However, instead of removing or attenuating the oscillation, the low pass filter changed the frequency of the oscillation with the amplitude intact. More interestingly, the frequency of the oscillation became lower as the cutoff of the low pass filter decreased. This result

strongly supports that it is surely not from any high-frequency resonance dynamics, and also made us consider that software calculations in the controller or data transfer could be the cause. Since the amplitude of 64 counts stayed the same, we became suspicious that the seventh bit of the decoded data might be corrupted or altered while transferred from FPGA to the real-time controller. Accordingly, we debugged the Labview coding of the controller part to make sure that there is no calculation error, and also implemented a handshaking protocol for the data transfer between the FPGA and the real-time controller so as not to loose or make alteration of any transferring data. In addition, we utilized several different ways of data transfer to rule out the possibility that the transferring method we used was problematic. Even with all this debugging, however, the oscillation stayed the same.

We also considered that the interpolation itself or interpolation level could have something to do with the strange oscillation. First, we asked MicroE for a new interpolator with the same interpolation level of $\times 256$ and tried the new one, but the result was the same. As for the interpolation level, since it is fixed value and requires additional software, we decided to try double ($2\times$) decoder instead of quadruple ($4\times$) counting. Even with the $2\times$ decoder, the oscillation still occurs but the amplitude changed. Figure 6-6 below illustrates the strange oscillation with the double decoder.

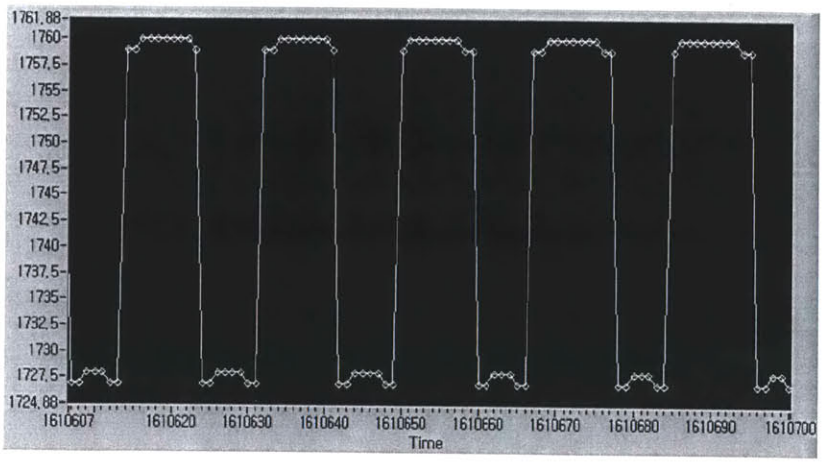

Figure 6-6: The strange oscillation occurred with double ($2\times$) decoder.

As shown in the figure, the amplitude decreased to 32 counts with the double decoder. In fact, this 32 count-amplitude corresponds the same physical movement as the 64 count-amplitude with the quadruple decoder because 1 count in the 2× counting mode is equivalent to 2 counts in the 4× decoding mode, which is 6μrad. However, if the oscillation were from the alteration or corruption of a data bit, the amplitude would have had to remain the same. As a result, this led us to consider that the encoder itself might be giving unwanted noise to the system.

Accordingly, we looked closely at the quadrature output of the encoder while the strange oscillation was happening. Figure 6-7 shows the captured screen of the oscilloscope with A-quad-B signals.

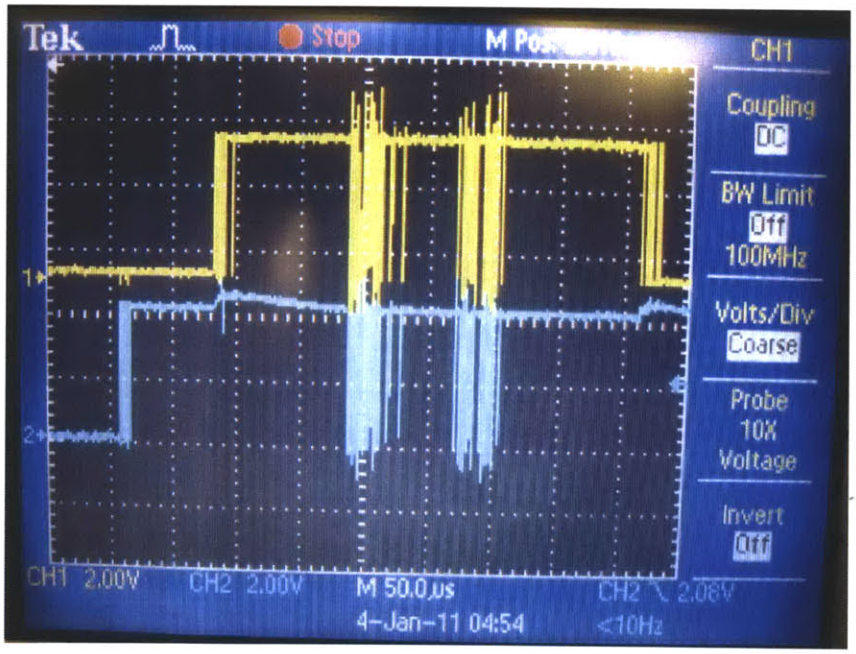

Figure 6-7: A-quad-B encoder output signal when the oscillation occurs.

As shown in Figure 6-5(a) and Figure 6-6, the 64 or 32 count-jump takes only one loop time which is 50 μs, and Figure 6-7 shows corresponding jitters within 50 μs. Observing this, we suspected that this random noise from the encoder output signals was the culprit for the oscillation. Then we decided to realign the encoder gratings

and the head although we did not consider realignment at the first place because the FPGA decoder seemed to give right edge counts whenever the position changed. It turned out that the MicreE encoder is much more sensitive to alignment then we thought it would be. After the realignment of the hardwares and the recalibration of the encoder output, we obtained the time response again, and this time it looked much clean as shown in Figure 6-8.

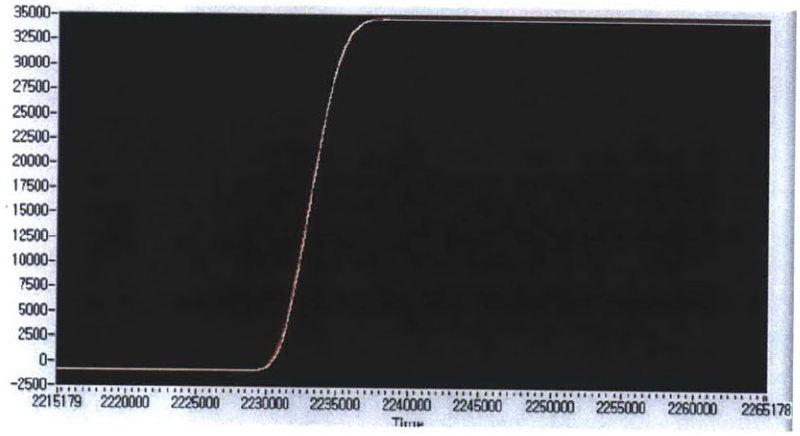

(a) Trajectory response

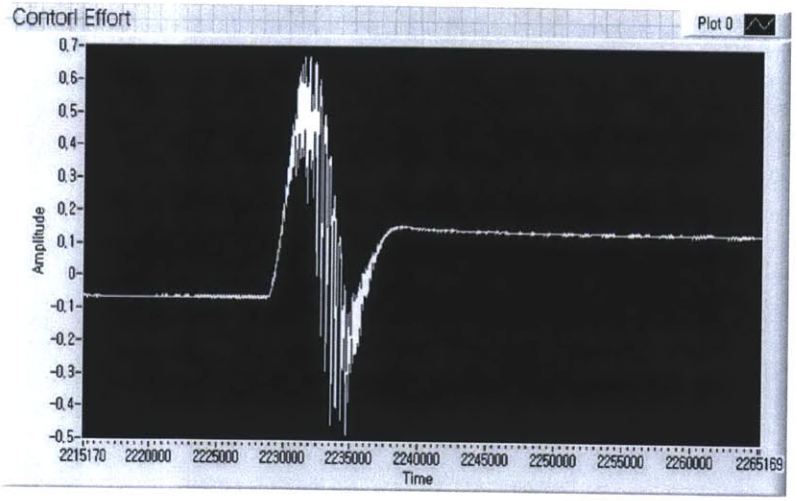

(b) Control output

Figure 6-8: No more strange oscillation after realignment and recalibration.

The trajectory response in Figure 6-8 looks cleaner than that in Figure 6-5(a) since

there no longer exists the strange oscillation. Also, the control output plot looks to have much less fluctuation due to the absence of the unnecessary oscillation. More importantly, the accuracy has also improved with the steady-state error going to zero since the encoder output no longer contained jitters and became more reliable.

In this section, we have explored challenges we encountered during the research. For the illumination, we suggest using a ring illuminator to avoid any shade and reflection issue and the ring illuminator can be easily built with several LED's and simple circuits. As for the encoder output, we suggest suspecting the alignment first when there is unexpected output, and we recommend that alignment should be done with great attention at the first place to spare extra time and effort.

Chapter 7

Conclusion and Future Work

In this thesis, we have discussed the design and implementation of a robotic single-cell manipulator and also the experiments of the prototype system. Our research has focused specifically on a simple and compact design of the cell picker and its control for high accuracy in cell-retrieving process.

In the design process, we have described the selection of the linear stages for the XY positioner, the Z-axis mechanism, the Z-axis actuator and the rotary encoder. As for the Z-axis motion, especially, we have shown that the rotary mechanism with the voice coil actuator is preferred to drive the tip of the picking module. In general, a linear mechanism requires heavier structure for the motion and it causes larger reaction on the system during the operation detailed in Chapter 3. As for the actuator, using general-purpose DC motors will require a gear-train which will have backlash issues that can cause non-negligible error on a micro-scale operation. Therefore we chose a direct-drive voice coil motor to avoid such problems and to increase the accuracy of the system. With these selections, the prototype of the single-cell picker was able to successfully retrieve microscopic objects from the microwells with submicron resolution.

Future work on this Z-axis actuation part would involve designing and building a voice coil actuator for the Z-axis motion. We are currently using an old hard disk drive by IBM for the actuator, and the unnecessary and heavy parts are still included because we did not want to damage the actuator while disassembling or cutting

undesired parts. Building a new actuator would eliminate the effort of designing and manufacturing arm extensions and it will also significantly decrease the weight of actuating part, thereby reducing the load on the Y-axis stage.

Selection and implementation of the rotary encoder was another issue. In order to meet the desired accuracy, we needed a rotary sensor with submicron resolution of less than 5 μrad per count. For this purpose, we selected the Mercury 3500 by MicroE which has a resolution of 3 μrad per count with the $\times 256$ interpolation and the typical A-quad-B output with the maximum speed of 28.8 MHz. As explained before, we used our FPGA card to count the edges of the quadrature signals with the clock of 80 MHz and sent the data to the real-time controller. However, it is also possible to directly count edges by using a counter of a Data Acquisition (DAQ) card. Doing this can eliminate the data transfer from the FPGA to the real-time controller and even eliminate the possibility of losing data or delay during the data transfer. Before using this method, however, we need to check if the maximum external source frequency for the counter of the DAQ device, which is only 20 MHz for our PXI 6052E model, is faster than the encoder output. Accordingly, we should consider either using slower output speed for the encoder or purchasing a newer DAQ device with a faster counter clock. With applications requiring not so fast sensor output, we suggest doing the former. As for the encoder implementation, it turned out that MicroE optical encoders are more sensitive to the alignment than we expected, and the ill-alignment can cause significant consequence on the encoder output as we have seen in Chapter 6. Accordingly, we recommend paying good attention to the alignment of the encoder gratings and the head and also consider realignment first when an unexpected noise is detected in the output signal.

There is another future work on the experiment part. As discussed in Chapter 6, we conducted our experiments with 10 μm microbeads. Checking if the picks were really successful, however, was somewhat difficult in that 1)our self-designed microscope system does not have a fluorescence illuminator to detect microbeads picked and placed in 96 well-plates and 2)it is also difficult to place the retrieved microbead back onto a dry PDMS stamp due to the hydrophobic characteristic of the

material discussed in the previous chapter. Accordingly, tests of confirming the picks need to be conducted with fluorescence for the future work. As for the experiments with actual living cells, we could use yeast cell lines since they are easy to handle, and by cultivating the picked ones we can tell if the picks are truly successful. However, since the prototype system is installed in our lab where proper devices for living cells are not equipped, the cells have to be transferred from somewhere else. During this transfer, a portion of the cells can lose their viability and it has to be taken account when deciding the success rate of the cell picks and the viability rate. For this purpose, we suggest taking two samples of PDMS stamps filled with the cells in the same manner and conducting only one of those, leaving the unused one as a control sample we can refer to after the picking experiments. Then, after retrieving enough number of cells, for example on the order of hundreds, we can statistically obtain the rates.

Finally, the automation issue should be also addressed in the future. We have shown that the prototype system can accurately retrieve individual cells from microwells. In order to dramatically increase the throughput of the retrieving process, however, automation is necessary. We believe that our prototype can have a fully automated retrieving process once real-time vision is integrated into the control loop of the system. With vision processing such as setting the coordinates onto images and pattern matching between frames, we can automatically locate the exact position of the target well and have the microscope stage move to that position. For this purpose, we suggest using a better illuminator such as a ring illuminator discussed in Chapter 6. It will provide clearer contrast and be of great help for successful pattern matching and therefore the automation.

In conclusion, we have shown that the robotic single-cell manipulator can potentially contribute to rapid assays of living cells which is a critical process in developing medicine and cures. First, the rotary servomechanism for the Z-axis of the cell picker is capable of yielding higher accelerations than linear servomechanism so that the whole cell picking and isolating process can have higher throughput when the system is appropriately automated. Also, when it comes to the vibration or deflection of the

Y-axis structure caused by the reaction force of accelerating the picking module, the rotary servomechanism of our system has advantage over linear servomechanism. In addition, our careful design of proposed robotic single-cell manipulator has less structural errors than the commercial device. Finally, our design uses simple off-the-shelf components so that the system can be easily and cost-effectively built by anyone in need. We hope that these advantages and development could contribute rapid discovery of treatment and vaccines on a wide range of diseases with potential impact on the society.

Appendix A

Labview codes

A.1 Control panels for the syringe pump, microscope stage, and vision

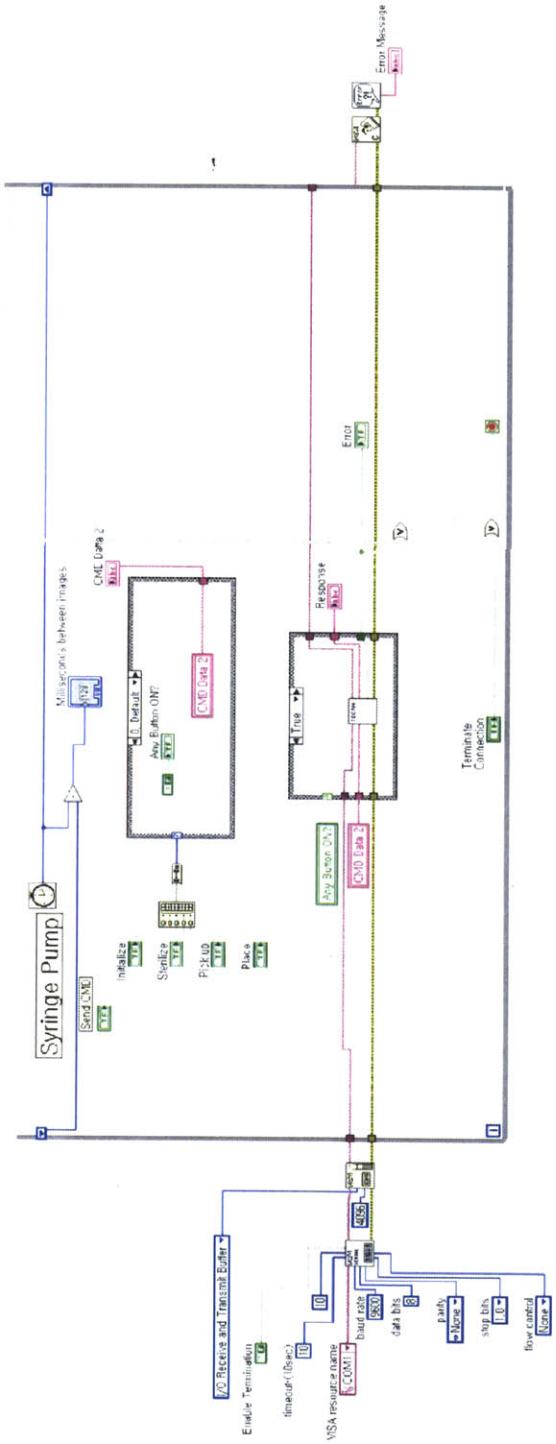

Figure A-1: Labview code for the syringe pump control panel.

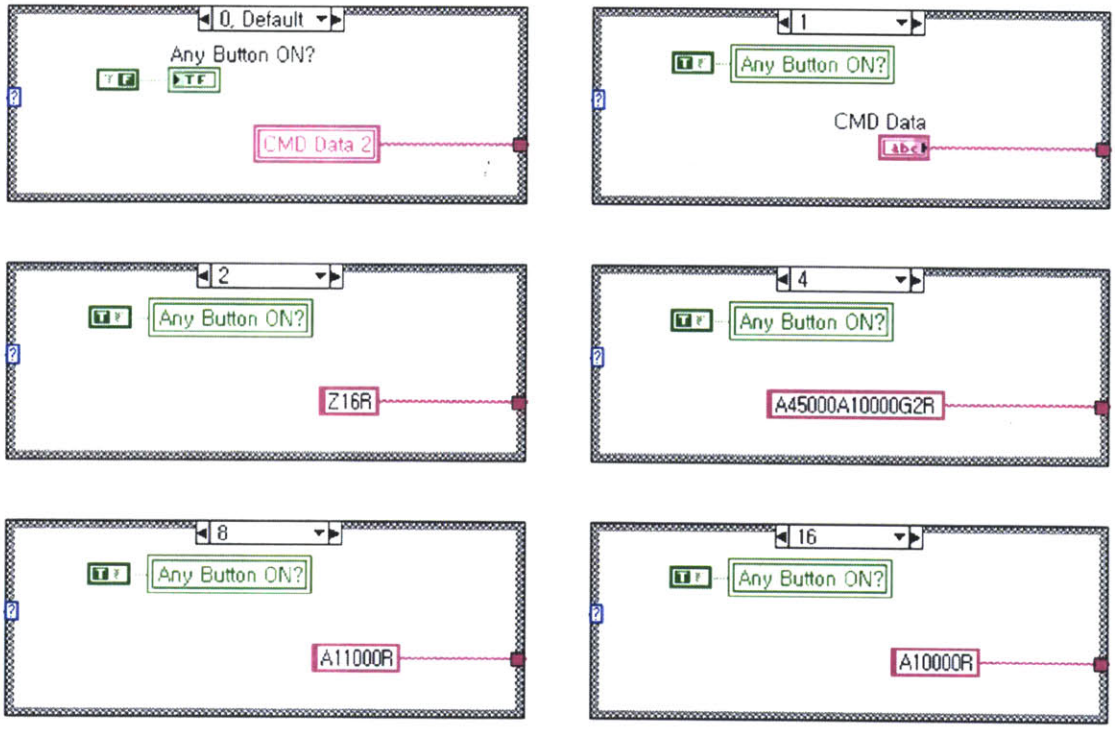

Figure A-2: First case structure in the syringe pump control loop.

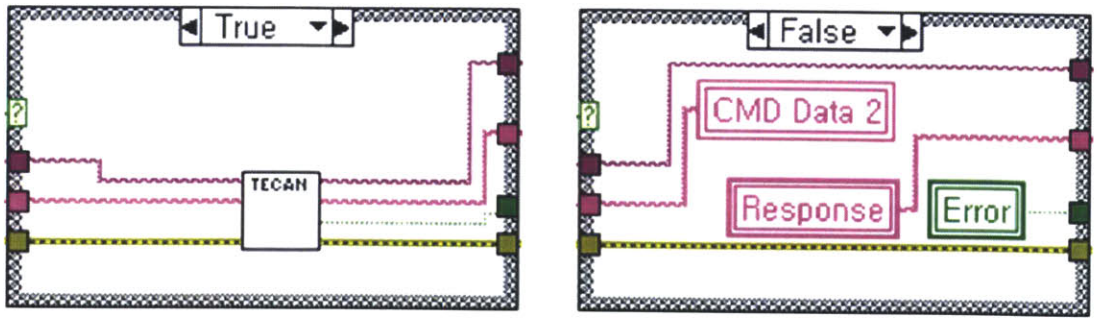

Figure A-3: Second case structure in the syringe pump control loop.

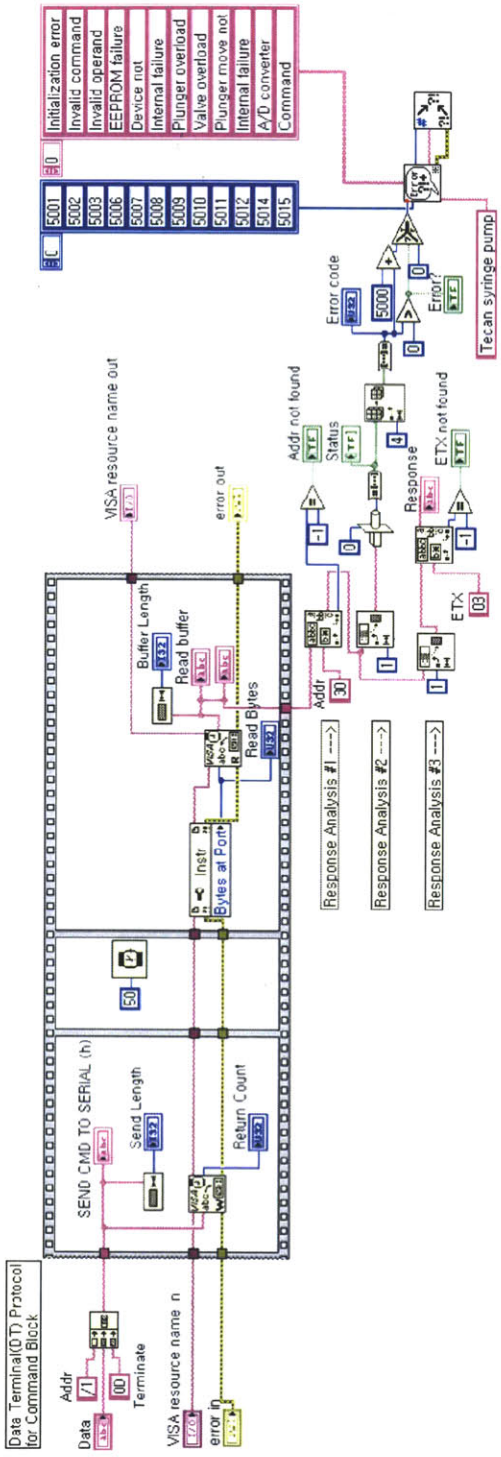

Figure A-4: Detailed code for the Tecan subvi.

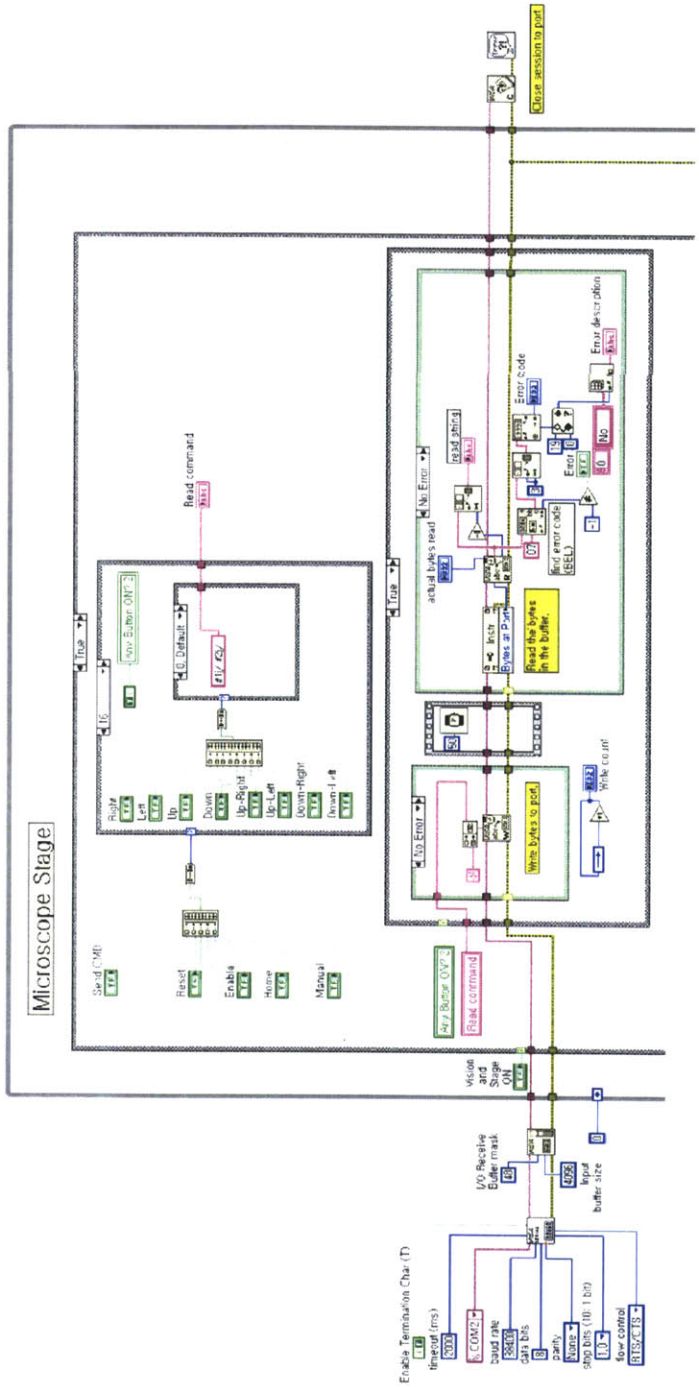

Figure A-5: Labview code for the microscope stage control panel.

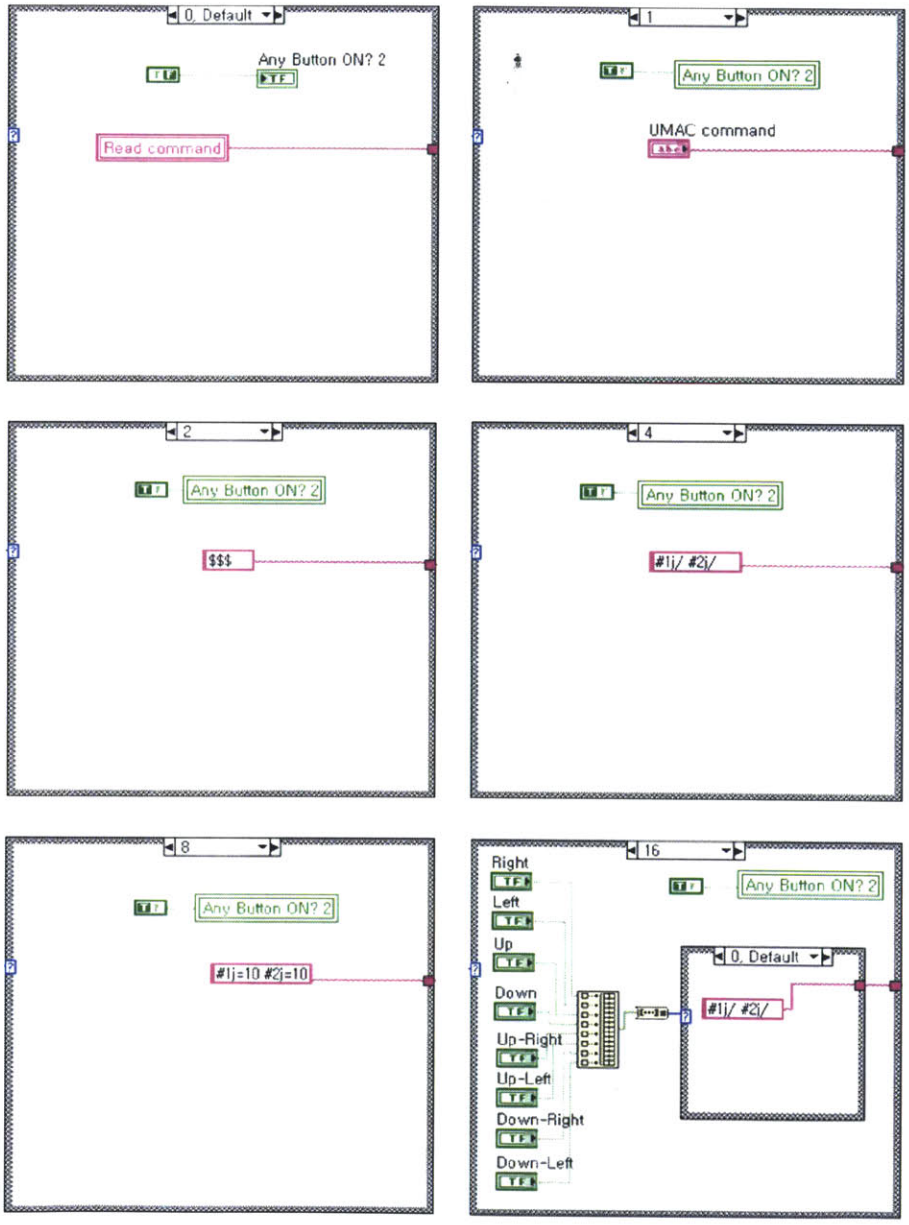

Figure A-6: Case structure in the microscope stage control loop.

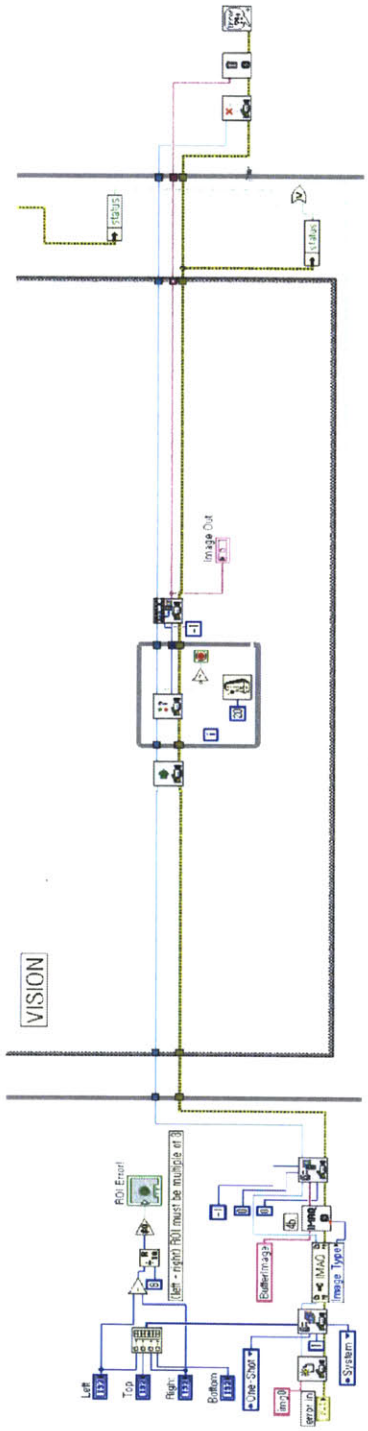

Figure A-7: Labview code for the vision panel.

A.2 FPGA edge counter for the A-quad-B encoder

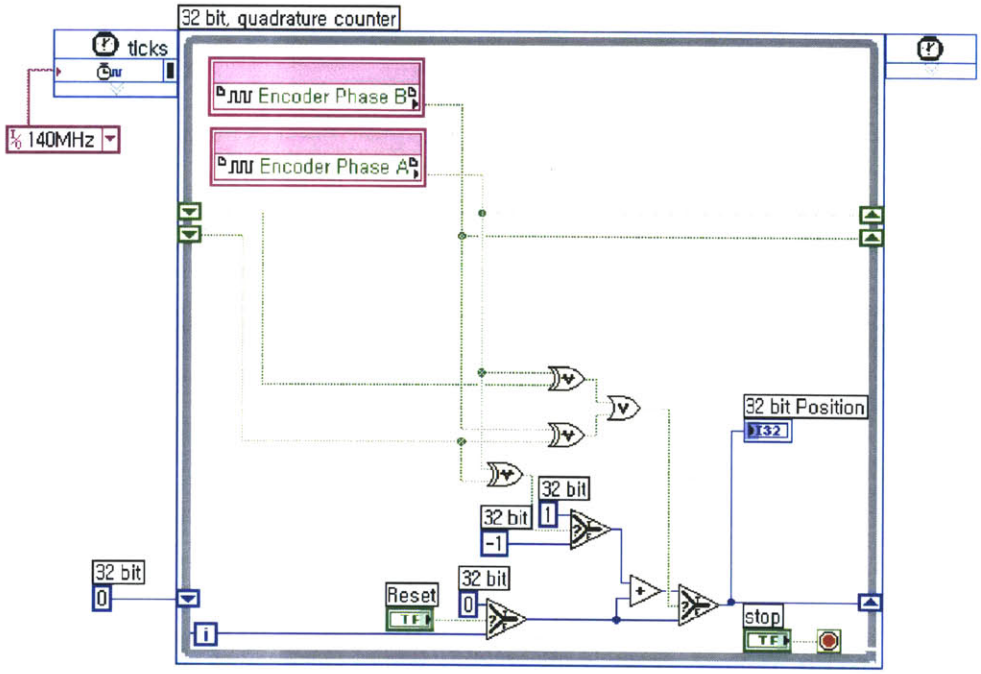

Figure A-8: Labview code for the encoder edge counter in FPGA.

A.3 Real-time control loop

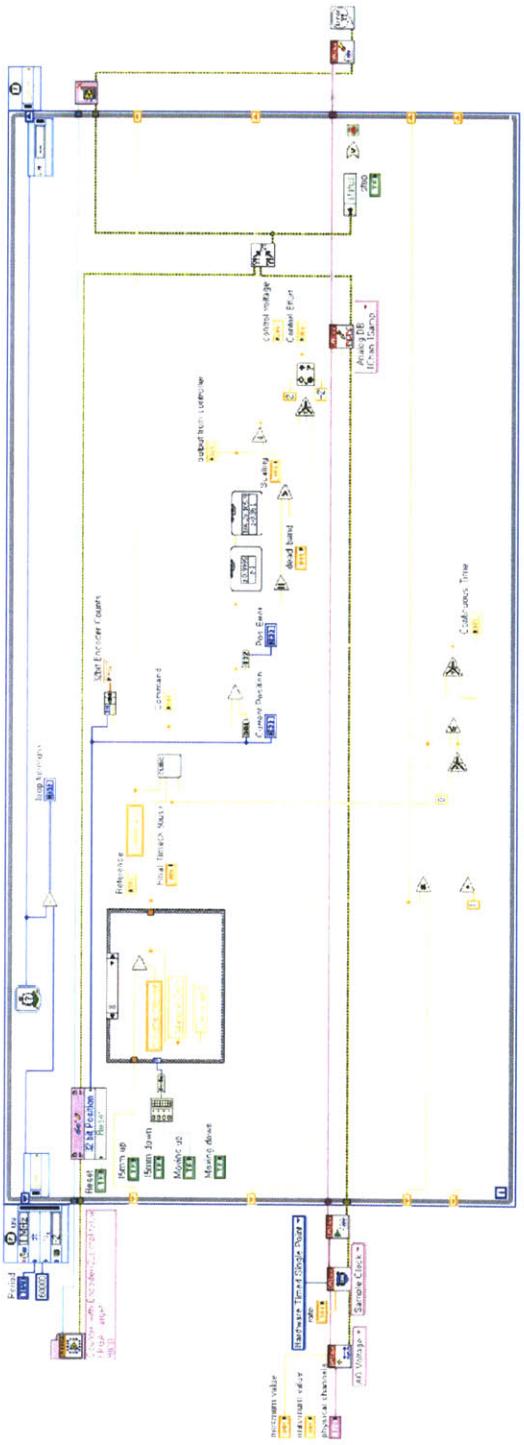

Figure A-9: Labview code for the real-time controller.

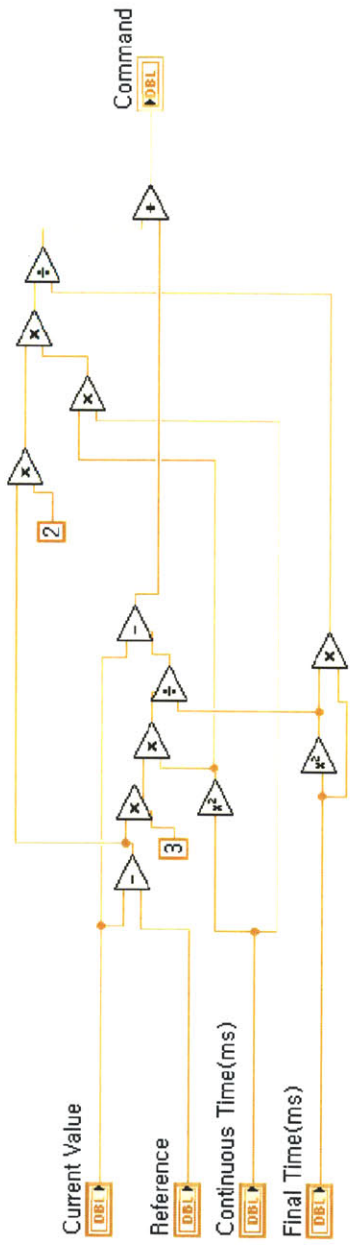

Figure A-10: Detailed code for the Cubic subvi.

Appendix B

Vendors

National Instruments Corporation

11500 N Mopac Expressway

Austin, TX 78759-3504

Telephone – (512) 683–0100

Web address – http://www.ni.com

Product used –

Hardware: PXI Chassis 1042, PXI Embedded Controller 8176, Multi-function DAQ 6052E, IMAQ Vision Card 1409, FPGA Card 7813R

Software: LabVIEW 2010

Aerotech Inc.

101 Zeta Drive

Pittsburgh, PA 15238-2897

Telephone – (412) 963–7470

Web address – http://www.aerotech.com

Product used in design – PRO Linear Stage 115-200, PRO Linear Stage 165-400

Specifications – http://www.aerotech.com/products/pdf/pro115.pdf, http://www.aerotech.com/products/pdf/pro165.pdf

Olympus America Inc.

3500 Corporate Parkway

Center Valley, PA 18034

Telephone – (617) 335–0073

Web address – http://http://www.olympusamerica.com/

Product used in design – Olympus Inverted Microscope CKX 41

Specifications – http://www.olympusamerica.com/seg_section/product.asp?
product=1038&p=144&sub=2&c=1

Marzhauser Wetzlar GmbH & Co.

In der Murch 15

D-35579 Wetzlar, Germany

Telephone – +49 (0) 6441–9116-0

Web address – http://www.marzhauser.com/nc/en.html

Product used in design – Marzhauser SCAN IM 127×83

Specifications – http://www.marzhauser.com/en/pim/produktdetail-popup.html?
view=details&pimid=a215&no_cache=1&m=null&p=null

Watec Incorporated

720 Route 17M, Suite 204 A

Middletown, NY 10940

Telephone – (845) 359–1490

Web address – http://www.wateccameras.com/index.php

Product used – Watec CCD Monochrome Camera 902C (obsolete, same as 902B)

Specifications – http://www.wateccameras.com/products.php?prod_id=178

Edmund Optics Inc.

101 East Gloucester Pike

Barrington, NJ 08007-1380

Telephone – (800) 363–1992

Web address – http://www.edmundoptics.com/

Product used – VZM 1000 Zoom Imaging Lens

Specifications – http://www.edmundoptics.com/onlinecatalog/displayproduct.cfm?productid=3280

Vita Needle Company, Inc.

919 Great Plain Avenue

Needham, MA 02492

Telephone – (781) 444–1780

Web address – http://www.vitaneedle.com/

Product used – Seamless 316 Stainless Steel Tubing with 1/16″OD, 0.01″ wall thickness, Annealed temper

Valco Instruments Co. Inc.

8300 Waterbury

Houston, TX 77055

Telephone – (713) 688–9345

Web address – http://www.vici.com/

Product used – PEEK Tubing with 1/16″OD, 0.040″ID TPK140-10

Labsmith, Inc.

6111 Southfront Road, Suite E

Livermore, CA 94551

Telephone – (925) 292–5161

Web address – http://www.labsmith.com/

Product used – PEEK Luer-lok Adapter for 1/16″OD tubing (T116–300), PEEK One-piece Fitting T116–100

Cirrus Logic, Inc.

2901 Via Fortuna

Austin, TX 78746

Telephone – (800) 625–4084

Web address – http://www.cirrus.com/en/

Product used – Power Operational Amplifier PA04

Specifications – http://www.cirrus.com/en/pubs/proDatasheet/PA04U_L.pdf

Tecan US, Inc.

4022 Stirrup Creek Drive Suite 310

Durham, NC 27703

Telephone – (800) 352–5128

Web address – http://www.tecan.com/

Product used – 60mm Stroke OEM Syringe Pump Cavro XLP 6000, Syringe XLP 50.0μL

Specifications – http://www.tecan.com/2.3101/Cavro-XLP-6000-Specifications

Dolan-Jenner Industries

159 Swanson Road

Boxborough, MA 01719

Telephone – (800) 833–4237

Web address – http://www.dolan-jenner.com/

Product used – Fiber-Lite Model 190

Specifications – http://www.dolan-jenner.com/Pro/190.htm

Appendix C

Drawing

C.1 Mounting hub for the encoder gratings

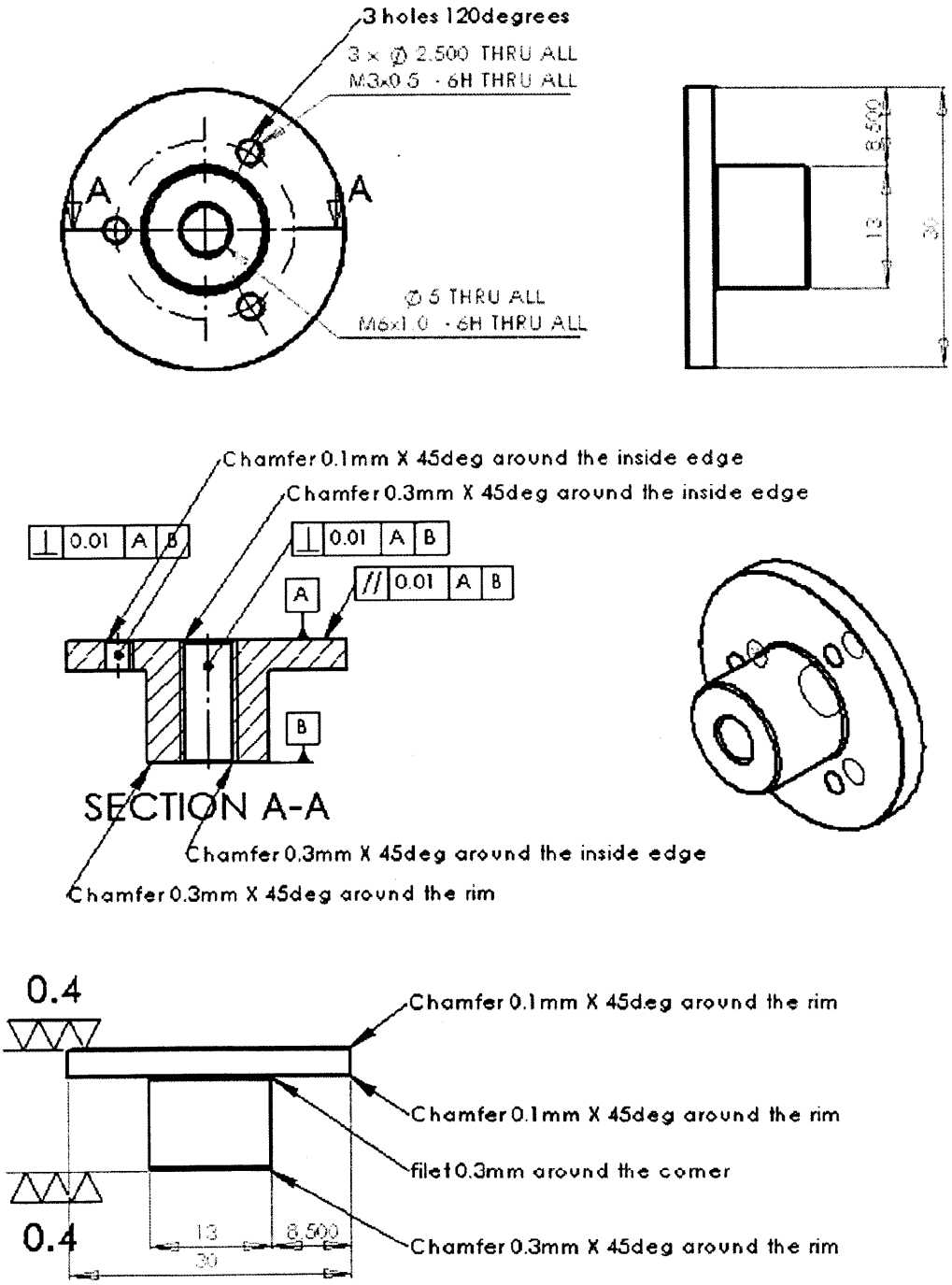

Figure C-1: Drawing for the mounting hub discussed in Chapter 4.

Bibliography

[1] Brekke, O.H. & Sandlie, I. *Therapeutic antibodies for human diseases at the dawn of the twenty-first century.* Nat. Rev. Drug Discov. 2, 52-62 (2003).

[2] Love JC, Ronan JL, Grotenbreg GM, van der Veen AG. *A microengraving method for rapid selection of single cells producing antigen-specific antibodies.* Nature Biotechnology, 2006. Volume 24 Number 6. Page703.

[3] Ostuni, E., Chen, C.S., Ingber, D.E. & Whitesides, G.M. *Selective deposition of proteins and cells in arrays of microwells.* Langmuir 17, 2828-2834 (2001).

[4] Bradshaw EM, Kent SC, Tripuraneni V, Orban T, Ploegh HL, Hafler DA, Love JC. *Concurrent detection of secreted products from human lymphocytes by microengraving: cytokines and antigen-reactive antibodies.* Clin Immunol. 129:10-.18 (2008).

[5] Ludwick, S., Trumper, D., *Design of a rotary fast tool servo for ophthalmic lens fabrication.*, Precision Engineering, 23/4:253-259 (1999).

[6] Ma, D. Trumper, D., *Design and implementation of a rotary fast tool servo for a turning machine.*, MS thesis, Massachusetts Institute of Technology, Department of Mechanical Engineering, 1998.

[7] J.R. Kovac, J. Voldman, *Intuitive, image-based cell sortinig using optofluidic cell sorting.*, Anal. Chem. 79, 9321-9330 (2007).

[8] James M. Gere, *Mechanics of Materials*, Nelson Thornes, 2002.

[9] P.J. Rae, D.M. Dattelbaum, *The properties of poly(tetrafluoroethylene) (PTFE) in compression.*, Polymer, 45, 7615-7625 (2004) <http://www.sciencedirect.com/science/article/B6TXW-4DB58X2-2/2/278e695bb-18f5714020d77974e2d9499>

[10] Dahl, P. R., *A solid friction model.*, Aerospace Corp., El Segundo, CA, tech. Rep. TOR-0158(3107-18)-1 (1968) <http://handle.dtic.mil/100.2/ADA041920>

[11] P.R. Dahl, *Solid friction damping of mechanical vibrations.*, AIAA Journal, 14, 1675-1682 (1976)

[12] Farid Al-Bensder, *Fundamental of friction modeling.*, American Society for Precision engineering, 48, 117-122 (2010)

[13] H. Olsson, K.J. Åström, C. Canudas de Wit, M. Gäfvert, P. Lischinsky, *Friction models and friction compensation.*, European Journal of Control, 4, 176-195 (1998)

[14] C. Canudas de Wit, H. Olsson, K.J. Åström, P. Lischinsky, *A new model for control of systems with friction.*, IEEE Transaction on Automatic Control, 40 (1995)

[15] D. Haessig, B. Friedland, *On the modeling and simulation of friction.*, Amer. Contr. Conf., San Diego, CA, 1256-1261 (1990)

[16] D. Chou, Trumper, D., *Dahl friction modeling.*, BS thesis, Massachusetts Institute of Technology, Department of Mechanical Engineering, 2004.

[17] J. Courtney-Pratt, E. Eisner, *The effect of a tangential force on the contact of metallic bodies.*, Proceeding of the Royal Society, A238, 529-550 (1957)

[18] Polytetrafluoroethylene (PTFE), May 9, 2011 <http://www.bearingworks.com/content_files/pdf/retainers/PTFE%20datashe-et.pdf>

[19] MatWeb Material Propery Data, May 9, 2011
<http://www.matweb.com/search/datasheet.aspx?matguid=ffc10b
084c4e4dd69754-38d9968e1292&ckck=1>

[20] AK Steel Corp., Product Data Bullentin 304/304L Stainless Steel, May 9, 2011
<http://www.aksteel.com/pdf/markets_products/stainless/austenitic/
304_304L_Data_Bulletin.pdf>

[21] Nanomotion Inc. 1 Comac Loop, Suite 14B2, Ronkonkoma, NY 11779.
Tel: 800-821-6266, URL: http://www.nanomotion.com/.